Acta
Technica
Jaurinensis

Vol. 12, No. 4, pp. 268-293, 2019
DOI: 10.14513/actatechjaur.v12.n4.498
Available online at acta.sze.hu

Literature Research on Experimental Investigations of Automotive Turbocharger Rotordynamics

P. Sass[1]

[1]Széchenyi István University, Department of Internal Combustion Engines
Egyetem tér 1, 9026, Győr, Hungary
e-mail: sass.peter@ga.sze.hu

Abstract: Contemporary turbochargers are high-speed rotating devices, commonly supported by full floating bearings or semi-floating bearings. Depending on the size and operational speed of the turbocharger, rotordynamics significantly changes. Industrial turbochargers are operating below 20.000 RPM and their rotor weight is substantial, leading to quasilinear rotordynamics behaviour. By contrast, automotive turbochargers are rotating up to 300.000 RPM with non-linear rotordynamics characteristics. Due to this non-linearity, rotor movement is intense, and bearing load is dynamically changing all the time. The consequence is reduced lifespan of the turbocharger. In this paper, the effect of changing bearing clearances, as well as the differences between semi-floating and full floating bearing constructions will be described based on journal papers scientific publications on the topic. Also, the damping and whirling phenomenon inside a bearing system will be investigated and presented in a comprehensive literature research on automotive turbocharger rotordynamics.

Keywords: turbocharger, full-floating bearing, semi-floating bearing, rotordynamics, vibration diagnostics

1. Introduction

A turbocharger contains a turbine and a compressor wheel interconnected with a common shaft, which is in most cases supported by full floating bearings or semi-floating bearings. The design of the bearing system and dimensions of the inner and

outer clearances have significant effect on subsynchronous rotor vibrations. The turbocharger rotor system has eigenfrequencies below the synchronous rotation frequencies. Therefore, subsynchronous excitation can cause induced subsynchronous rotor vibrations, and it is important to know the characteristics of these in the vibration spectrum [1].

The aim of the author of this review paper is to collect and summarise the most substantial observations from scientific literature written on the topic of turbocharger rotordynamics, and to make conclusions about the remaining potential in the research of turbocharger vibrations, particularly focusing on those phenomena related to operation of the bearing system. The varying load on the bearings can cause reduced lifespan of the turbocharger, and also has an influence on its running quality. Therefore, research of the vibrations inside the turbocharger central housing plays an important role in application of automotive turbochargers.

2. Rotordynamics of Small Turbochargers Supported on Floating Ring Bearings - Highlights in Bearing Analysis and Experimental Validation

This article written by Luis San Andres, Juan Carlos Rivadeneira, Kostandin Gjika, Christopher Groves and Gerry LaRue was published by the American Society of Mechanical Engineers in the Journal of Tribology 2007 [4]. It sums up basic knowledge on the linear and non-linear rotrodynamics phenomena of automotive turbochargers. The authors are focusing on subsynchronous vibrations measured on a turbocharger cold gas test bench, and compare the measurements with numerical predictions. Luis San Andres and Juan Carlos Rivadeneira state, that subsynchronous vibrations are occurring due to the circumferential whirling of the oil inside the bearing clearance. Moreover, if the outer bearing clearance is increased compared to the inner oil film thickness, subsynchronous vibrations can be suppressed. However, in practice, this is only true at low operating speeds [2, 3, 4].

2.1. Motivation

As claimed by the authors, the size of the inner and outer bearing clearances are one of the most important turbocharger design parameters from rotordynamics point of view. The turbocharger can operate in three different critical states or modes. In the first critical rotational speed regime or mode, the conical rotor deflection pattern dominates with relatively large rotor shaft movement both at the compressor and turbine side. In the second mode of operation, the rotor behaviour shows cylindrical deflections,while in the third critical rotor speed regime or mode, the turbocharger shaft reaches flexible deformation states. In the first two vibration modes, the rotor has rather low eigenfrequencies. When the rotor system is properly balanced, the

amplitudes of the subsynchronous vibrations can be as high as three times larger than the synchronous ones. It is possible, that frequencies of subsynchronous vibrations overlap the low eigenfrequencies of the rotor system during rigid rotor modes because of the low eigenfrequencies of the system in this frequency range. The presented study and related references contain experimental and computational investigations on the effect of bearing clearance change on rotor vibrations [4, 5].

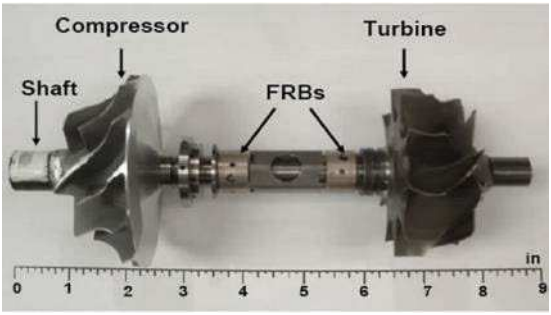

Figure 1. Measured turbocharger rotor of [4]

2.2. Experimental turbocharger and shaft motion measurements

The vibrations of the rotor were measured both on the compressor and on the turbine side. The most interesting part of the investigation was when rotor speed reached $65{,}000\ RPM$, and the floating bearing probably stopped spinning, which led to significant increase in the vibration amplitudes at about 0.5 times of the synchronous frequency [4, 6].

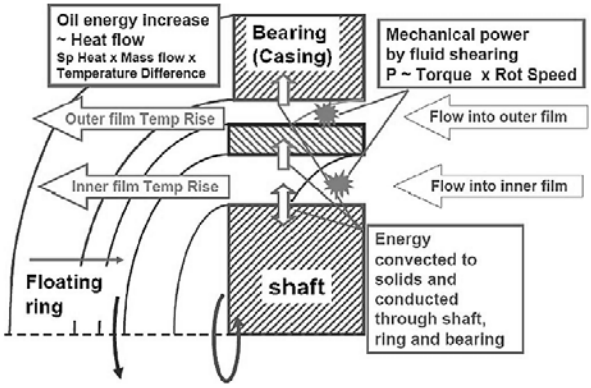

Figure 2. Heat flow inside the bearing housing [4]

In real operating conditions and also on hot gas test benches, the shaft is a heat source for the bearing system, so the inner oil film heats up and the amplitudes of vibration could change due to the smaller damping coefficient because of this temperature increase. The measurements took part with oil pressures between 1,5 and 2,7 bar and oil temperatures between 32-46 °C, with rotor speeds up to 80,000 RPM. The shaft movement was also measured with inductive proximity sensors installed perpendicularly to each other. The turbocharger speed was measured on the compressor side with an infrared wheel-speed sensor. In addition, two optical fibre cables were built into the turbocharger center-housing facing exactly to the bearings to follow rotational of the bearings by detecting the oil threads passing by. With this measuring system, a relation could be found between the amplitude growths of the subsynchronous vibrations and rotational speed of the full floating bearing [4].

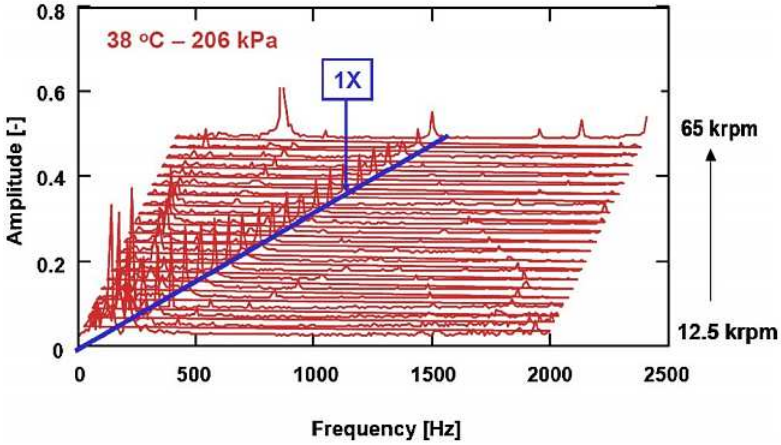

Figure 3. Waterfall diagram of the turbocharger of [4]

Below $20{,}000\ RPM$ the band structure of the spectrum is very complex, and the vibration amplitudes are also high due to self-induced vibrations. The frequencies are close to the natural frequencies of the rotor at low operational speed.

At $65{,}000\ RPM$, a significant amplitude peak has become visible. It is a plausible assumption that this critical frequency could exactly be the rotational speed where the floating ring bearing stops spinning [4, 7]. At high rotational speed, the thickness of the inner oil film increases, while the outer film thickness decreases due to heat exchange effects. This assumed to be the reason why the movement of the floating bearing could get obstructed [4, 8]. However, tests show that rotational speed of the floating bearing does not match well with the theoretically estimated values

3. Effects of bearing outer clearance on the dynamic behaviour of the full floating ring bearing supported turbocharger rotor

The paper was published by Elsevier, in the journal of Mechanical Systems and Signal processing in 2012 [10], written by L. Tian, W.J. Wang and Z.J. Peng in the University of Sussex, United Kingdom.

3.1. Motivation

The document is dealing with the nonlinear rotordynamic phenomena by using run-up and run-down simulation methods. The authors investigate the effect of bearing outer clearance change on rotordynamic characteristics. With the numerical method applied, the natural frequencies of the rotor can be predicted and also the nonlinear jumps in the vibrations can be explained [9, 10].

3.2. The Turbocharger Campbell diagram

The Campbell diagram or also called as interference diagram shows the natural frequencies of a rotor system as a function of rotational speed.

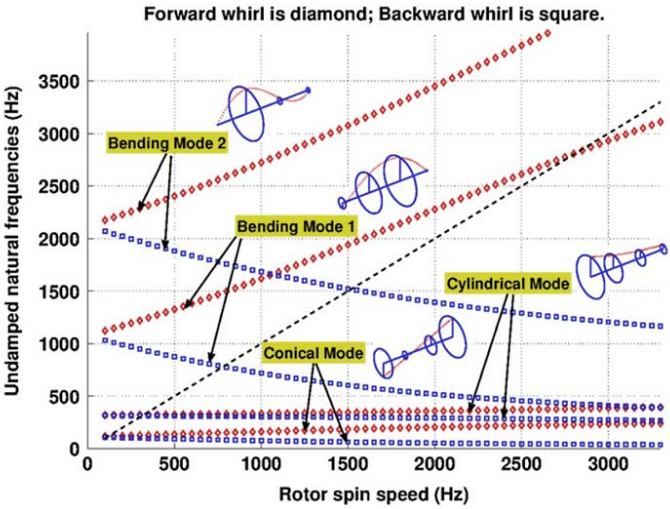

Figure 4. A turbocharger Campbell diagram (dash line is the synchronous line) [10]

Figure 4 shows the Campbell diagram of a turbocharger. When the rotational speed of the rotor is low, the subsynchronous (or even the synchronous) vibrations

can match the natural frequencies of the system, which leads to self-induced vibrations. These self-induced vibrations could be critical and important to verify during the design phase of the turbocharger because of their large amplitudes and high acoustic emission levels [10, 11, 12].

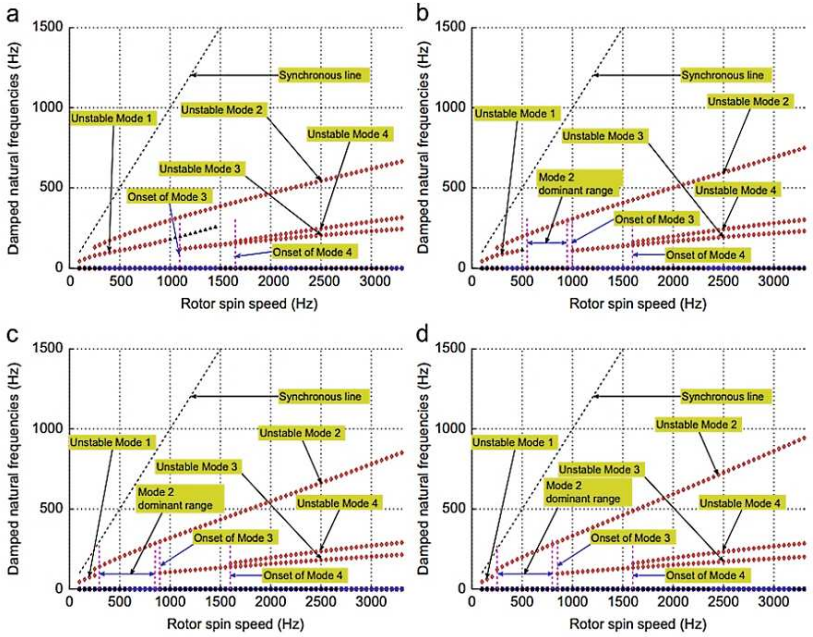

Figure 5. Campbell diagrams with varying bearing outer clearances (a=30 μm; b=35 μm; c=40 μm; d= 44 μm) [10]

Figure 5 shows, the effect of changing the bearing outer clearance. By increasing the outer clearance, the duration of the first unstable mode (Mode 1) can be significantly reduced, depending also on rotational speed. With 30 μm outer clearance, the first unstable mode is visible till 60,000 RPM rotor speed. However, when the clearance is increased up to 44 μm, this first unstable mode lasts till 12,000 RPM only [13, 14].

3.3. Result of the run-up simulations

The author performed run-up simulations and evaluated the data in waterfall diagrams. The aim of the simulations was the investigation of non-linear subsynchronous vibrations [10].

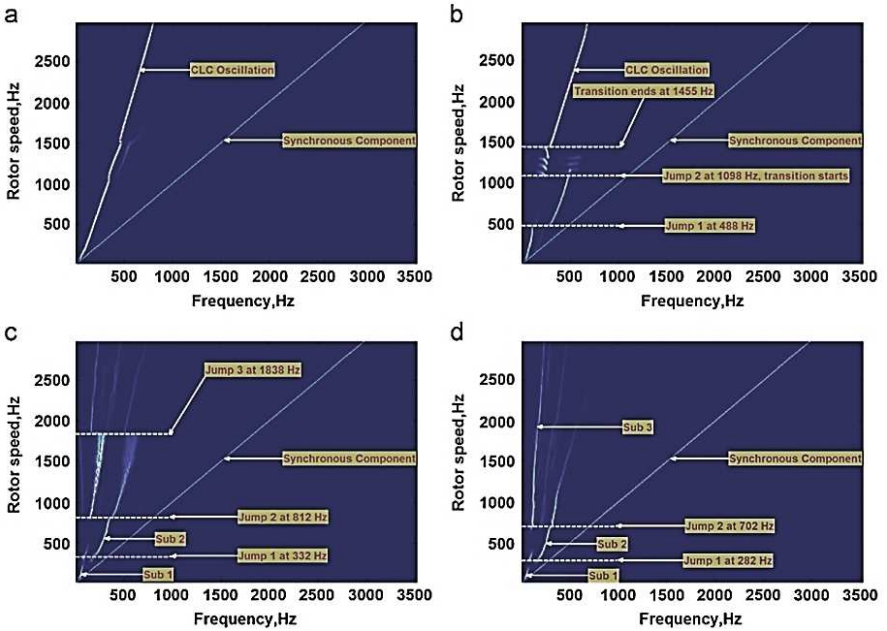

Figure 6. Waterfall diagrams from run-up simulations with 5 μm unbalance offset and varying outer bearing clearences from 30 μm to 44 μm (in the order of a to d) [10]

The simulation results show that the considered bearing outer clearance content can be subdivided into four ranges. The first range is from 30-33 μm. In this clearance range nonlinear jump cannot be observed. In range 2, from 34-39 μm outer cleareance, nonlinear jumps are identified in a sequence of Sub 1 to Sub 2. In case of run-up simulations with bigger outer clearance, nonlinear jumps are likely to happen at lower rotational speeds. In range 3, where the clearance is 40-43 μm, the jump sequence is Sub 1 to Sub 2, then Sub 2 to Sub 1, and then Sub 1 to Sub 3. The jump speed also shifted to lower rotational speeds than in the previous range. Range 4 is with clearance from 44 to 50 μm. Non-linear jumps are also visible, following the sequence of Sub 1 to Sub 2, and then Sub 2 to Sub 3. Bigger bearing clearance leads to an earlier upset of Sub 2 vibration [9, 10, 15].

4. Experimental and numerical investigations on an automotive turbocharger with a transparent bearing section

This following paper is written by W. Köhl from Technical University of Darmstadt, M. Kreschel and D. Filsinger from IHI Charging Systems International GmbH, Germany in 2014 [16].

4.1. Motivation

In this publication the authors present a research on the dynamic behaviour of a full-floating radial bearing supported turbocharger via numerical investigations and measurements on a cold gas turbocharger test bench. The aim of this work is to examine changes in the orbit and deflections of the turbocharger rotor as bearing housing is being modified. The bearing housing itself was made of a special transparent material, and a high-resolution camera recorded the rotation movement of the bearing during test operation [16, 17].

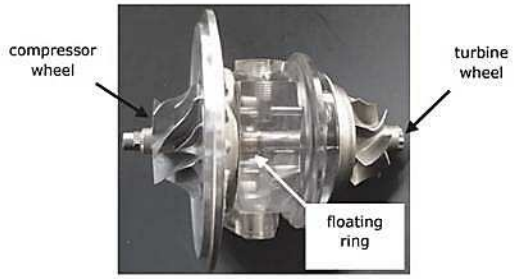

Figure 7. Turbocharger with a transparent bearing section [16]

4.2. Highlights of the experimental setup

The oil induced vibrations are most likely to be manufested as a “constant tone” noise from the charger. During the operation of the rotor, the frequency of subsynchronous vibrations is only changing to a small extent. The bearing system transmit these vibrations, and in the worst case and depending on the resonance frequencies, the turbine wheel, the compressor wheel or even the exhaust system could behave as a sound amplifier [18].

The measurements presented took part on a turbocharger cold gas test-bench, with 27°C oil temperature. The turbocharger speed was measured at the compressor wheel side, and the received signal was recorded through a low-pass filter. The configuration of the test can be seen in details in Table 1 below [16].

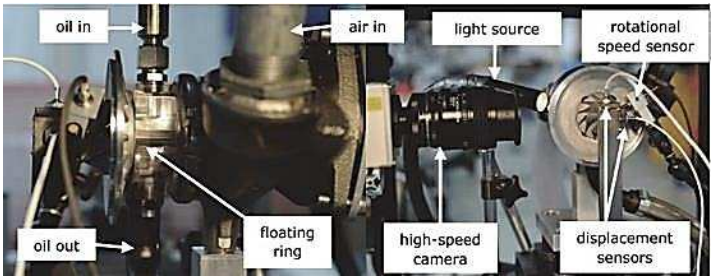

Figure 8. Setup of the measuring system of [16]

The essence of the investigation was to validate the numerical calculations with test-bench measurements, that is, to confirm that the calculated natural frequencies of the system are consistent with the measured ones. During the tests, the turbocharger performed a run-down operation from a specified rotational speed [16], instead of a run-up phase of some other investigations.

Table 1. Measurement setup details [16]

Component	***Type***	***Configuration***
Turbocharger	IHI Charging Systems International GmbH	Waste gate closed No compressor housing
High-Speed camera	Photron: Fastcam Ultima 512	32,000 fps 512x12 pixels
Light source	Shot: cold light 2500 LCD	
Displacement sensor	μ-Epsilon, Eddy current DT 110-T-S1-M-C3	
DSpace		Sampling frequency: 8192 Hz
Oil	ESSOLUBE X2 20W	ηoil (27°)≈110 mPas

4.3. Numerical and experimental results

As described by the authors, the system reaches its first natural frequency when the amplitudes of the subsynchronous vibrations originating from the inner bearing clearance reach their maximum and then begin to decrease. In addition, the rotational

speed of the bearing also has an effect on the vibrations from the inner bearing clearance [16].

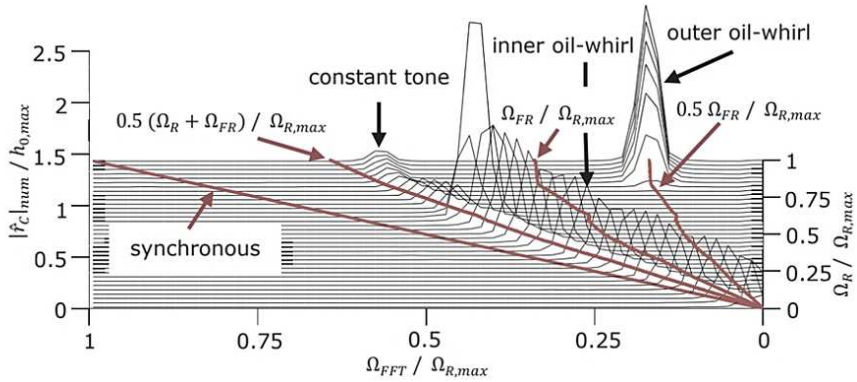

Figure 9. Calculated waterfall diagram from the numerical model [16]

On the calculated waterfall diagram of Figure 9., a significant amplitude peak appears from 0.8 Ω_(R,max) with approximately half the frequency of the floating ring's rotational speed. This vibration belongs to the oil-whirl of the outer film, and does confirmed by the experiment. In general, the calculated rotational speed of the floating ring is higher than the experimentally detected floating ring speed [16, 19].

The authors wanted to adjust the computed results closer to the experimentally measured values, so the stiffness and the damping of the inner and outer oil film was modified in the model accordingly.

As predicted by the Campbell diagrams fom calculations, the effect of subsynchronous vibrations can be reduced if the floating ring rotational speed is reduced. The floating ring rotational speed can be decreased by changing the bearing geometry. If the inner bearing clearance increases, the stiffness of the inner oil film reduces. Thus, the constant tone phenomenon will likely occur at lower rotor speeds, causing smaller vibration amplitudes. To reduce the outer whirl, the damping of the outer oil film has to be increased [16, 20].

The rotational speed of the floating bearing was recorded, and the results show that the ring speed ratio (Ω_fring/Ω_Rotor) is in the relative speed range of 0.1 … 0.2. The friction torque, which drives the floating ring turned out to be smaller in reality than the numerically predicted values. This is caused by the different temperatures of the inner and outer oil film, which changes the viscosity of the oil. The transparent bearing housing and a high-speed camera allows to measure the rotational speed of the floating ring. With this help, the numerical models can be

validated. The numerically calculated ring speed ratios are overestimated compared to the experiment. This could be improved by re-running the tests with oils of different viscosity levels [16, 19, 20].

5. Effects of Semi-floating Ring Bearing Outer Clearance on the Subsynchronous Oscillation of Turbocharger Rotor

The research presented in this section was published in the Chinese Journal of Mechanical Engineering written by Liang Feng, Zhou Ming, and Xu Quanyong, in the School of Aerospace Engineering, Tsinghua University, Beijing in 2016 [21].

5.1. Motivation

The paper presents research results on the topic of vibration diagnostics of turbochargers supported with semi-floating bearings. The outer clearance of the semi-floating bearing affects the magnitude and the frequency of the whirl motion phenomenon, which is important from turbocharger designs with semi-floating bearings perspective. To explore the effects of the outer clearance, the authors used a transient finite element analysis program for the rotor. The oil film bearing of the test was built and validated by another published experimental study.

The authors present that as the outer clearance increases, three subsequent steps are going to occur to the low-frequency subsynchronous vibrations. First, the vibration amplitudes are rather high, then a gradual amplitude recession happens. and finally, the two subsynchronous vibrations combine. The high-frequency subsynchronous oscillations start to evolve gradually first, then their amplitudes increase, and finally the vibration modes combine. The increasing outer clearance causes a „zipper" effect to these oscillations, which means that the subsynchrons vibrations start to combine at lower speeds if the outer clearance increases [21, 22, 23].

5.2. Numerical Method

The equivalent simplified rotor model was divided into 25 one-dimensional elements with 26 nodes. The blue section on the figure represents the aluminium alloy compressor impeller [21].

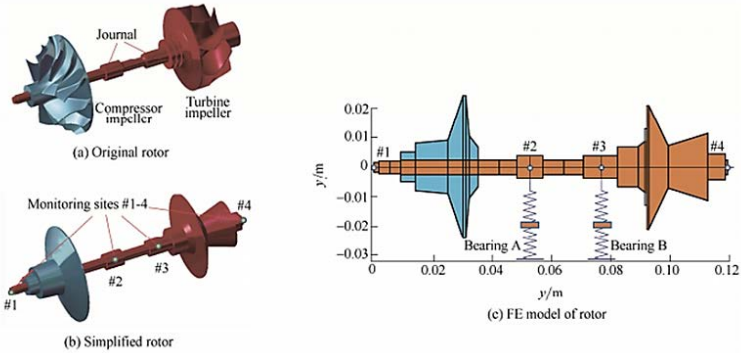

Figure 10. Simplified model of the rotor of [21]

The basic rotordynamic equation, which helps to specify the correct model, is the following:

$$\mathrm{M_{rotor}}\ddot{\mathrm{q}}_{\mathrm{rotor}} + (\mathrm{C_{rotor}} + \Omega \mathrm{G_{rotor}})\dot{\mathrm{q}}_{\mathrm{rotor}} + \mathrm{K_{rotor}}\mathrm{q_{rotor}} = \mathrm{F_{rotor}}, \quad (1)$$

In many turbochargers, the rotor is supported by one semi-floating ring, which incorporates two load surfaces (compressor side and turbine side). The ring can be considered as a rigid body since it is stubbier than the shaft itself [24].

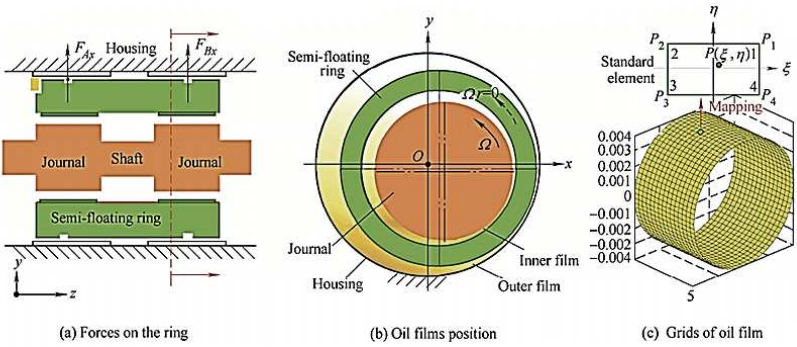

Figure 11. Bearing model of [21]

For a comprehensive model, the oil film model also had to be deduced. The pressure distribution in a fluid film bearing can be described by the Reynolds equation. By solving the equations, the pressure at each node can be calculated and integrated into the nonlinear oil film force components that are then applied to the rotor-ring equation in each step of the numerical integration [21, 25].

5.3. Non-linear analysis of ideal conditions

Under ideal conditions, the gravity is neglected in the simulation, and the rotor is supposed to be perfectly balanced. The equilibrium position of the ring is the center of the housing, which position is unstable. The vibrations originating from the whirling motion of the oil will be visible in less than half of the rotor rotational speed. Figure 12 shows the decomposed limit cycles of the shaft orbit at different rotational speeds for the subsynchronous vibrations. The vibration amplitude at the compressor side is larger than the turbine side for Sub A, but for sub B the amplitudes for both sides are close. This may be caused by the different mass densities of the compressor wheel and the turbine wheel [21, 26].

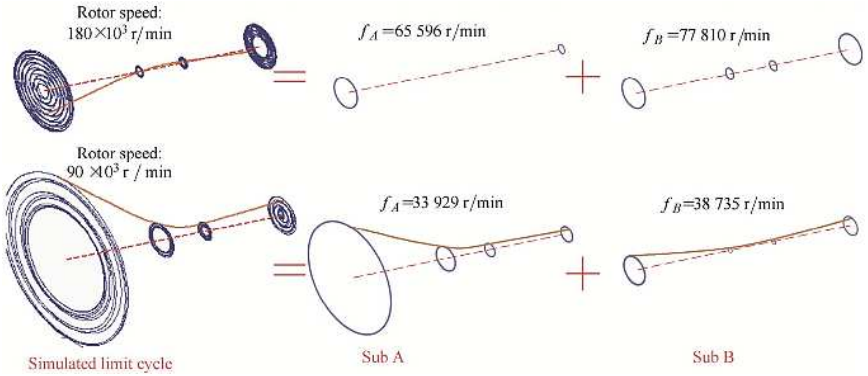

Figure 12. Rotor orbit at different rotational speed [21]

Figure 13 clearly shows that as the outer clearance increases, the changes in subsynchronous amplitudes are significant. When $c_2 = 24\ \mu m$, Sub 1 has a quite large amplitude while Sub 2 is hardly visible, and the limit cycles are perfect cycles. As c_2 increases, Sub 1 becomes weaker while Sub 2 extends downwards to 160,000 RPM. When c_2 continues to increase, Sub 1 weakens further and Sub 2 vibration occurs at lower and lower rotational speeds. At $c_2 = 40\ \mu m$, the magnitude of the subsynchronous vibrations are very similar to each other, and Sub 2 appears in almost the whole rotational speed range. When $c_2 = 46\ \mu m$, Sub 1 and Sub 2 merges to a new subsynchronous oscillation named Sub 0. The combination starts from high rotor speeds and extends to lower rotor speeds like a „zipper". When c_2 becomes $60\ \mu m$, the „zipper" pulls down to the low end of the rotor speed range, and Sub 0 starts at very low rotor speed, causing perfect cycles again [21, 27].

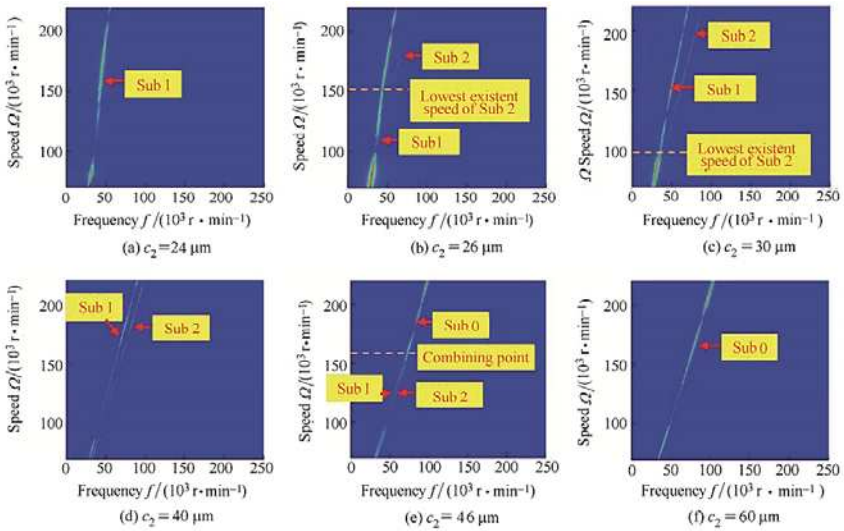

Figure 13. Frequency contours in ideal condition [21]

Figure 14 shows the frequencies of Sub 0, 1 and 2 at 160,000 RPM with different outer clearances (c_2). As the outer clearance increases, the subsynhcronous oscillations slowly move to 0.5 times the rotor speed frequency. The frequency of the Sub 1 vibration changes the most with the bearing clearance. Between 25 to 46 μm outer clearance values, the frequency of Sub 1 increases from 0.285 to 0.456 times the rotor rotational speed. After the merge, the frequency of Sub 0 only slightly increases with the change in outer clearance [21, 26].

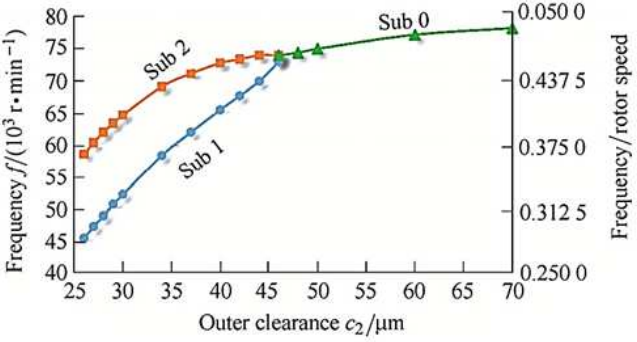

Figure 14. Frequencies of Sub 0, 1 and 2 at 160 000 r/min with different c_2 [21]

5.4. Non-linear analysis of real conditions

Under real conditions, the gravity and the unbalance always exist and have substantial influence to the behaviour of the rotor system. During this stage of the analysis, the gravity and unbalance effects were applied to the simulations [21].

The outer clearance c_2 was varied from 26 to 50 μm, and the rotor speed ranged from 70,000 RPM to 220,000 RPM in the simulation. Also, 0.04 g·mm unbalance was applied to the rotor (at both the compressor and the turbine side). In general, the subsynchronous oscillations go through a very similar development as the outer clearance increases like in the previous ideal simulation case. However, there are also some important differences between the ideal and real conditions. The evolution of Sub 2 is delayed. When c_2=26 μm, Sub 2 only exists above 200,000 RPM under real conditions, while it was excited at about 160,000 RPM under ideal conditions. Also, Sub 2 changes with a greater extent compared to the ideal case, and the merging process happens at smaller outer clearance values. On the other hand, Sub 2 does not appear below 140,000 RPM under either conditions [21, 28].

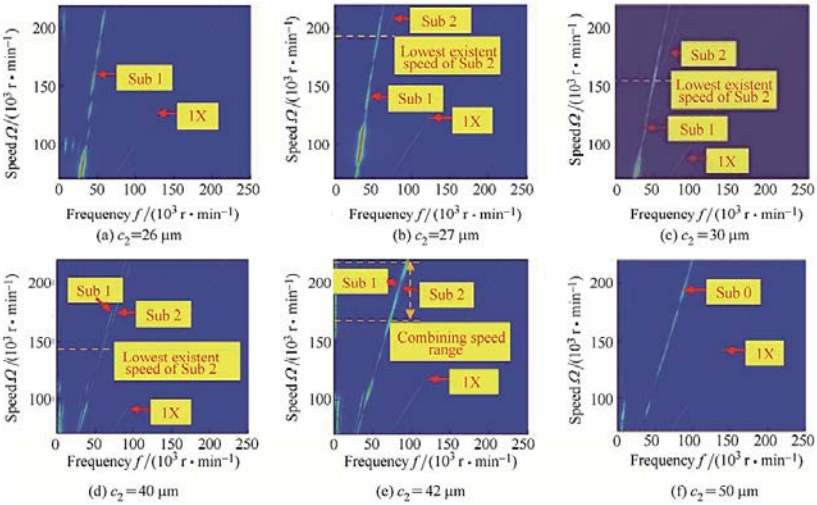

Figure 15. frequency contours in real condition [21]

The explanation for these phenomena is that the rotor has two bearings and Sub 1 and Sub 2 occurs between two different bearing surfaces. Sub 1 occurs in bearing A and Sub 2 is in bearing B. In this case, the gravity centre of the rotor is very close to bearing B, so the unbalance and the applied gravity has a greater influence on the Sub 2 oscillation [21].

6. Implementation of pre-measurements on a compressed-air operating turbocharger component test-bench

The comprehensive literature research provides an eligible amount of data to plan the turbocharger investigations, which leads to experimental tests of the simulation results. To successfully transplant the acquired information on the turbocharger rotrodynamics to measurements, the test-bench and the measuring system must be precise enough to detect the minor changes in the tribological system without disturbance. In such a way, pre-measurements are necessary before the experimental investigation of the bearing system, to ensure that the subsynchronous vibrations are measurable and the occurring noises on the test-bench are below the interference limit. In this purpose, vibration measurements were implemented on a compressed-air test-bench to map the occurring noises and identify the turbocharger vibration components on a Campbell diagram.

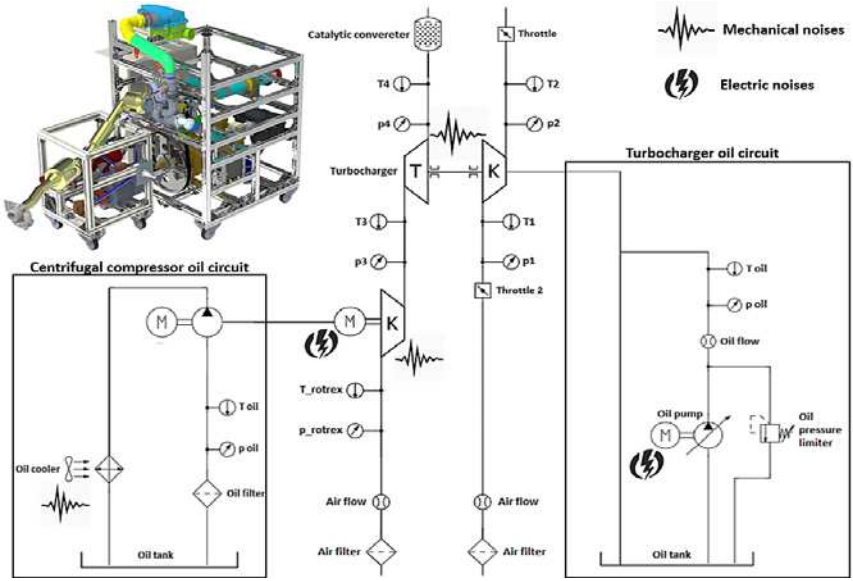

Figure 16. Structure and noises of the compressed-air test-bench

For the vibration analysis, an acceleration sensor has been mounted on the center-housing of the turbocharger. The used sensor can measure even $\mu m/s^2$ accelerations, therefore, significantly low body-noises can cause unwanted signals. To ensure that the test results are appropriate and the interference factors are well-known, the occurring noises of the test-bench (Figure 16.) itself had to be measured. An electric motor drives a centrifugal compressor with a high drive ratio. The

rotating compressor produces the desired amount of air pressure to spin up the turbocharger rotor. The test-bench has a built-in oil circuit for the turbocharger with fully controllable oil inlet pressure. In addition to the observation of the equipment, the noises in the test room have been recorded, while the sensor was mounted on the turbocharger because the important information in terms of the vibration analysis is to determine the undesirable noises for the evaluation. The most dominant noises during operation are originating from the centrifugal compressor and the equipment's high voltage electric systems. The electric noises are emitted by the operation of the oil pump in the turbocharger oil circuit and from the electric motor which drives the centrifugal compressor.

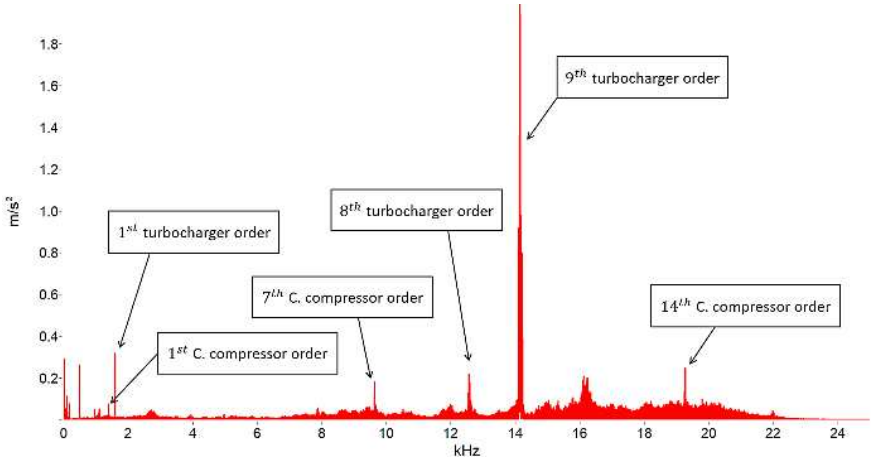

Figure 17. Fourier Spectrum of the measured turbocharger at stationary speed

Figure 17 shows the Fast Fourier Spectrum of the turbocharger. The rotational speed of the centrifugal compressor was set up to 84.000 RPM, which corresponded to 100.000 RPM rotational speed on the turbocharger. The most dominant vibration components are marked on the diagram. As the figure shows, the highest amplitude vibration is around 14 kHz frequency, which is the 9th order of the turbocharger vibration (the vibration components of the turbocharger will be analyzed later in this chapter). The magnitude of the 9th turbocharger order is close to 2 m/s^2, which is significantly higher than 7th order of the centrifugal compressor's vibration. On the other hand, both the 7th and the 14th order of the centrifugal compressor are clearly visible on the spectrum of the turbocharger. This means, that the interference from the centrifugal compressor must be considered.

Figure 18 shows the Campbell diagram of the investigated turbocharger. The simplest vibration component to find on this spectrum is the first order (1), which

equals the frequency of the rotor speed, e.g., if the rotational speed of the turbocharger is $60.000\,RPM$ $(1000\,1/s)$, then the first order or synchronous vibration occurs at $1000\,Hz$. The cause of this vibration is mainly the unbalance of the rotor assembly of the turbocharger (compressor wheel, shaft, turbine wheel, compressor wheel nut). The implementation of a perfect balancing method is impossible, so the synchronous vibration component is always visible on the Campbell diagram under real circumstances

The oil whirling noise is marked with (2) on Figure 18, which lies below the frequency of the synchronous vibration This vibration is also called constant tone, due to its slight change in frequency on a run-up phase. In this spectrum, a jump can be seen in the frequency of the constant tone vibration at $104{,}000\,RPM$. The cause of this frequency jump is related to rotordynamic phenomena. It is presumed, that the vibration mode of the rotor system is changing from conical to cylindrical mode. The frequency of the oil whirl is highly dependent on the damping of the bearing system, which is affected by oil temperature, viscosity and the inner and outer radial bearing clearances.

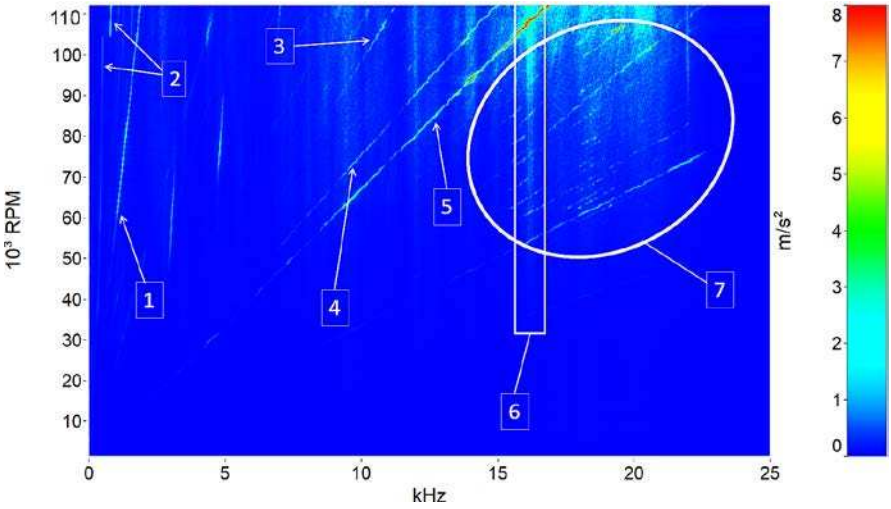

Figure 18. Turbocharger Campbell diagram

The vibration marked with 3 on Figure 18 shows the necessity of the measurements. The 7th order vibration of the centrifugal compressor is clearly visible and could be disturbing in the evaluation of the measured data.

The component marked with 4 and 5 are the vane pass frequencies of the turbocharger compressor (8 vanes) and turbine (9 vanes) wheel. As mentioned in the

previous chapter, the vane pass frequency can be obtained by multiplying the first order frequency with the number of vanes of the impeller. Vibration 4 and 5 are exactly 8 times and 9 times the synchronous vibration. The amplitudes of these vibrations are clearly affected by the rotational speed. Figure 18 shows that the 9th order of the turbocharger has significantly higher amplitude at high rotor speeds (over $90.000\ RPM$), than the 8th order. This is believed to be a consequence of differing turbine and compressor wheel weight and geometry and the fact that the turbocharger is powered on the turbine side, but further measurements are needed to clarify the cause of this phenomenon. Impeller damage could increase the amplitude of the 1st, 8th and 9th, depending on the type of damage suffered.

Electric noises can be seen in the region marked with 6 on Figure 18. The electric noises can be easily recognized by the blurry appearance on the spectrum and the invariable frequency. As discussed in the previous chapter, the electric noises of the test-bench are located at $4\ kHz, 8\ kHz, 12\ kHz, 16\ kHz$ and $20\ kHz$. In this case, the most dominant components are the high-frequency electric noises, especially at $16\ kHz$. It is important to distinguish these noises from the vibrations of the turbocharger because these components influence the measured acceleration level and can be misleading without spectral analysis.

In the region marked with 7, a group of high-frequency superharmonic components are visible. The frequency of these vibrations is the double of the vane pass components. The 14th order of the centrifugal compressor vibration as well as the 16th, 18th turbocharger compressor and turbine vane pass orders are in this area of the Campbell diagram.

7. Further potential in the topic of turbocharger vibration measurements as suggested by literature research

Based on the studies presented and the test-bench measurements, there are several remaining questions in turbocharger design in terms of turbocharger vibro-acoustics, especially if viewed from experimental investigations side. It can be supposed that there always remains a difference between the simulations and the data measured on a test bench. The measurements should be developed from cold gas test benches to hot gas test benches, or even to engine test benches to ensure that test conditions are as close to the real operational environment as possible.

There are also plenty of major question in the topic of turbocharger rotordynamics, which should be investigated and measured to provide useful data for the further developments. The damping coefficient of the bearing system is depending on numerous factors, such as the geometrical parameters of the bearings and the shaft, the used material, the quality of the oil and temperature. To be able to measure the

exact damping effect of the bearing system, a special tribometer is under development, which simulates the extremely high rotational speed of the rotor and measures the friction coefficient and the damping of the tribological system. For the investigations of the changing bending modes of the rotor under real conditions, high precision distance sensors are necessary. To be able to measure the motion of the shaft, the data processing and the sampling frequency of the measuring system needs to be very high. The shaft motion measuring system combined with vibration measurement can provide helpful information about the bending modes and the rotor response. With the mentioned equipment the magnitude of the constant tone vibration and the frequency jump of these oil whirl phenomena can be investigated.

7.1. Measuring the effect of changing physical state of the oil on the vibrations caused by its whirl

There is a huge potential in the vibration measurements with various oil quality and condition. Both temperature and viscosity level of the oil, as well as oil flow rate has an effect on the operation of the turbocharger rotor. Measuring the vibrations of the turbocharger with different oil temperatures can provide valuable information due to the change in damping coefficient of the oil, which depends on oil viscosity. With this measurement, vibrations at cold start and at hot operating conditions can be compared.

By the help of additional experimental investigations, results of simulations could further be validated and refined, thus reducing the costs of development phase of turbochargers. For better simulation results, the damping coefficient of oil could be calculated from test-bench measurements. By exciting the turbine shaft while accurately measuring acceleration levels, the damping coefficient can potentially be calculated, thus making the simulations more accurate. Under real operating conditions, damping coefficient of oil is also changing continuously as the oil is being heated up to operational temperature [29].

7.2. Comparison of different bearing constructions

Many of the publications studied dealt with the effect of bearing clearance dimensions change on characteristics of induced oscillations. A comprehensive experimental study could highlight the waterfall diagram differences between a semi-floating bearing and a full-floating bearing designs. With the use of cold gas and hot gas turbocharger test-benches in parallel, excited accelerations and characteristics of the subsynchronous vibrations could be validated in almost real operating conditions.

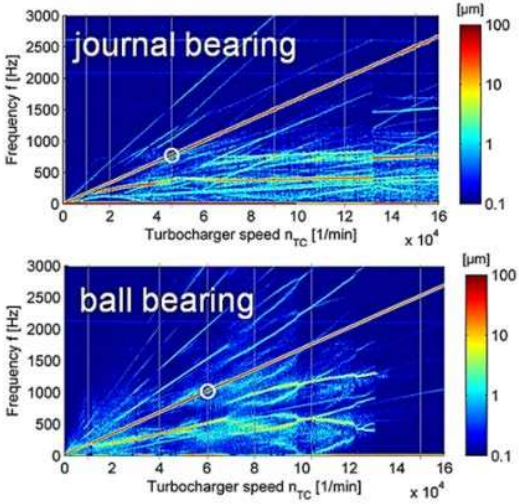

Figure 19. Campbell diagrams of turbochargers with different bearing constructions [30]

Ball bearings for automotive exhaust gas turbochargers are getting to become more common nowadays. Preliminary studies predict that better throttle response may be achieved by ball bearings due to the smaller friction forces at lower turbocharger rotational speeds. However, at high operating speeds, floating bearings also have less friction. Moreover, ball bearings have more intense acoustic emission levels, which negatively affects their penetration rate in automotive applications. Comparing the full-floating bearing, the semi-floating bearing and the ball bearing supported turbochargers on test-benches while measuring the emitted sound levels with microphones as well as the vibrations on the turbocharger in different operational conditions is important for the future of turbochargers. There are already some manufacturers that have tried ball bearing turbocharger applications in their vehicles [31].

7.3. Research of vibrations caused by the deterioration of ideal bearing conditions

Quality of the loaded bearing surfaces has strong effect on vibrations of the bearings. By measuring the acceleration levels on turbochargers with different bearing wear conditions a relation may be found between tribological phenomena inside the bearing housing and the vibrations generated outside. This method could be helpful for lifetime tests, or even could be a basis of an online damage detection system, supposing that the measurements are accurate and precise enough. To

diagnose the surface condition, special confocal microscopes are currently used for recording the whole surface and even to evaluate roughness parameters or wear volume after every test run.

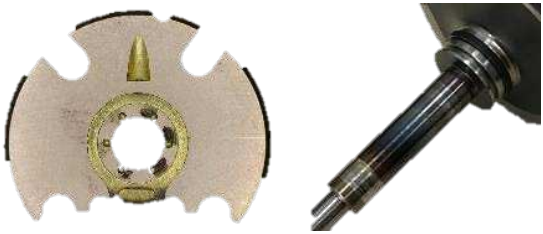

Figure 20. Wear on the loaded bearing surfaces of a turbocharger's thrust bearing and shaft

The aim of these measurements could primarily be the damage detection of the bearing system. By comparing turbocharger vibrations while the turbocharger is in assembled state with bearing conditions of different wear levels measured in disassembled state afterwards, functional dependences may be found to estimate bearing conditions online or real time. Early damage detection of the bearings thus may become possible, which would reduce time and cost of unnecessary disassembling of the chargers.

Acknowledgement

The paper was written with the support of the project titled "Internationalisation, initiatives to establish a new source of researchers and graduates and development of knowledge and technological transfer as instruments of intelligent specialisations at Széchenyi István University" (project number: EFOP-3.6.1-16-2016-00017).

References

[1] H. Nguyen-Schäfer, Rotordynamics of Automotive Turbochargers, 2nd Edition, Springer International Publishing AG, Ludwigsburg, Germany, 2015. doi: https://dx.doi.org/10.1007/978-3-319-17644-4

[2] H. R. Born, Analytical and Experimental Investigation of the Stability of the Rotor-Bearing System of a New Small Turbocharger, ASME Paper No. 87-GT-110, 1987. doi: https://doi.org/10.1115/87-GT-110

[3] M. Tanaka, A Theoretical Analysis of Stability Characteristics of High Speed Floating Bush Bearings, Proceedings of 6th International Conference on Vibrations in Rotating Machinery, IMechE Conference Transaction 1996–6, Oxford, UK, Paper No. C500/087/96, pp. 133–142, 1996.

[4] L. San Andres, J. C. Rivadeneira, K. Gjika, C. Groves, G. LaRue, Rotordynamics of Small Turbochargers Supported on Floating Ring Bearings - Highlights in Bearing Analysis and Experimental Validation, Journal of Tribology 129 (2) (2007) pp. 391-397.
doi: https://doi.org/10.1115/1.2464134

[5] C. Holt, L. San Andrés, Test Response of a Turbocharger Supported on Floating Ring Bearings Part I: Assessment of Subsynchronous Motions, Proceedings of 19th Biennial Conference on Mechanical Vibration and Noise, Chicago, IL, ASME Paper No. DETC 2003/VIB-48418, pp. 969-974, 2003.
doi: https://doi.org/10.1115/DETC2003/VIB-48418

[6] L. San Andrés, J. Kerth, Thermal Effects on the Performance of Floating Ring Bearings for Turbochargers, Proceedings of the Institution of Mechanical Engineers, Part J: Journal of Engineering Tribology 218 (5) (2004) pp. 1–14.
doi: https://doi.org/10.1243/1350650042128067

[7] M. Tanaka, Y. Hori, Stability Characteristics of Floating Bush Bearings, Journal of Lubrication Technolology 94 (3) (1972) pp. 248–259.
doi: https://doi.org/10.1115/1.3451700

[8] J. Kerth, Prediction and Measurement of the Rotordynamic Response of an Automotive Turbocharger with Floating Ring Bearings, MSc thesis, Texas A&M University, College Station, TX (2003).
URL http://hdl.handle.net/1969.1/ETD-TAMU-2003-THESIS-K426

[9] P. Bonello, Transient modal analysis of the non-linear dynamics of a turbocharger on floating ring bearings, Proceedings of the Institution of Mechanical Engineers, Part J: Journal of Engineering Tribology 223(1) (2009) pp. 79–93.
doi: https://doi.org/10.1243/13506501JET436

[10] L. Tian, W. J. Wang, Z. J. Peng, Effects of bearing outer clearance on the dynamic behaviours of the full floating ring bearing supported turbocharger

rotor, Mechanical Systems and Signal Processing 31 (2012) pp. 155-175.
doi: https://doi.org/10.1016/j.ymssp.2012.03.017

[11] C. Li, Dynamics of rotor bearing systems supported by floating ring bearings, Journal of Lubrication Technology 104 (4) (1982) pp. 469-476.
doi: https://doi.org/10.1115/1.3253258

[12] R. Holmes, M.J. Brennan, I. Gottrand, Vibration of an automotive turbocharger—a case study, 8th International Conference on Vibrations in Rotating Machinery, Institution of Mechanical Engineers, Swansea, UK, pp. 445–455, 2004.

[13] M. Hemmi, T. Inoue, Effects of characteristics of floating bush bearings on the stability of turbochargers, The Proceedings of the International Conference on Motion and Vibration Control, Saitama, Japan, pp. 979–984, 2002.
doi: https://doi.org/10.1299/jsmeintmovic.6.2.979

[14] R. Kirk, A.A. Alsaeed, Induced unbalance as a method for improving the dynamic stability of high speed turbochargers, International Journal of Rotating Machinery, Article ID 952869, p. 9, 2011.
doi: http://dx.doi.org/10.1155/2011/952869

[15] P. Kamesh, Oil-Whirl instability in an Automotive Turbocharger, PhD Thesis, University of Southampton, Faculty of Engineering and the Environment, Institute of Sound and Vibration Research (2011).
URL https://eprints.soton.ac.uk/188121/1/188121P2767.pdf

[16] W. Köhl, M. Kreschel, D. Filsinger, Experimental and numerical investigations on an automotive turbocharger with a transparent bearing section, 11th International Conference on Turbochargers and Turbocharging, pp. 349-359, 2014.
doi: https://doi.org/10.1533/978081000342.349

[17] B. Schweizer, M. Sievert, Nonlinear oscillations of automotive turbocharger turbines. Journal of Sound and Vibration 321 (3-5) (2009) pp. 955-975.
doi: https://doi.org/10.1016/j.jsv.2008.10.013

[18] L. San Andres, J. Rivadeneira, K. Gjika, A virtual tool for prediction of turbocharger nonlinear dynamic response: validation against test data, Journal

of Engineering for Gas Turbines and Power 129 (4) (2006) pp. 1035-1046.
doi: https://doi.org/10.1115/1.2436573

[19] B. Schweizer, Total instability of turbochargers rotors – Physical explanation of the dynamic failure of rotors with full-floating ring bearings, Journal of Sound and Vibration 328 (1-2) (2009) pp. 156-190.
doi: https://doi.org/10.1016/j.jsv.2009.03.028

[20] B. Schweizer, Oil whirl, oil whip and whirl/whip synchronization occurring in rotor systems with full-floating ring bearings, Nonlinear Dynamics 57 (4) (2009) pp. 509-532.
doi: https://doi.org/10.1007/s11071-009-9466-3

[21] L. Feng, Z. Ming, X. Quanyong, Effects of Semi-floating Ring Bearing Outer Clearance on the Subsynchronous Oscillation of Turbocharger Rotor, Chinese Journal of Mechanical Engineering 29 (5) (2016) pp. 901-910.
doi: https://doi.org/10.3901/CJME.2016.0421.057

[22] L. Chaofeng, Y. Hexing, Z. Shihua, Simulations and experimental investigation on motion stability of a flexible rotor-bearing system with a transverse crack, Chinese Journal of Mechanical Engineering 26 (6) (2013) pp. 1194–1203.
doi: https://doi.org/10.3901/CJME.2013.06.1194

[23] P. Bonello, M. J. Brennan, R. Holmes, Non-linear modelling of rotor dynamic systems with squeeze film dampers—an efficient integrated approach, Journal of Sound and Vibration 249 (4) (2002) pp. 743–773.
doi: https://doi.org/10.1006/jsvi.2001.3911

[24] S. T. Noah, P. Sundararajan, Significance of considering nonlinear effects in predicting the dynamic behavior of rotating machinery, Journal of Vibration and Control 1 (4) (1995) pp. 431–458.
doi: https://doi.org/10.1177/107754639500100403

[25] R. I. Taylor, The inclusion of lubricant shear thinning in the short bearing approximation, Proceedings of the Institution of Mechanical Engineers, Part J: Journal of Engineering Tribology 213 (1) (1999) pp. 35–46.
doi: https://doi.org/10.1243/1350650991542596

[26] K. Gjika, L. San Andrés, G. D. Larue, Nonlinear dynamic behavior of turbocharger rotor-bearing systems with hydrodynamic oil film and squeeze

film damper in series: prediction and experiment, Journal of Computational and Nonlinear Dynamics, 2010, 5(4): 041006.
doi: https://doi.org/10.1115/1.4001817

[27] C. Weng Jen, Rotordynamics and bearing design of turbochargers, Mechanical Systems and Signal Processing, 29 (2012) pp. 77–89.
doi: https://doi.org/10.1016/j.ymssp.2011.07.025

[28] W. Zheng, W. Zengquan, Z. Li, Time-dependent vibration frequency reliability analysis of blade vibration of compressor wheel of turbocharger for vehicle application, Chinese Journal of Mechanical Engineering, 27 (1) (2014) pp. 205–210.
doi: https://doi.org/10.3901/CJME.2014.01.205

[29] J.W. Lund, E. Saibel, Oil Whip Whirl Orbits of a Rotor in Sleeve Bearings, Journal of Engineering for Industry, 89 (4) (1967) pp. 813-823.
doi: https://doi.org/10.1115/1.3610159

[30] C. Biet, R. Baar, Experimental study on ball bearings for exhaust gas turbocharger, 5th Tribology and Effeciency Conference of Győr, pp. 253-272, 2018.

[31] D. Zeppei, S. Koch, A. Rohi, Wälzlagerungstechnologie für Pkw-Turbolader, MTZ - Motortechnische Zeitschrift 77 (11) (2016) pp. 28-35.
doi: https://doi.org/10.1007/s35146-016-0112-6

Acta
Technica
Jaurinensis

Vol. 12, No. 4, pp. 294-305, 2019
DOI: 10.14513/actatechjaur.v12.n4.511
Available online at acta.sze.hu

Reducing Pseudo-error Rate of Industrial Machine Vision Systems with Machine Learning Methods

B. Szűcs[1], Á. Ballagi[2]

[1]Audi Hungaria Zrt., Product Unit Diesel I4/V6,
Audi Hungária út 1., H-9027 Győr, Hungary
e-mail: balazs.szucs@audi.hu

[2]Széchenyi István University, Automation Department,
Egyetem tér 1., H-9026 Győr, Hungary
e-mail: ballagi@sze.hu

Abstract: Nowadays machine learning and artificial neural networks are hot topic. These methods gains more and more ground in everyday life. In addition to everyday usage, an increasing emphasis placed on industrial use. In the field of research and development, materials science, robotics and thanks to the spread of Industry 4.0 and digitalization, more and more machine learning based systems introduced in production. This paper gives examples of possible ways of using machine learning algorithms in manufacturing, as well as reducing pseudo-error (false positive) rate of machine vision quality control systems. Even the simplest algorithms and models can be very effective on real-world problems. With the usage of convolutional neural networks, the pseudo-error rate of the examined system reducible.

Keywords: machine learning; classification; convolutional neural network; machine vision; industry 4.0

1. Introduction

This paper presents the usability of ML *(machine learning)* and ANNs *(artificial neural networks)* in the domain of industrial image processing. The goal of the research is to find, develop and test practical use-cases of ML and AI *(artificial*

intelligence) methods in production, focusing on automotive industry and manufacturing.

Nowadays the high quality standards necessitate the use of in-line, automatic measurement and supervision systems. One of these systems is the vision system, which performs part inspections and automatic measurements. For the simplest task like object detection, or advanced functions like distance and/or angle measurements, position or colour detection, surface scan and measurement, these systems are ready-to-go solutions. These methods are easy to use, when the inspected images are very similar to the images used to configure and tune the system. However, when the images contain unusual parts or external disturbances, the pseudo-error rate of the supervisions system can be increasing. To fight these problems ML and AI methods offers possible solutions.

In the serial production, every day very big amount of data generated by automated systems. The images and the measurement data is stored for years to support the quality assurance. These historical datasets are good starting points of ML and AI methods. In the following sections, we show how to use these data to reduce pseudo-error rate of a machine vision system and we present a potential, real-world use case.

2. Framing the problem

The problem, which the methods presented on, is the following: An automated station, which integrated into the assembly line, checks the electrical connectors of an internal combustion engine. The station checks, whether the connector attached and properly locked, or not. The inspected electrical connector of an internal combustion engine seen on Figure 1. (The part numbers and identifiers are deliberately blurred.)

Figure 1. Inspected electrical connector

The algorithm of the station searches for two parallel edges in a manually predetermined region of interest, these represents the upper edge of the plastic label and the lock of the connector, and then calculates the distance of edges. The edge detection based on the changes of the average pixel values (intensity change) of the picture. (Figure 2, the edges used to the calculation marked green.) If the distance is in a predefined interval, the algorithm classifies the connection as OK. As seen, the connector attached fully and locked, but in some cases, the vision system cannot detect these edges, thus cannot compute the distance, the result will be NOK *(not okay)*.

Figure 2. The measurement of the distance between upper edge of the plastic label and the connector lock

Typical pseudo-errors (false positives) are on Figure 3. For a human inspector it is unambiguous that the connectors are fully attached and locked, but the algorithm of the machine vision system cannot detect one or both of the edges, and cannot place the measuring window on the pictures, thus the result of the inspection will be NOK.

Figure 3. Typical pseudo-errors

The problem is that some cables not properly arranged and they cover the edges, thus the edges are not detectable. The shadows on the inspected area, the changes in lighting or the colour of the material can cause the same effect.

The goal is to reduce these errors by learning high-level representations of the well-attached connector, with which the system still able to recognize the good connections, even when disturbances present in the images, and the edges not detectable.

3. Methods

3.1. Toolbox

We used Python to design, build and evaluate machine learning algorithms and models. Python is an interpreted, high-level, general-purpose programming language, which is very popular in data science, ML and AI. To build models, we used the libraries scikit-learn [1], TensorFlow [2] and Keras. These libraries are open-source and highly supported by the data science and AI community.

3.2. The dataset

The dataset used in this research contains 22755 images. In Table 1, the original ratio of the OK – NOK images shown. The images collected and categorized by the automated control station and the result of thirty days productions.

Table 1. The original ratio of the OK – NOK images

OK	***NOK***	***Sum***
21844	911	22755

3.3. Image pre-processing

The computation cost and the training time are two notable factors when we design and train ANNs. In special cases, like in the manufacturing, a lot of environmental variable fixable. In this case, the set of inspected items is limited to two to three types; the position of the engines, thus the connector's positions varies in a very limited range. That means the region of interest, thus the size of the image is reducible. To reduce the size of the input dimension and to speed up the human inspection too, the images cropped and rotated. The original and the pre-processed images shown on Figure 4, the attributes of the pictures in Table 2.

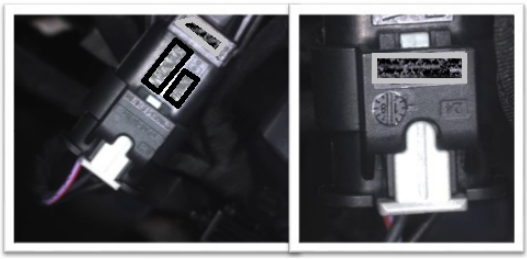

Figure 4. Original and pre-processed image

Table 2. Parameters of the original and the pre-processed images (dimension: input of the ANNs, width x height)

Parameter	***Original***	***Pre-processed***
Width	1200 px	510 px
Height	1000 px	540 px
Size	70 kB	30 kB
Dimension	1 200 000	275 400

3.4. Dataset revision

To determine the true numbers of OK and NOK images, including false positive (false NOK) and false negative results (false OK), revision of the categories had to be made. To speed up the process, we selected the unambiguous pictures with a very useful ML algorithm, the k-means++ [3].

The k-means algorithm mostly used for data mining. It clusters the given data by separating samples in n groups of equal variance, minimizing a criterion known as the inertia, also known as within-cluster sum-of-squares. (Eq. 1.) The algorithm requires specifying the number of clusters; in this case, the number of classes chosen to be two, thus the model separates the unambiguous pictures from those who contains disturbing factors like cables and shadows. The algorithm divides a set of n samples into C disjoint clusters, each described by the mean, or the μ_j inertia of the samples in the cluster [3].

$$\sum_{i=0}^{n} \min_{\mu_j \in C} \left(\|x_i - \mu_j\|^2 \right) \qquad (1)$$

In this case, the similarity measure was the Euclidean distance of the sample and the cluster centroid. From the analysis of the disturbances, it is stated, when an unambiguous disturbing factor, for example a cable over the connector is present, the average pixel value of the sample is highly different from the value of the disturbance free samples. The ambiguous samples, which contains smaller disturbances like partial attachment, we manually reviewed.

The result of clustering the NOK images seen on Figure 5. The plot axes are dimensionless. To represent the samples in a 2D plot, we generated the coordinates from the pixel values of images. To this, we used principal component analysis (PCA) [4]. The PCA is widely used in machine learning. The essence of PCA is to reduce the dimensions of a large data set while keeping the present variance as best as possible.

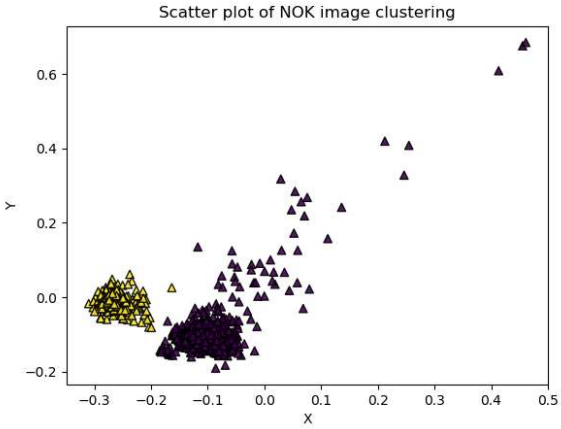

Figure 5. Scatter plot of clustered NOK Images. With yellow: images without disturbing factors, with purple: images with disturbing factors. On the samples in the lower density space, there are no connector at all.

After the clustering, we checked again the category manually, which contains disturbing factors. The results of pre-processing seen in Table 2.

Table 3. Ratio of images after pre-processing

OK	***NOK***	***Wrong pos.***	***Sum***
22582	81	92	22755

As seen, formerly there was 738 pictures categorized as NOK, despite they were truly OK. Wrong positions means that the combustion engine position were wrong, thus on the picture there was no connector at all. If we sum categories NOK and Wrong pos., we will have 173 true NOK pictures, 0.76 percent of total pictures. Theoretically, that means if we train an ANN with these dataset and reach about 98 percent accuracy, the network could categorize all NOK pictures as OK despite still have an accuracy of 98%. To prevent this problem we need more NOK samples for the training, and for that purpose, image augmentation [14] can be the solution.

3.5. Image augmentation

To deal with the problem of having few training images, the data augmentation and image generation is one possible solution. With TensorFlow and Keras it is possible to randomly shift vertically and horizontally, rotate, flip, rescale, zoom-in or zoom-out, brighten or darken images. To do this we used the 173 NOK and 173 randomly selected OK picture as the input of the image generator. The image generator generated the input images of the model in the batch of 32 in every step of every epoch. In this case, we used 25 epochs and 25 steps per epoch, results in a total of 20000 images. With this method, the bias of the OK-NOK rate reducible and the training speed increasable. We used the 80% of the images to train the network, the rest 20% was the validation dataset.

3.6. Convolutional neural networks

To detect and reduce the pseudo-errors we used a convolutional neural network [6]. Convolutional neural networks or CNNs are a special kind of ANNs inspired by biological processes [7]. CNNs are very effective in areas such as image recognition and classification. CNNs used to identifying faces, objects and traffic signs and used in robotic vision and autonomous cars. CNNs use relatively little pre-processing, the network learns the filters that in traditional machine vision algorithms were hard-coded, thus CNNs are independent from prior, human knowledge. These networks learns higher representation of images by learning the filters corresponding to the objects or parts of the image. The output neurons share weights as the same filter is applied but to different image regions, this approach reduces the number of weights used by the network.

The network consists of an input layer, an output layer, and multiple hidden layers. The hidden layers consist of convolutional layers, activation function, pooling layers, fully connected layers and normalization layers. For classification task, the output layer usually have softmax or sigmoid activation. A typical CNN architecture seen on Figure 6.

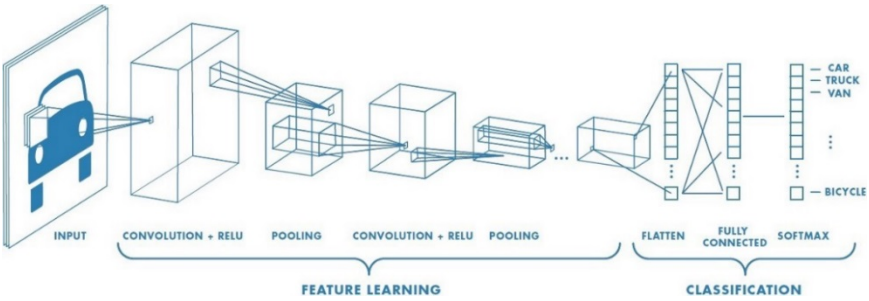

Figure 6. A CNN architecture. [8]

The convolutional layers apply filters to the original image, or to other feature maps in deeper networks. The most important parameters are the number of kernels (filters) and the size of the kernels.

Pooling layers performs the subsampling, a specific function such as max pooling or average pooling, which takes the maximum or the average value in a certain filter. These layers are reducing the dimensionality of the previous layers.

Fully connected layers used to flatten the results of the pooling layers before the activations propagated to the classification layer.

4. The model

The architecture similar to the LeNet-4 models architecture, which is a relative simple, yet accurate model. [9] We fitted the model parameters to the input image parameters. The architecture of the model is the following: after the input layer comes two convolutional layer with ReLU (*rectified linear unit*) activation, the third layer is a MaxPooling layer followed by a Flatten layer, which connects the convolutional part of the network to the fully connected part of the network. The fully connected, also known as the dense part of the network contains three layers, and the output layer contains one node with softmax activation. For the better generalization, we used 20% dropout [10] between the fully connected layers. We tested many dropout rates, but in the literature widely used value, performed the best.

To train the model we used the Keras ImageDataGenerator class. This class responsible for the image augmentation also. We trained the model for 25 epochs, with 25 steps per epoch. In each step, we fed the generated images to the network in the batches of 32 picture. The optimizer was an Adam [11] optimizer, the loss

function is mean squared error and the metric for the optimization is the model accuracy.

For validation, we used another batch of pictures from a second generator. After 25 epochs of training, the validation accuracy was about 90% (Figure 7.).

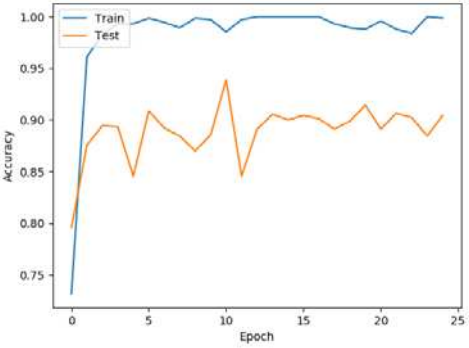

Figure 7. Model accuracy

5. Results

After the training phase, the 911 images, which formerly classified as NOK by the original machine vision algorithm, we fed to the model. The improvement of misclassification rate seen in Table 4.

Table 4: Improvement of misclassification rate

Total Samples	***True NOK***	***Misclassification***	
		Original system	***CNN***
911	173	738 (81.01%)	23 (2.52%)

6. Conclusion

The model is much simpler than the state-of-the-art (VGG [12], CapsNet [13]) image classification models, but for special tasks, it can provide promising results. In contrast with the artificial general intelligence, where the goal is to distinguish and classify as much objects as possible, the goal and the scope of the industrial image processing is well defined and restricted to few cases.

With the use of machine learning, the performance of the conventional industrial image processing systems effectively improvable. If we use the model as the extension of the original system, it reduces the pseudo-error (false positive) rate, thus, reducing the amount of human intervention, and the productivity increases.

The usage of ML methods in production can reduce the manufacturing cost and boost the effectiveness of production, thus besides financial-economic advantages higher levels of production quality can be reached. Researching further potential use-cases and the targeted development of industrial application are highly recommended.

7. Further goals

The further goals of the research besides improving the existing model is to develop and test new and robust models with sophisticated categorisation capabilities. The goal is to reach up to 98% accuracy on categorising true (positive) and false (false positive) errors, and to categorize the true errors.

Acknowledgement

AUDI HUNGARIA Zrt supported the publishing of this paper and the research.

References

[1] F. Pedregosa, G. Varoquaux, A. Gramfort et al, Scikit-learn: Machine Learning in Python, Journal of Machine Learning Research, 12 (2011) pp. 2825-2830.
URL https://dl.acm.org/citation.cfm?id=1953048.2078195

[2] M. Abadi, A. Agarwal, P. Barham et al., TensorFlow: Large-scale machine learning on heterogeneous systems, p. 19, 2016.
arXiv: https://arxiv.org/abs/1603.04467

[3] D. Arthur, S. Vassilvitskii, k-means++: The Advantages of Careful Seeding, SODA '07 Proceedings of the eighteenth annual ACM-SIAM symposium on Discrete algorithms, New Orleans, Louisiana, 2007, pp. 1027-1035.
URL https://theory.stanford.edu/~sergei/papers/kMeansPP-soda.pdf

[4] J. Shlens, A Tutorial on Principal Component Analysis, educational guide, Machine Learning, Cornell University, p. 12, 2014.
arXiv: https://arxiv.org/abs/1404.1100

[5] Y. Lecun, Y. Bengio, Convolutional Networks for Images, Speech, and Time-Series. in: The Handbook of Brain Theory and Neural Networks, MIT Press Cambridge, MA, USA, 1998, pp. 255-258.

[6] K. O'Shea, R. Nash, An Introduction to Convolutional Neural Networks, ArXiv preprint, p. 10, 2015.
arXiv: https://arxiv.org/abs/1511.08458

[7] K. Fukushima, Neocognitron, Scholarpedia 2 (1): 1717, 2007.
doi: https://doi.org/10.4249/scholarpedia.1717

[8] S. Saha, A Comprehensive Guide to Convolutional Neural Networks—the ELI5 way [cited 2019-05-03]
URL https://towardsdatascience.com/a-comprehensive-guide-to-convolutional-neural-networks-the-eli5-way-3bd2b1164a53

[9] Y. Le Cun, L. Bottou, C. Cortes et al., Comparison of learning algorithms for handwritten digit recognition, International Conference on Artificial Neural Networks, in: F. Fogelman, P. Gallinari (Eds.), EC2 Cie Publishers, Paris, 1995, pp. 53-60.

[10] N .Srivastava G. Hinton, A. Krizhevsky et.al., Dropout: A Simple Way to Prevent Neural Networks from Overfitting. Journal of Machine Learning Research 15 (2014) pp. 1929-1958.

[11] D. P. Kingma, J. Ba, Adam: A Method for Stochastic Optimization, International Conference on Learning Representations, arXiv preprint, p. 15, 2014.
arXiv: https://arxiv.org/abs/1412.6980

[12] K. Simonyan, A. Zisserman, Very Deep Convolutional Networks for Large-Scale Image Recognition, arXiv preprint, p. 14, 2014.
arXiv: https://arxiv.org/abs/1409.1556

[13] S. Sabour, N. Frosst, G. E. Hinton, Dynamic Routing Between Capsules, arXiv preprint, p. 11, 2017.
arXiv: https://arxiv.org/abs/1710.09829

[14] L. Perez, J. Wang, The Effectiveness of Data Augmentation in Image Classification using Deep Learning, arXiv preprint, p. 8, 2017.
arXiv: https://arxiv.org/abs/1712.04621

[15] Q. Zhang, M. Zhang, T. Chen, Z. Sun, Y. Ma, B. Yu, Recent Advances in Convolutional Neural Network Acceleration, Neurocomputing 323 (2019) pp. 37-51.
doi https://doi.org/10.1016/j.neucom.2018.09.038

Acta
Technica
Jaurinensis

Vol. 12, No. 4, pp. 306-320, 2019
DOI: 10.14513/actatechjaur.v12.n4.521
Available online at acta.sze.hu

Correlations between Forging Tool Lifetime and the Continuous Curvature Transitions

F. Tancsics[1], T. Ibriksz[1]

[1]Széchenyi István University, Department of Material Sciences and Technology, 9026 Győr, Egyetem tér 1, Hungary
e-mail: tancsics@sze.hu

Abstract: The forged work-piece geometry is determined by different standards and bilateral specifications, so the geometry is not allowed to be changed by the technologist according to their own decision. Therefore, the lifetime of the tool which gives the final geometry is a key issue. The tool lifetime is mainly influenced by technology and process parameters. Regarding these parameters, there are many classical optimization solutions available to increase tool life. In our work, we have looked for a technical device that can complement classic solutions to further enhance the effectiveness in the field of forging tools lifetime. In our opinion, such a technical device may be a continuous curvature of the surface transitions at the preformed geometry. In our work, we investigated the effect of the continuous curvature for a function reducing the forging work at a real geometry.

Keywords: forging; tool lifetime; B-spline; forging force

1. Introduction

Connection between tool surfaces, which take effect on material flow, can be designed with continuity in the connecting points. This continuity is mostly achieved by connecting the tangential of the two endpoints. These endpoints ensure the C^1 continuity in common points of the curves. The result of relationship is the rounding radius, which provides a smooth surface transition. Such a transition is acceptable in general for most applications because of the favourable material flow, minimized wear rate and low forging energy [1][2].

This continuity can be ensured by higher-level connections driven splines as well, which are commonly used in other engineering applications as well [3][4]. An example of this is the connection with continuous curvature between certain surface

elements with C^2 continuity. This C^2 continuity simultaneously provides the criterions of tangential and continuous curvature at the connecting endpoints of curves. In between the endpoints the curvature might constantly change. In fact, this change can be expressed as an angle, which is the degree of the change of the tangential vector relative to the arc length in the instantaneous point on the curve. Therefore, at the connection of a straight and a spline, the initial curvature of the spline should be zero, consequently, the first elementary section of the spline is a straight. This type of curvature may provide smoother transition between surfaces regarding material flow. These latter connection forms were tested on a real preformed and finished 3D forging tool geometry of crown wheel (Fig. 1).

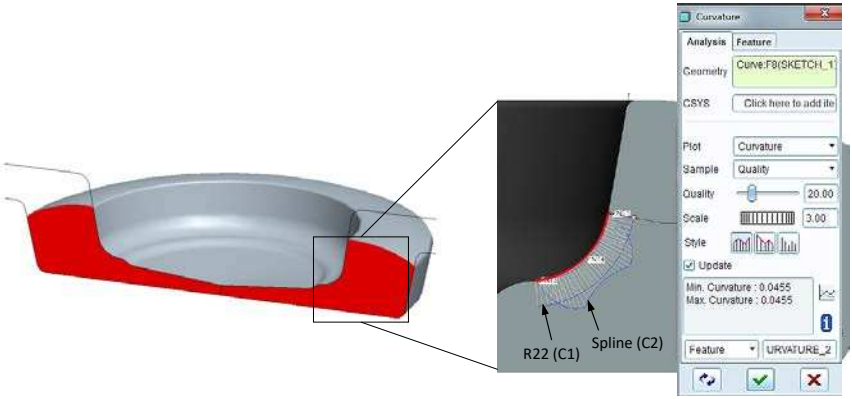

Figure 1. The preformed crown wheel (left) and the curvatures of inspected area (right) are shown with highlighted curvature of R22 radius

In Fig. 1 left a simple forged crown wheel preformed geometry can be seen whereon our concept can be well illustrated. The inspected radius in Fig. 1 right, which is indicated by dark loop, is R22 mm and its curvature is constant (0.0455). The radius is connected tangentially to the other sections on the profile curve. In these endpoints the radius value is infinite, and the value of the curvature is zero. Therefore, the curvature in these points is not continuous. Fig. 1 shows a spline curve as well, with different curvature radius. There is C^2 continuity at the endpoints of spline curve and between the endpoints there is a continuously variable curvature. The question, which of the available spline curves can be more appropriate for replacing the radius, arises. In our point of view, we only need to ensure that the C^2 continuity at the endpoints of spline curve meets and the approximation curve method is used between these points.

This requirement is practically equivalent to usage of cubic B-spline curves [5]. The Pro/E CAD system, similarly to other market leader CAD systems, uses the

NURBS (Non Uniform Rational B-Spline) curves for complex tasks [6]. This type of curve can be simplified according to the curve classes bound together with well-known rational B-splines [7]. Based on these considerations the Pro/E CAD system is a suitable application for function analysis [8]. The selected spline system (in other words: "control point spline method") connects to the sections of the profile curve by continuous curvature and it is locally changeable. The local curvature of the spline curve can be controlled by one or more treadpoints (point on the curve). In Fig. 2 the complete curvature of spline curve can be controlled by three control points or by control polygon (points on the purple lines). It is worth considering to optimize the number of control points to achieve the most even curvature.

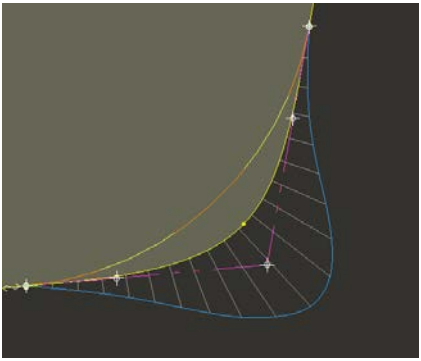

Figure 2. The variable curvature between the endpoints of spline curve

The geometry can be freely variable within certain limits, however, the volume constancy, referring to the initial volume, must be ensured. These variable geometries considering the volume constancy can be ensured with limited extreme value calculation in different CAD solution [9] [10]. Based on volume constancy, the usage of transitions with continuous curvature may be accomplishable as well. We can also specify a maximum allowable curvature (boundary) and we can determine the suitable local position of the control point with limited extreme value calculation. In our point of view, the maximum allowable curvature should be determined based on the radius of the finished geometry. With respect to the modified surface transitions, the Simufact.forming finite element software is suitable for determining which preforming has the less energy demand. This software is a member of Computational Fluid Dynamics (CFD) software family, so in this case it can provide adequate analyses about the incompressible continuum flows along to modified tool surfaces to determine the energy of material motion using numerical approaches.

2. FEM testing on the new surface transition

Our primary goal was to find a detectable decrease in deformation energy or forging force. If it is possible, this value can be optimized later, so the main goal will be available. We produced different spline curves with different curvature between the examined endpoints of the tool surface in the Pro/E CAD system. We wanted to know if we may get a more suitable geometry in terms of material flow instead of the original radius connection. The new geometry is more appropriate for material flow, which reduces the deformation energy and does not influence negatively the flow conditions considered in Ref. [11]. For the required finite element analysis we used the Simufact.forming CAE system (hereinafter referred to as "SF").

2.1. Investigating the lower forging energy

For simulation test we used a maxima crank press equipment with 80 MN nominal force. For the forging technology (e.g. forging temperatures, tact time, material grade, etc.) and tools (e.g. 3D models, surface hardening and roughness, etc.) we used the technological parameters given by Rába engineers. The forging process consists of three steps, upsetting (for descaling) - preforming - finishing, thus we used a multi-stage technology method in the simulation. Except for some pre-process data, the technology cannot be disclosed. The approved pre-process data for publishing, which are enough to understand the energy analysis of the effect of continuous curvature, are the following:

- Imported file formats from CAD system: DXF (Drawing eXchange Format) file formats to simplify the simulation geometry of forging tools
- Selected options for analysis in SF system: Hot forging, 2D axisymmetric, solver type is FE (Finite Elements)
  - The mesh type is AFQ (Advancing Front Quad)
  - The element edge is 1.5 mm
  - The HTC (Heat Transfer Coefficient) value between the work piece and the environment is 50 W/m^2K, the same as between the forging tools and the environment,
  - Forging temperature is 1100 °C, the average tool temperature is 200 °C
  - Tool elasticity assign is: Rigid
- Materials selected from the library of SF: for forging tool it is 55NiCrMoV6 material grade, and for forging piece it is 20MnCr5 material grade with their mechanical, technological and chemical properties.

- The friction mechanism between the tool and the workpiece was approximated by the constant value of Kudo's friction number. This value was set to 0.45 based on the previous tribological studies.

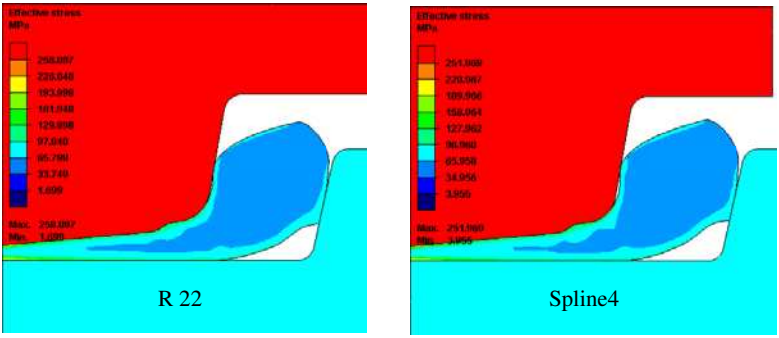

Figure 3. Normal stress distribution differences in case of radius (R22) and spline4 curve in SF system

Fig. 3 shows a simulation result of the normal stress distribution of workpiece in connection with the rounding radius and one of the spline curves. We can state that the acting normal stress on the surface of the tool in the test environment is reduced by Spline4 curve (see Table 1). In addition, it is visible that the work-piece surface is separated from the top tool surface. This effect was typical of all types of examined connecting curves. From this, it can be concluded that the lower part of the connecting curve has a strong effect on the flow of the material. It also means that the distribution of the compression tension in direction of corner radius of the cavity has a higher intensity. This indicates more favorable material flow conditions for filling the cavity. The results in details of the analysis are given in Table 1.

Table 1. Data of forging in case of different curves based on the SF analysis

Name	***Forging process***	***Deformation energy [KJ]***	***Deformation force [MN]***	***Total energy [KJ]***
reference (radius)	preforming	604.565	18.324	1101.993
	finishing	497.428	78.05	
Spline2	preforming	613.536	18.708	1113.129
	finishing	499.593	77.562	
Spline3	preforming	627.846	18.839	1140.577
	finishing	512.731	77.346	
Spline4	preforming	597.472	17.789	1108.375
	finishing	510.903	78.626	

The energy data for the simulations are summarized in tables. These data represent the maximum values at the end of the stroke. As we only need this data, we disregard the shape of the energy diagrams. The same consideration refers to force-related values as well. From the data in Table 1, it can be concluded that the needed preforming energy and the contact force were reduced together in case of Spline4 [12]. On the other hand, this advantage is lost at finishing forging.

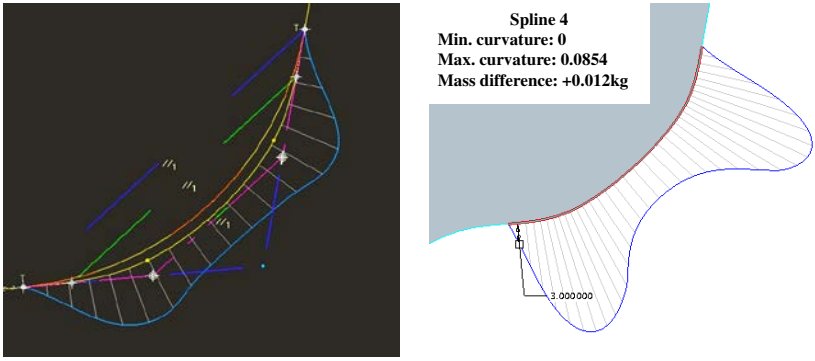

Figure 4. The symmetrical curvature of spline4 curve with two treadpoints

Fig. 4 shows spline4, which provides the local curvature by two treadpoints. Hereinafter, this type of curve is worth examining and this geometry is worth being developed. The difference from the initial mass based on the limited extreme value optimization is +0.012 kg. This weight difference can be reduced later. Two conclusions can be drawn in connection with the continuation of examination. On the one hand, there is a spline curve that reduces deformation force and energy. On the other hand, the analysis should also be extended to the finishing process, and the task should be solved in a complex way. We found a suitable curve geometry to reduce deformation energy so our primary goal is accomplished. In addition, we came to the conclusion that the spline4 curve is worth being further examined.

2.2. Complex examination to decrease the forging energy

In further to reach better results, we should preserve the control point spline method because it guarantees well-controlled positions in the CAD system. The start and end points of spline4 curve coincide with the radius endpoints. Due to preserving C^2 continuity, the points of the spline curve are located on the common tangent crossing through the radius endpoints. If we take 4 control points on these 2 tangents, only 2 variable dimensions have to be changed in a limited extreme value calculation in case of a symmetrical spline (Fig. 4). It is worth examining spline4 curve with asymmetric curvature as well.

In this case three dimensions have to be changed for a limited extreme value calculation. The result of this calculation can be seen in Figure 5. Additionally, it can be seen that approximation of volume constancy has also been improved.

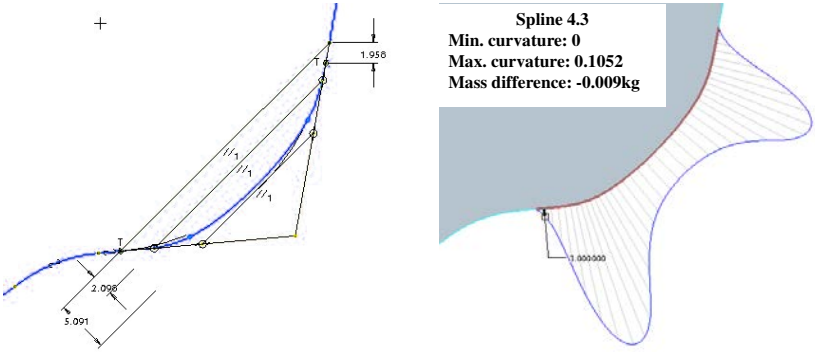

Figure 5. The optimized asymmetrical curvature of spline4.3 curve

The code number 4.3 refers to the 3 variables of the asymmetric curvature of Spline4 curve. In the following section, we examined this type of curve because of better approximation of geometry and greater variation possibilities. However, using multiple variables can result in complicated optimization algorithms as well. Keeping this in mind, our optimization algorithm has been simplified according to the principle of dynamic programming [13]. We have used the minimum values of deformation energy for additional examination in all cases.

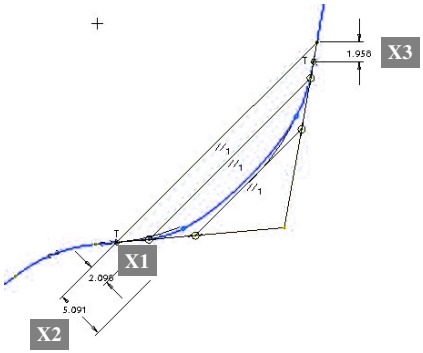

Figure 6. The variable dimensions of the spline4.3 curve

This time with the help of the variables, the new goal is to find the minimum value of deformation work by changing the dimensions (Fig 6). Dimensions X1 and X3 are freely variable. Dimension X2 is already limited by the change in dimension X1.

Based on these conditions, we examined the deformation work in SF system by changing the dimension of X1 and X3. The volume constancy is ensured by parameter X2. With the created curves, the average mass deviation varied around 0.0003 kg. Consequently, the approximation accuracy of the initial mass improved further as well. This approximation accuracy is an already acceptable value. The spline curves named by numbers of the variants. For example, if X1=2 mm and X3=1 mm, the code of spline curve is Spline2.1.

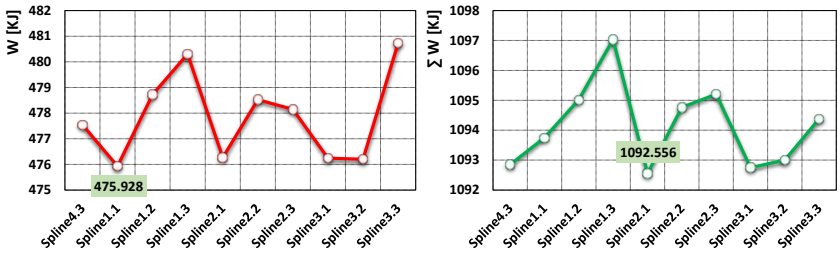

Figure 7. The deformation energy minimum values regarding the finishing forging and the total deformation based on the SF analysis

The variations of range of function were plotted on charts of energy requirements as a function of the final deformational and total energy demands (Fig 7.). Analyzing these diagrams, it can be stated, that Spline2.1 curve has a minimum value on the total energy demand diagram and has an extreme low value on the final deformational diagram. So, this spline curve is worth dealing with.

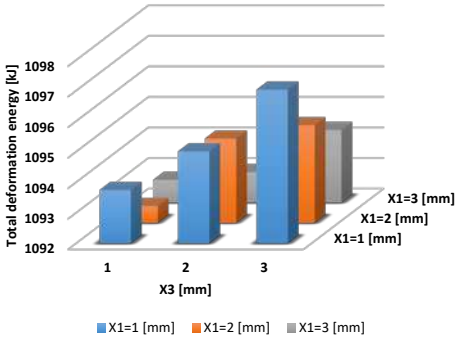

Figure 8. The total energy demand in case of different types of spline4.3 curves based on the SF analysis

The minimum value of total energy demand is shown in a special column diagram as well (Fig. 8). Further energy reduction is possible by improving Spline2.1 curve (Fig 9.).

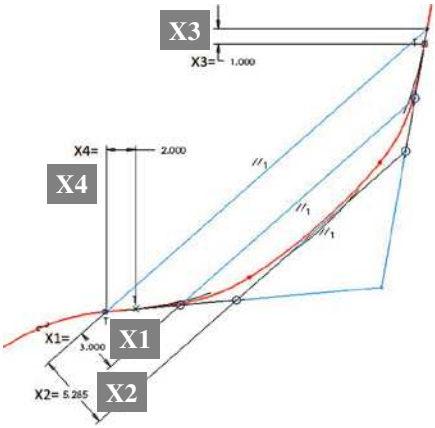

Figure 9. Introducing a new variable (X4) to improve spline2.1 curve

For this we need to introduce a new variable and establish new relationships between the variables. In this relation-system, dimensions X1, X3 and X4 are freely variable, while dimension X2 is limited by dimension X1.

According to the previously applied principle, we examined the energy values by changing dimensions X1, X3 and X4. As before, the volume constancy is ensured by parameter X2. In the examined geometric context we have to formulate the boundary conditions, which are the following:

$$0 \leq X1 < X2, \tag{1}$$

$$0 \leq X3, \tag{2}$$

$$0 \leq X4 < 2.093. \tag{3}$$

Whereabouts: X2 follows from volume constancy, insofar if the value of X4 is greater than 2.093, it would already be defined with another radius, so setting the continuity of the curvature may become complicated. With the created curves, the average mass deviation is alike with Spline2.1, so it is an acceptable value.

We named the spline curves based on the number of variants, as we mentioned it before. For example, if X1=3 mm, X3=1 mm and X4=2 mm, the code of spline curve is Spline3.1.2.

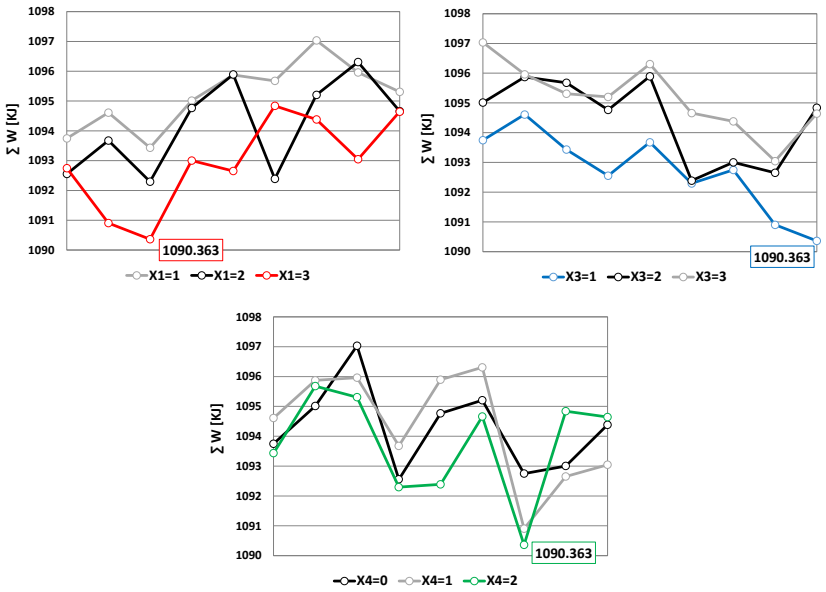

Figure 10. Seeking for spline curve of minimum energy based on the SF analysis

Performing the test for all variations of curves may lead to a dataset that is hard to handle. This dataset should be interpreted purposefully for the effects of each parameter. We continue to apply the principle of dynamic programming as we previously mentioned. From the combination of the minimum curves, the code of the minimum spline curve can be generated, which is Spline3.1.2 curve (Fig. 10). If the dataset is manually processed, we can get the same result. Based on the results of examination, we may state the last simplifying conditions.

- X1 should be increased as long as possible. In the extreme case, the value of X1 approximates X2 with an integer. Value X2 is determined by the law of volume constancy.
- X3 should be set as low as possible. In terms of integers, it is advisable to set X3 to one or zero.
- X4 should be set to maximum integer.

Based on the above findings, the last test was done with the following settings:

$$0 \leq \mathrm{X1} \sim \mathrm{X2} = 4, \tag{4}$$

$$0 \ldots 1 = \mathrm{X3}, \tag{5}$$

$$X4 = 2. \tag{6}$$

The results in details are summarized in Table 2 below.

Table 2. Data of energy in case of different spline types based on the SF analysis

Name	***Forging process***	***Deformation energy [KJ]***	***Total energy [KJ]***
Spline4.0.2	preforming	620.882	1089.96
	finishing	469.078	
Spline4.1.2	preforming	614.646	1090.047
	finishing	475.401	

From the data in Table 2, it can be concluded that the needed settings for giving the minimum summarized forging energy in the overall formula are the following:

$$X1 \sim X2, \tag{7}$$

$$0 = X3, \tag{8}$$

$$X4 = \max. \tag{9}$$

The curve refinements can also be carried out in the form of factionary variables, but no substantial change is possible. Depending on the total work and the refinement of curvature continuity, there is a rational limitation point of energy reduction. Fig. 11 shows this limited relationship between the reducible energy and curvature continuity.

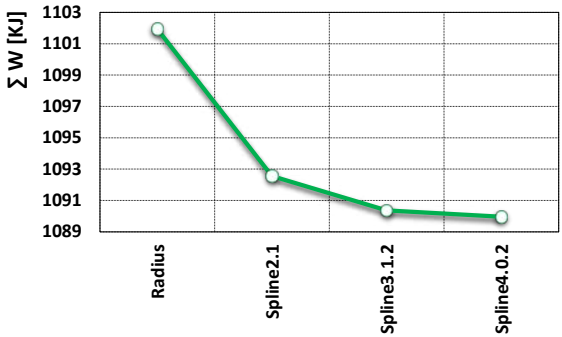

Figure 11. The cumulative forging energy reduction achieved by dynamic programming method.

The curvature of Spline4.0.2 curve is shown in Figure 12. It is worth observing the shape of the curvature which is more favorable for material flow. This geometry has a more favorable effect on sliding systems of metals.

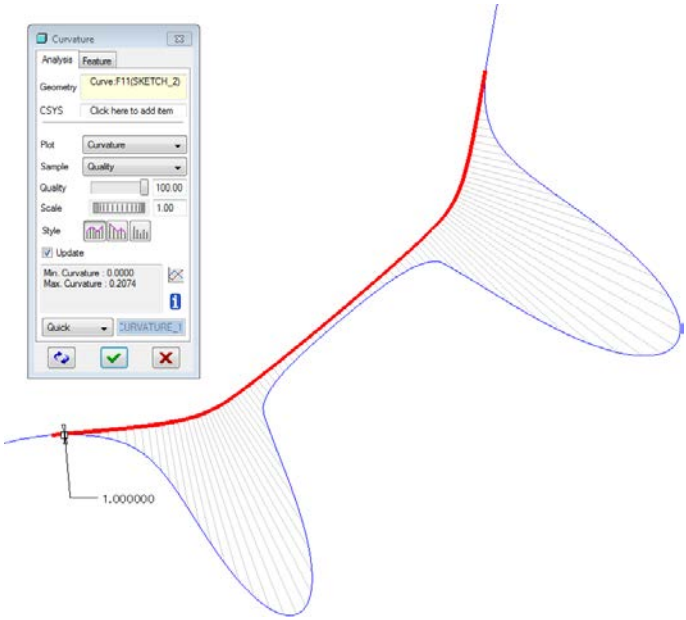

Figure 12. The curvature of Spline4.0.2 curve

For this we need to introduce a new variable and establish new relationships between the variables. In this relation-system, dimensions X1, X3 and X4 are freely variable, while dimension X2 is limited by dimension X1.

Finally, from the data in Table 2, we selected the Spline4.02 curve of the preforming tool and examined the effect of the new geometry on distribution of effective strain rate. This parameter is a good indicator of the state of material flow and filling of cavity. The picture at the top side of Figure 13 is showing the contour line of the original radius of upper tool and the flow lines of material flow in SF system. The picture below it shows the connection with optimized continuous curvature of upper tool and the flow lines of the material flow. The effective strain rates are displayed on the left side of both images. When looking at the pictures, our first impression is that there is no difference between them. Taking a closer look at the distribution of local deformations around the flow lines, the bottom image shows a more even distribution and sometimes smaller value.

All this leads to a slight decrease in energy and a better filling in cavity. Both analyses were made with the same pre-process settings.

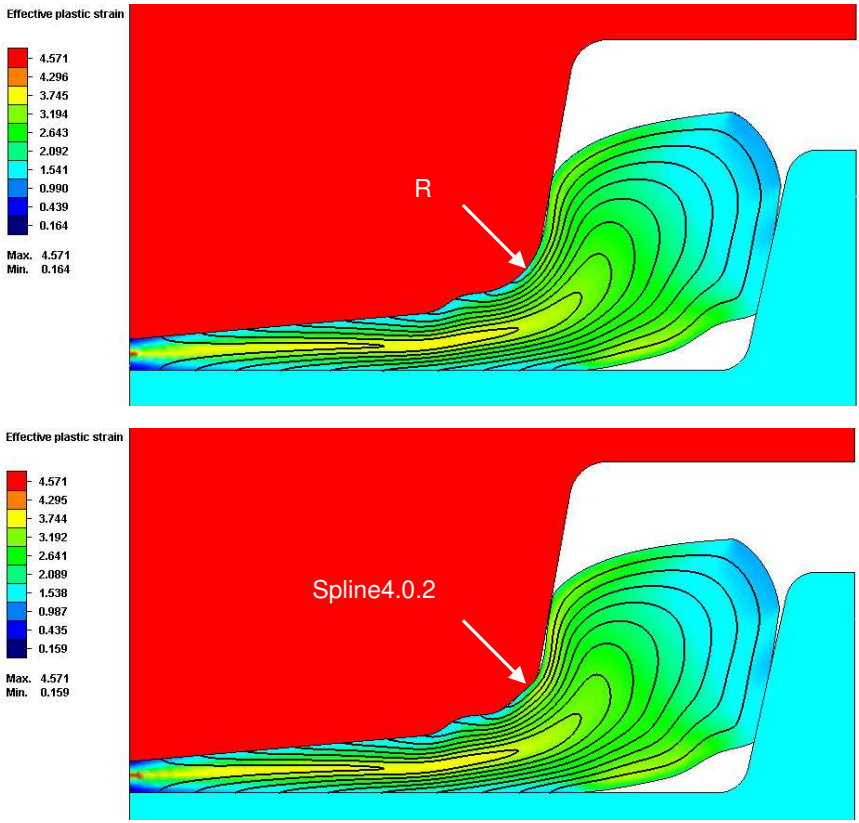

Figure 13. Differences between the original radius and the curvature optimized for the material flow based on the SF analysis

3. Summary and discussion

In our work we investigated whether the surfaces with continuous curvature transitions affect the energy demand of the forging. We proved the existence of this effect, the magnitude of which was about 1% for a given radius. In the first approach, this does not seem to be a great value, but it should not be neglected in case of the radius which most exposed to wear impacts. If the hardness of tools increases by any hardening process, the effect of the curvature may be much stronger as well [14].

We should remember that we only tested one average radius dimension. The effect can also be increased in case of multiple or larger radii. Therefore, our next goal is to investigate the real impact of the presented virtual connection in manufacturing conditions. Summarizing our work, the main goals are fulfilled basically for industrial applications, so the next important step may be the practical adaptation.

Acknowledgement

The paper was written with the support of the project titled "Internationalization, initiatives to establish a new source of researchers and graduates and development of knowledge and technological transfer as instruments of intelligent specializations at Széchenyi István University" (project number: EFOP-3.6.1-16-2016-00017). We would also like to thank Ernő Halbritter PhD and Ádám Futácsi for assisting in connection with the theoretical background of this article.

References

[1] L. Shen, M. Bellus, Numerical Simulation of Multistep Warm Extrusion Forming for the Outer Race of Universal Joint, Journal of Engineering Science and Technology Review 11 (6) (2018) pp. 162-168. doi: 10.25103/jestr.116.20

[2] Y. Chen, Preform Design for Forging and Tube Hydroforming Processes, Ph.D. thesis, Graduate Faculty of North Carolina State University, Department of Mechanical Engineering, (2011).

[3] F. Hajdu, Gy. Molnárka, Parallelization of Numerical Examination of Nonlinear Systems using Maple, Proceedings of the 5th International Conference on Parallel, Distributed, Grid and Cloud Computing for Engineering Dun Eaglais, CCP:111, paper 30, Stirlingshire, UK, (2017).

[4] F. Hajdu, P. Mika, P. Szalai et al., Determination of Vibrations Caused by the Road Profile in Case of a Fire Truck, International Advanced Research Journal in Science, Engineering and Technology 6 (3) (2019) pp. 52-58. doi: 10.17148/iarjset.2019.6310

[5] E.U. Agom, F.O. Ogunfiditimi et al., Cubic B-Spline Collocation and a Domain Decomposition Methods on 4th Order Multi-point Boundary Value Problems, Journal of Advances in Mathematics and Computer Science 27 (1) (2018) pp. 1-7. doi: 10.9734/jamcs/2018/40656

[6] E. Unvert, P. Atkinson, D.J. Tancock, Applying 3D Scanning and Modeling in Transport Design Education, Computer-Aided Design & Applications 3 (1-4) (2006) pp. 41-48.
doi: 10.1080/16864360.2006.10738440

[7] B.T. Bertka, An Introduction to Bezier Curves, B-Splines, and Tensor Product Surfaces with History and Applications, 1st Edition, University of California, Santa Cruz, (2008).

[8] J. Wronecki, Surface Modelling Techniques for Automotive and Product Design, 1st Edition, East Tennessee State University, American Society for Engineering Education, (2007).

[9] F. Tancsics, Development and Practical Implementation of Basically Computer-Aided Design Methods of Virtual Forging Technologies, Ph.D. thesis, Széchenyi István University, MMTDI, (2013) (in Hungarian)

[10] F. Tancsics, T. Gergye, E. Halbritter, Using up-to-date softwares in technological improvements and optimisation of multiple cavity forging, Strojnicky Casopis, Journal of Mechanical Engineering 62 (4) (2011) pp. 191-203.

[11] L. Shih-Hsien, U.C. Chai et al., Generalized Optimizations of Two-Stage Forging of Micro/Meso Copper Fastener, MATEC Web of Conferences 185 (00002) (2018) p. 11.
doi: 10.1051/matecconf/201818500002

[12] N. Fois, M. Watson et al., An Investigation of the Relationship between Wear and Contact Force for Abradable Materials, Journal of Engineering Tribology 229 (2) (2015) pp. 136-150.
doi: 10.1177/1350650114545139

[13] V.L. Matos, A.B. Philpott, E.C. Finardi, Improving the Performance of Stochastic Dual Dynamic Programming, Journal of Computational and Applied Mathematics 290 (2015) pp. 196-208.
doi: 10.1016/j.cam.2015.04.048

[14] D.C. Ko, D.H. Kim, B.M. Kim, Finite Element Analysis for the Wear of Ti–N Coated Punch in the Piercing Process, Wear 252 (11-12) (2002) pp. 859–869.
doi: 10.1016/S0043-1648(02)00032-7

Acta
Technica
Jaurinensis

Vol. 12, No. 4, pp. 321-334, 2019
DOI: 10.14513/actatechjaur.v12.n4.522
Available online at acta.sze.hu

Unmanned Free Balloon Flight's Integration into Unmanned Aircraft System Traffic Management

N. Hegyi[1], J. Jósvai[2]

Széchenyi István University, Department of Vehicle Manufacturing,
Egyetem tér 1, H-9026 Győr, Hungary
e-mail[1]: hegyi.norbert@sze.hu
e-mail[2]: josvai @sze.hu

Abstract: This paper describes and inspects unmanned aerial vehicle, unmanned aircraft system, unmanned aircraft system traffic management, light and medium unmanned free balloons. It presents future safety developments and goals of the European Union's own airspace, but also the Hungarian free route airspace. The development and realization of Swiss U-Space is discussed. Hungarian flights statistics are analyzed. Based on statistics, realized and under development solutions there are recommendations in the paper for the integration of the flight tacking for the mentioned balloons. A real flight tracking test has been done and it is shown in this paper. Its properties are analyzed with conclusions for possible usage.

Keywords: unmanned aerial vehicle; unmanned aircraft system traffic management; unmanned free balloon; U-Space; tracking

1. Introduction

This paper investigates the possibilities of the integration of light and medium unmanned free balloon flight tracking into unmanned aircraft system traffic management. Firstly, in this introduction the main terms as unmanned aerial vehicle (UAV), unmanned aircraft system (UAS), unmanned aircraft system traffic management (UTM), unmanned free balloons need to be clarified for further understanding. Safety developments for the European airspace are described. The Hungarian free route airspace and Hungarian flights statistics are analyzed. Later on

a real flight tracking test is shown and its properties (accuracy, continuity, reliability) are analyzed for possible usage. Conclusions are drawn from these results.

1.1. Unmanned aerial vehicle

Unmanned aerial vehicle as they name suggests are aerial vehicles, which have no human operating personal on board, and are flying remotely or autonomously. They can be classified by a wide range of features, for example by weight, or engine type. The mass of them ranges from a few grams to multi-ton aircraft [1]. Their flight altitude extends from the ground up to the jet aircrafts'. Rotorcraft designed UAVs are able to float on the spot while the fastest ones can fly with hypersonic speeds [2], [3]. As it can be seen, unmanned aerial vehicles exist in many variants. In this paper the smaller UAVs, commonly called in the last years 'drones' are inspected.

1.2. Unmanned aircraft system

An unmanned aircraft system or UAS includes the unmanned aerial vehicles, their control and support systems. Many of them are currently under development [4].

1.3. Unmanned aircraft system traffic management

Unmanned aircraft system traffic management or UTM is a management system for the autonomous controlled operations of unmanned aerial systems. The UTMs are now mostly under development [5].

1.4. Unmanned free balloons

Unmanned free balloons, as their names suggests are unmanned and fly freely. These devices generally consist three main parts, a balloon, a parachute and a probe. This can be seen in Fig. 1. The photo was taken by N. Hegyi in 2017 at a test flight to check possible technical solution for further flights.

Figure 1. A light unmanned free balloon

Unmanned free balloons should be used in such a way that they do not endanger persons, property or other aircraft. In order to avoid accidents, the balloons need to be designed with a not hazardous structure.

The basic classifying characteristics for light and medium free balloons are:

- They carry a payload of one or more packages with a combined mass of less than 4 kg (light) or more than 4kg, but less than 6 kg (medium);
- they do not contain a package of 3 kg or more;
- they do not contain a package with a 2 kg or more with an area density greater than 13 g per square centimeter;
- and the suspension of the load is provided by a rope or other device with requiring an impact force of less than 230 N to separate the payload from the balloon. [6]

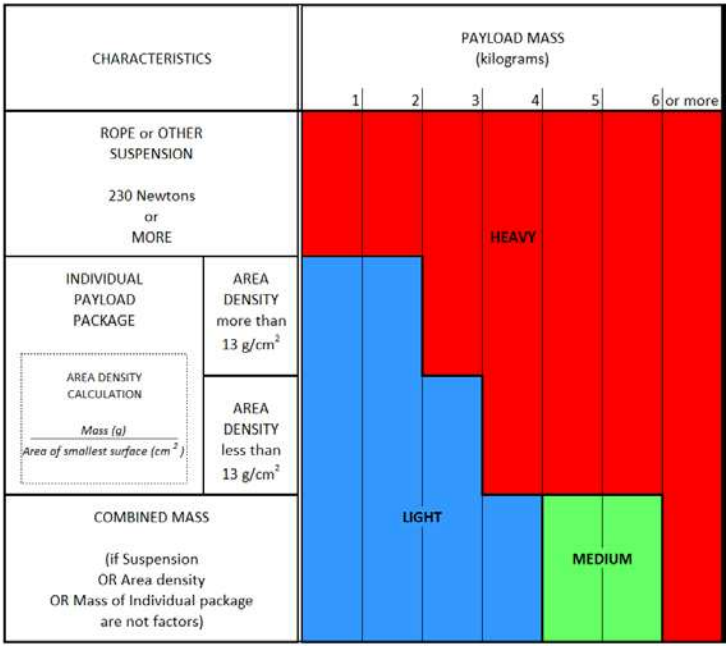

Figure 2. Categorization of unmanned free balloons [6]

This research is concentrating on payloads above 1 kg. In comparison meteorological balloons' radiosondes (which are the payloads) are usually about 40-300 g. To be clear, radiosondes for special purposes can be heavier [7], [8], [9].

2. Tracking

2.1. U-space

The primary purpose of this paper is to demonstrate the integration of authentic tracking of unmanned light and medium free balloons into UTM. U-space is a concept published in 2017 by Single European Sky Air Traffic Management Research (short form: SESAR), which aims the use of UTM through Europe [10].

A previous work by N. Hegyi [11], had already described tracking systems out of these several were used for paragliding, some for drones and some for professional airplane flights. It concluded that the technology used by smartphones could be used partially for the tracking of light and medium free balloons.

In September 2017, the first U-space system was realized in Switzerland. This proved that air navigation services will be capable for the integration of the UAS

into their systems. The goal is to create a system for safe, efficient, and secure access to the airspace for the drones. In a short way the goal is to increase the safety of airspace [12]. This demonstration showed for example in practice the use of e-registration and e-identification, airspace authorization, flight planning, flight management, live telemetry and tracking, the integration into the Swiss Air Traffic Service (ATS) radar system [13].

In March 2018 it was announced that Skyguide (the Swiss air traffic service provider) and AirMap (an airspace management platform for UAVs) will develop and deploy the first national drone traffic management system in Europe [14].

2.2. Free route airspace

Euro-control initiated the development of free route airspace in 2008. The free route airspace (FRA) is a specified airspace. In this airspace a flight route can be planned and defined via an entry point and an exit point, with possible intermediate waypoints for routing. This is possible without any references to the air traffic services route network. In this kind of airspace, the flights are still the subject to air traffic control [15].

In the Commission Implementing Regulation No. 716/2014 the European Union gave a deadline for January 1st 2022 to introduce the FRA [16]. On February 5th 2015, HungaroControl was the first one in Europe to introduce the FRA under the name Hungarian Free Route Airspace or HUFRA [17].

2.3. Air traffic data

The need for integrating of light and medium unmanned free balloons to UTM is supported by flight data.

From Table I in the 'all flights' column (it contains all flights above, to and from Hungary) increased by 31.25 % in comparison of August 2015 to August 2018 [18], [19], [20].

Table 1. Number of flights for statistics

	Flights over Hungarian airspace	**Budapest flights**	**All flights**
August 2015	74201	8685	82886
August 2016	76237	8988	85225
August 2017	81613	9681	98133
August 2018	90198	11049	108791

As it can be seen in Fig. 3 the yearly overflying traffic above Hungary increased by 71.56 % from 2004 to 2017 [21].

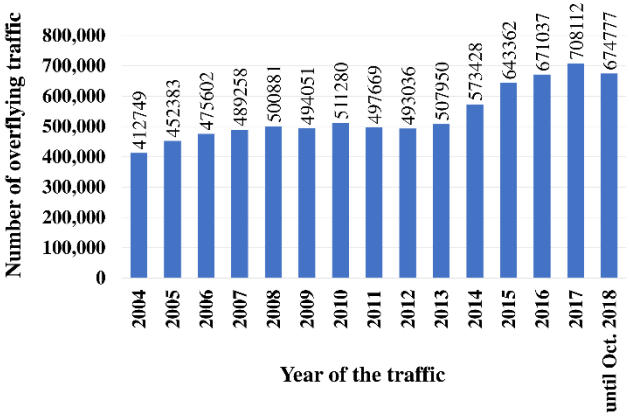

Figure 3. Overflying traffic data above Hungary [21]

As it could be seen in Table I and Fig. 3 the number of flights is increasing, which means that the flight density in airspace is also increasing. In addition, the introduction of HUFRA caused the elimination of specified ATS routes in those defined airspaces. In a sense this causes the possibility to get anywhere in the free route airspace near an airplane. The bigger flight density and the FRA influence in indirect way to increase the danger of a collision by a light or a medium unmanned free balloon with an aircraft.

2.4. Dangerous proximity

In the previous mentioned study by N. Hegyi [11] a near collision of a hobby light unmanned free balloon and an airplane above the USA was mentioned. The balloon got 152 meters close (500 feet) under the jet. This can be seen for far enough, but if an ascent rate of 5 m/s is assumed for a similar situation, and 30 seconds later for the aircraft's arrival at that point than it could have been much closer.

Light unmanned free balloons are not seen on radar by HungaroControl civil air traffic controllers. They are flying without any direct guidance, so only a controlled drone or a jet aircraft can avoid any hazardous close ups or collisions. This paper recommends that if the balloons mentioned here would also contain the electronics required for U-Space, they would increase safety in the airspace, beginning from their release until their landing, in order to avoid potential collisions.

The problem currently is, that the initial phase of U-space systems is working just to a few hundred meters in altitude [10]. The next practical step in this research is to develop a solution for UTM up to an altitude of 18 km. The goal of this altitude is justified by next generation supersonic business aircraft currently in concept studies or under development. Their preferred flight altitude will be 17 km [22].

3. A concept

Previously dangers caused by unmanned free balloons to manned airplanes, like dangerous proximity or the possibility of collisions were already mentioned in this study. The primary objective would be to track the balloons and integrate their positions and flight routes into the UTM.

In the present, for safe flights at the near ground phase of their flights a proper tracking is possible with mobile phone-based technology. This solution would work up to the maximal operating height above ground of 3G-4G mobile phone networks and the equipment used for the 'first steps of U-Space'.

There is also the flight phase of higher altitudes, like 10 km, 20 km above ground or even more. Above the altitude of currently developed U-space there are also some possible solutions. Currently this paper would recommend the use of other radio communication systems.

For practical testing Automatic Packet Reporting System (APRS) amateur radio frequencies are usable. In Hungary one of these frequencies is 144.8 MHz. It needs to be mentioned that APRS tracking is accessible in real-time with Automatic Packet Reporting System-Internet Service (APRS-IS) for example on the website 'aprs.fi'. For realistic testing the HABP42+ balloon tracking device was used for active paragliding flights on 19th and 20st April 2019 near Tolmin in Slovenia. The call sign was N. Hegyi's HA1NX. The flight of 20th April 2019 is a positive demonstration for the APRS tracking. The device was set to transmit tracking data every 70 seconds with a delay of a few seconds (caused intentionally by a few settings). The analyzed data show that after the take off the time between transmissions was 76-80 seconds. Four times this was longer, caused by no possible contact to internet connected receiver stations. The mentioned situations will be analyzed later in this document.

On Fig. 4. the test flight of the 20th April 2019 is shown on GoogleEarth map with satellite image layer. The blue line is the flight route shown by APRS tracking data. The red colored path is the real flight route recorded by the device on a memory card. The flight lasted for 1 hour 9 minutes, its length was about 22.9 km measured in 3 dimensional space. The flight started from a 1085 m high mountain, the maximum altitude was 2059 m, the landing point was at 225 m in a valley. The average speed was 26.05 km/h, the maximum was 56.21 km/h.

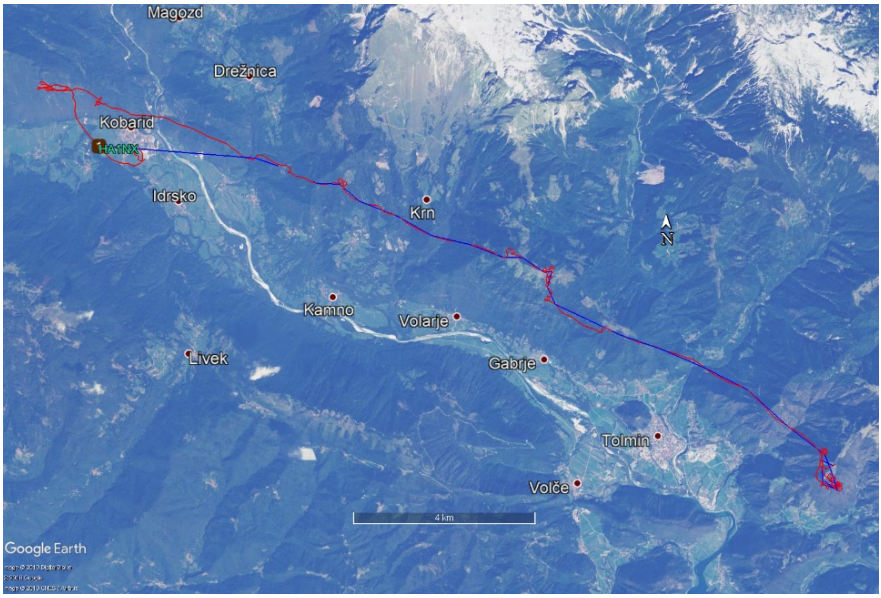

Figure 4. Flight tracking test shown

The beginning phase of the flight is shown on Fig. 5. The blue line is the flight route shown by APRS tracking. The red colored sign – the elevating spiral connected with vertical lines to the ground – is the real flight route recorded by the device on a memory card. The first 12 minutes of the flight can be seen on the image. The spiral flight route is caused by the special paragliding elevation technique with the upward moving air. A spatial difference between the blue and red lines can be seen. The APRS tracking sent a data package every 76-80 seconds and between these packages the real movement was not a straight line, it took place on curved lines. This difference is between 0 to 200 meters. In case of a light or a medium unmanned balloon's flight this difference would be most probably under the 200 meters value. This would be the result, because a balloon's flight has no spiral movement compared to paragliding.

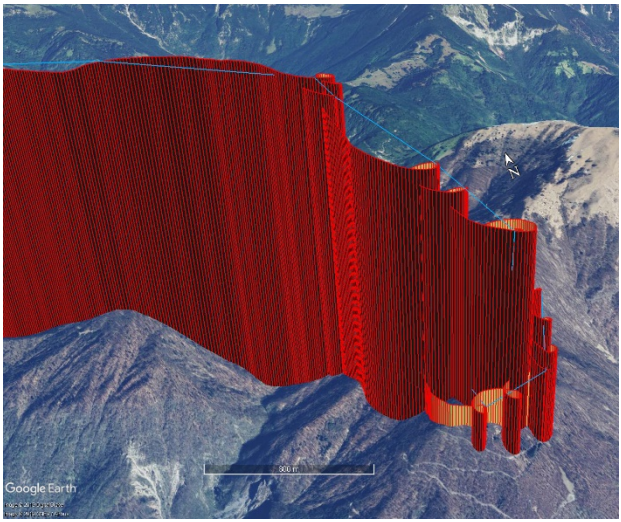

Figure 5. The beginning phase of the flight

On Fig. 6. the middle parts of the flight can be seen. This image shows the difference of the APRS tracking and the real flight in the middle parts of the flight. The red spiral flight route is not connected to the ground.

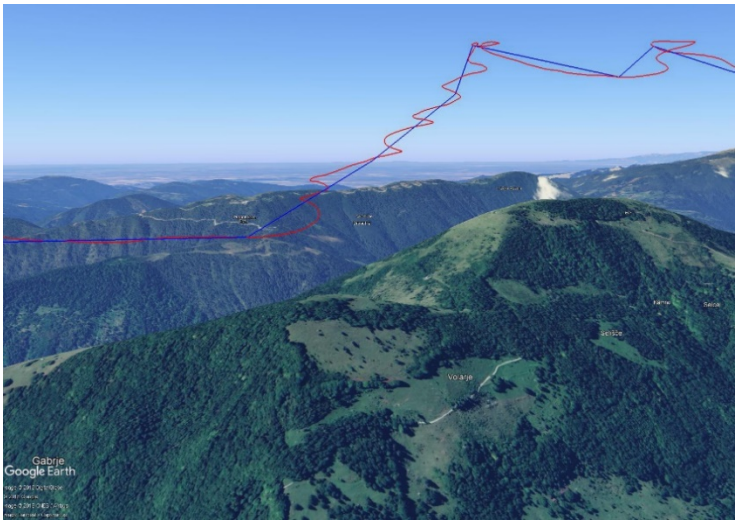

Figure 6. The beginning phase of the flight

On Fig. 4., Fig. 5. and Fig. 6. the difference between the transmitted tracking route and the real flight route can be seen. From the analyzed data it can be seen, that the difference was mainly 0-200m, with 2km partly at the last 17 minutes.

As it was mentioned previously, that the connection to the APRS was lost four times. Two times the time between two tracking points were 2 minutes 40 seconds. This means that, the connection was lost for one tracking data package. It follows that one tracking data package has been sent by the tracking device, but there was no receiver station in connection range for getting the data. The difference between the reported and real flight route was 300-350m which is not significantly bigger than on the more accurate tracking parts.

On Fig.7. the end part of the flight route is shown at the 16 minutes without contact is shown. At that moments on GoogleEarth it can be seen, that mountains were between the paraglider and all receiver stations. The biggest difference between real and received tracking is 2km. Despite of low probability this inaccuracy could cause dangerous proximity between balloons and other aircrafts. This could be solved with a more dense planned network or with a two-mode solution described after Fig. 8.

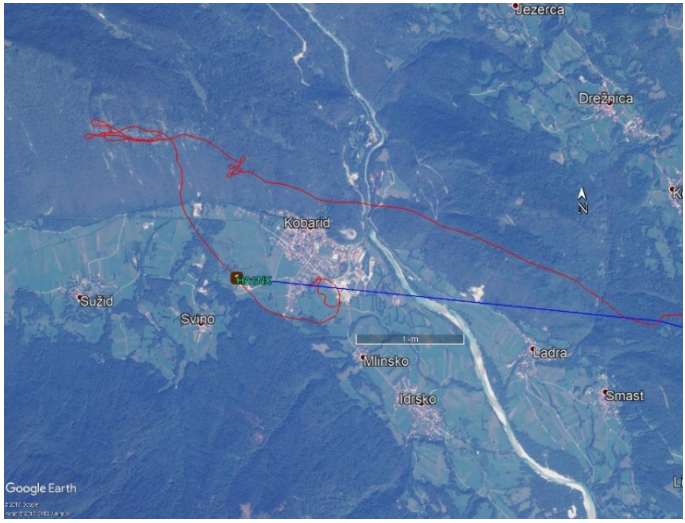

Figure 7. The end part of the flight

On Fig. 8. the same part of the flight is shown on a topographic map, on which the mentioned internet connected receiver stations are also shown [23]. On this map the causes of contact lost can be seen, which are the topographic conditions. At point "A" the connection was made with station S56VIL-10, after this it was out of range caused by the terrain. At point "B" the link was made with station S55AOP-5 (outside the map) from 1094m altitude. After point "B" the tracking connection was

missing for 16 minutes 56 seconds. At point "C" the connection was made again with S55AOP-5 from 631m altitude. After point "C" the tracking was missing at the last 5 minutes. The difference between APRS tracking and the real route was at maximum 2km at "B-C" flight and 1km after "C".

Figure 8. The end part of the flight without connection

With a two-mode tracking system the tracking would be possible by APRS systems at high altitudes, and by 3G-4G mobile systems near ground. The tracking data could be sent by mobile phone-based equipment from altitudes like the APRS untracked last 5 minutes of the flight. To prevent the lose of APRS-IS contact, the improvement of the APRS receiver stations would be needed. On first order, this means more stations, on calculated, planned positions. If this development would be realized, then this technology would be a good option for further usage.

There is a problem with one part of this kind of tracking that needs to be mentioned. A call sign alone does not make the tracking authentic or from another perspective it does not make it enough official for air traffic controllers. There are laws for amateur radio communication which forbid improper use of call signs, but this does not mean, that this would not be possible. It is necessary to search for more authentic solutions [24].

In order to achieve the integration of light and medium unmanned free balloons into UTM, in addition to the necessary tracking equipment an official registration would be needed. This would make the identification of the balloon and the operator possible.

4. Conclusion

At the end of this study the conclusion can be that a two-mode (near ground and high-altitude mode) tracking system should be developed. By the test presented and analyzed in this study it is confirmed, that it can be achieved with further development of already existing tools adapted for this kind of special usage. Near ground mode would be working with 3G-4G mobile telephone technology, and the high-altitude mode would use APRS radio communication. The big step to assure a system, which can be used officially in an authentic way to integrate it into UTM is necessary.

Acknowledgement

The paper was written with the support of the project titled 'Internationalization, initiatives to establish a new source of researchers and graduates and development of knowledge and technological transfer as instruments of intelligent specializations at Széchenyi István University (project number: EFOP-3.6.1-16-2016-00017).

References

[1] M. Hassanalian, A. Abdelkefi, Classifications, applications, and design challenges of drones: A review, Progress in Aerospace Sciences, 91 (2017) pp. 99–131.
doi: https://doi.org/10.1016/j.paerosci.2017.04.003

[2] Airbus, Zephyr (2018), [cited 2018-11-30]
URL https://www.airbus.com/content/dam/corporate-topics/publications/brochures/0296_18_2_ZEPHYR_datasheet_E_horizontal_A4.pdf

[3] NASA, X-43A Hyper-X (2018), [cited 2018-11-30]
URL
https://www.nasa.gov/centers/armstrong/history/experimental_aircraft/X-43A.html

[4] S. G. Gupta, M. M. Ghonge, P. M. Jawandhiya, Review of unmanned aircraft system (UAS), International Journal of Advanced Research in Computer Engineering & Technology, 2 (4) (2013) pp. 1646–1458.

[5] T. Jiang, J. Geller, D. Ni, J. Collura, Unmanned aircraft system traffic management: Concept of operation and system architecture, International Journal of Transportation Science and Technology, 5 (3) (2016) pp. 123–135.
doi: https://doi.org/10.1016/j.ijtst.2017.01.004

[6] EUR-Lex, Commission implementing regulation (EU) No 923/2012, [cited 2018-12-01]
URL https://eur-lex.europa.eu/legal-content/EN/TXT/PDF/?uri=CELEX:32012R0923&from=EN

[7] Vaisala, Radiosonde RS41-D Datasheet B211609EN-D (2018), [cited 2018-12-08]
URL https://www.vaisala.com/sites/default/files/documents/RS41-D-Datasheet-B211609EN.pdf

[8] Meisei Electric. iMS-100 GPS Radiosonde, meteorology, Products (2018), [cited 2018-11-30]
URL http://www.meisei.co.jp/english/products/ims-100-e.pdf

[9] Intermetsystems, iMet-1-ABxn Radiosonde (2018), [cited 2018-11-30]
URL http://www.intermetsystems.com/ee/pdf/202060_iMet-1-ABxn_Data_161006.pdf

[10] SESAR, European drones outlook study - Unlocking the value for Europe, 2016, [cited 2018-02-28]
URL
https://www.sesarju.eu/sites/default/files/documents/reports/European_Drones_Outlook_Study_2016.pdf

[11] N. Hegyi, Safety issues for light and medium unmanned free balloons tracking, Repüléstudományi Közlemények, 30 (2) (2018) pp. 217–224, in Hungarian.

[12] Skyguide, Skyguide demonstrates integration of drones into airspace by means of the U-space (2017), [cited 2018-09-10]
URL https://www.skyguide.ch/en/events-media-board/news/#p9260-9267-9277

[13] Airmap, In Switzerland, U-space takes off (2017), [cited 2018-09-10]
URL https://www.airmap.com/switzerland-u-space-skyguide-demo/

[14] Skyguide, Skyguide & AirMap join forces to develop Europe's first national drone traffic management system (2018), [cited 2018-09-10]
URL https://www.skyguide.ch/en/events-media-board/news/#p13446-13453-13459

[15] Eurocontrol, Supporting European Aviation (2018), [cited 2018-11-30]
URL https://www.eurocontrol.int/articles/free-route-airspace

[16] EUR-Lex, Commission Implementing Regulation (EU) No 716/2014, [cited 2018-10-20]
URL https://eur-lex.europa.eu/legal-content/EN/TXT/?uri=uriserv%3AOJ.L_.2014.190.01.0019.01.ENG

[17] HungaroControl, The most effective version of free airspace management is introduced by HungaroControl firstly in Europe (in Hungarian) [cited 2018-10-20]
URL https://www.hungarocontrol.hu/sajtoszoba/hirek/hungarian-free-route-airspace

[18] Hungarian Air Traffic Statistics, HC Radar - HungaroControl's Magazine, September 2016, p. 17.

[19] Hungarian Air Traffic Statistics, HC Radar - HungaroControl's Magazine, September 2017, p. 17.

[20] Hungarian Air Traffic Statistics, HC Radar - HungaroControl's Magazine, September 2018, p. 17.

[21] HungaroControl's Flight Statistics [cited 2018-10-20]
URL https://en.hungarocontrol.hu/about-us/air-navigation-services/statistics

[22] Y. Sun, H. Smith, Review and prospect of supersonic business jet design, Progress in Aerospace Sciences, 90 (2017), pp. 12–38.
doi: http://dx.doi.org/10.1016/j.paerosci.2016.12.003

[23] aprs.fi, [cited 2019-04-25]
URL
https://aprs.fi/#!mt=roadmap&z=13&ts=1555718400&te=1555804800&call=a%2FHA1NX

[24] 15/2013 (IX. 25.) NMHH Decree on Amateur Radio Service (in Hungarian) [cited 2018-12-19]
URL
https://net.jogtar.hu/printiframe?docid=A1300015.NMH&targetdate=&printTitle=15/2013.%20%28IX.%2025.%29%20NMHH%20rendelet

Acta
Technica
Jaurinensis

Vol. 12, No. 4, pp. 335-346, 2019
DOI: 10.14513/actatechjaur.v12.n4.512
Available online at acta.sze.hu

Development of a Procedure for the Validation of Statistical Energy Analysis Simulations

D. Sipos[1], D. Feszty[2]

Széchenyi István University, Department of Whole Vehicle Engineering
Egyetem tér 1., 9026 Győr, Hungary
[1]e-mail: sipos.david@ga.sze.hu
[2]e-mail: daniel.feszty@audi.hu

Abstract: This paper describes the development of an NVH measurement procedure that can be used for comparisons to Statistical Energy Analysis (SEA). In SEA, the outputs of the simulation are ensemble averaged quantities for each subsystem, which can be obtained in measurements by averaging some measurement point results. For several reasons, the number of measurement points must be as few as possible, but at the same time, they have to provide a well approximated averaged response of the system. The sufficient number of evaluation points and excitation load cases are determined via Finite Element (FE) simulations. It is shown that in case of a simple, flat plate, 17 randomly chosen evaluation points in at least 3 load cases are enough to properly approximate the SEA results.

Keywords: SEA; NVH measurement; comparison; finite element method

1. Introduction

In recent years, the determination of the Noise, Vibration and Harshness (NVH) characteristics of complex structures, such as road or air vehicles via simulation methods have become one of the most important fields of technical development in the industry [1]. These structures are subjected to a wide range of excitation frequencies during their operation [2]. To calculate the low-frequency behaviour, Finite Element simulation is a commonly used tool, however, as the frequency increases, smaller elements must be used, which leads to a significant increase in the number of degrees of freedom. [3] Thus, Finite Element Method becomes prohibitive because of the excessive computational cost. Furthermore, the assumption of a deterministic behaviour for these systems is no longer valid beyond

a certain frequency range [4]. Fortunately, there are several alternative methods for high-frequency vibro-acoustic problems, such as Statistical Energy Analysis [5].

Statistical energy analysis gives the opportunity to calculate the medium- to high-frequency dynamic response of vibro-acoustic systems. It utilizes the spatially and frequency band averaged vibrational energy over a subsystem as the primary variable of the power balance equation system, defined by [5]:

$$\boldsymbol{P} = \omega \boldsymbol{C} \boldsymbol{E}, \tag{1}$$

In Equation (1), $\boldsymbol{P}$ and $\boldsymbol{E}$ are the vectors of injected power and the vibrational energy levels of the subsystems, respectively. The injected power is defined as a rain-on-the-roof excitation, which can be approximated as uncorrelated nodal forces. In an analogy to heat conduction, the vibrational energy can then be considered to propagate as though heat between subsystems in heat transfer. The coupling and damping coefficients are defined in matrix $\boldsymbol{C}$, while ω is the central frequency of the considered band. Figure 1 illustrates the graphical representation of an SEA model. [6]

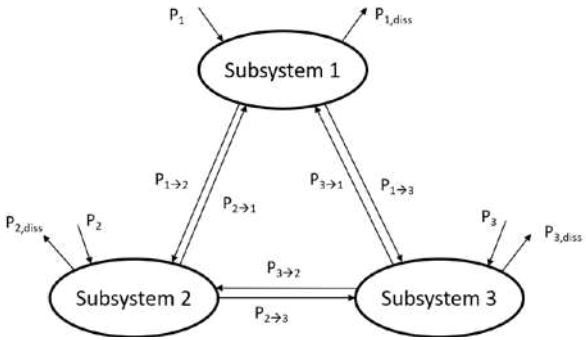

Figure 1. Representation of a SEA model [6]

Each subsystem is defined as group of similar modes, i.e. having homogeneous vibrational energy distribution in the response, or having similar damping loss factor, which must be much higher than the coupling loss factors to the other subsystems. Another key assumption of SEA is that there are enough eigenmodes in the frequency band, so that statistical behaviour of the system can be assumed [7]. This technique gives computationally affordable solutions at high frequencies, because the number of degrees of freedom are independent from the wavelength [5]. Moreover, the matrix of coefficients can be a sparse, diagonal dominated, symmetric matrix, which is well conditioned to make the calculations numerically even cheaper.

Regarding the complex vibro-acoustic structures, numerical simulations are not yet ready to completely replace the experiments, especially in the mid- and high-frequency range. Therefore, measurements are still necessary to prove that the dynamic and acoustic behaviour of the system is as it is expected. Measurements are also used for the validation of simulations. In case of a Finite Element Analysis, it is straightforward to compare the results to experiments. Regarding the excitation in FE simulation, a point force can be applied anywhere on the structure, while in measurement, applying a shaker at the same position is equivalent. At the output points in measurements, accelerometers can be attached to the structure and then the frequency response functions are calculated by the testing software [8]. Figure 2 shows a schematic representation of a general measurement set-up.

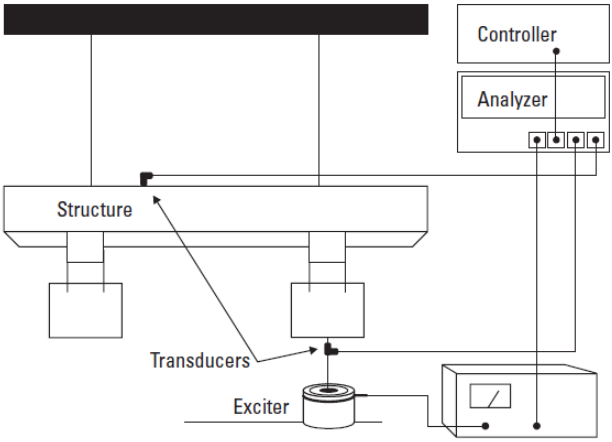

Figure 2. General test configuration [9]

However, in case of a high-frequency method like SEA, the comparison to experiments is more difficult. It is because only an averaged energy level of the subsystems is calculated, from which an averaged panel velocity is derived. As the excitation, a single point force cannot be applied at a certain position, it is distributed along the whole panel to obtain rain-on-the-roof excitation [6].

From these, it seems that some averaging of the measurement results is necessary, but there is no rule in the literature on how many outputs and load cases are required for this. In most cases, the number of the accelerometers and the measurement tools are limited, so is their availability. Furthermore, applying too many sensors at the same time could lead to high distortion in the frequency response functions, especially at higher frequencies, because of the additional mass loading [10].

Therefore, the goal of this paper is to propose a novel measurement procedure for validating SEA simulations. The method is demonstrated for a thin, flat plate. The aim is to determine the number of the required output points, as well as a sufficient number of load cases, from which a well approximated response of the panels can be obtained for comparison to SEA results. A special feature of the paper is, that in order to prove the concept of the measurement methodology, Finite Element simulations are used instead of real measurements, because its output is in the same format as measurement data would be.

2. Determination of the number of required evaluation points

The study was performed on a simple flat plate. Its dimensions were 550 x 650 mm, with the thickness of the plate being 2 mm. A general steel material was defined, which has the following properties:

- Young's modulus: 210 000 MPa
- Poisson's coefficient: 0,3
- Density: 7 850 kg/m^3
- Structural damping coefficient: 0,01

The plate was meshed with 10 mm linear quad elements. Figure 3 shows the assembled FE model; it consists of 3575 element and 3696 nodes in total. First, the sufficient number of outputs were determined, thus only one load case was defined. The excitation node was selected via random process, it is marked with black square.

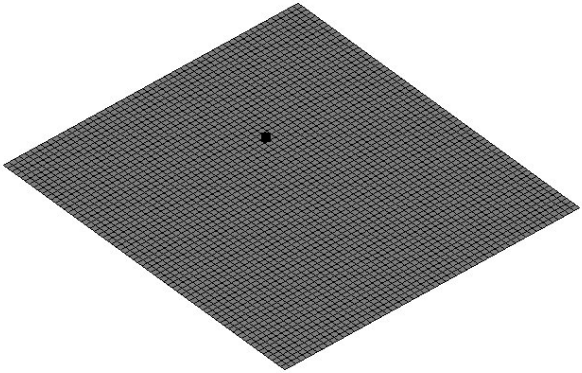

Figure 3. The finite element model, excitation node

The simulations were performed up to 1 kHz in Virtual Performance Solution (VPS) by the ESI Group. A pre-processing script was developed, which has the

possibility to set whether the excitation is fix or randomly selected, how many outputs are requested and whether they are randomly scattered, or are the same in each load case. First, the number of outputs was determined by the desired number of results, in this case it was 15. The sequence started from 2 and had to contain the number of all nodes, 3696. According to these criteria, a geometric series rounded to integers resulted the following numbers: 2, 3, 5, 10, 17, 29, 50, 85, 147, 251, 430, 737, 1262, 2159, 3696.. In each case, the outputs were randomly scattered. Figure 4-6 show the illustration of the cases where 17, 147 and 737 output nodes were defined as examples.

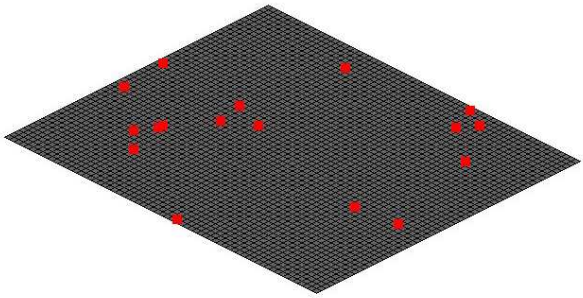

Figure 4. Finite element model, 17 output points

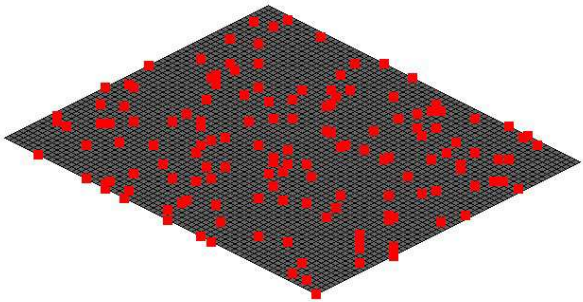

Figure 5. Finite element model, 147 output points

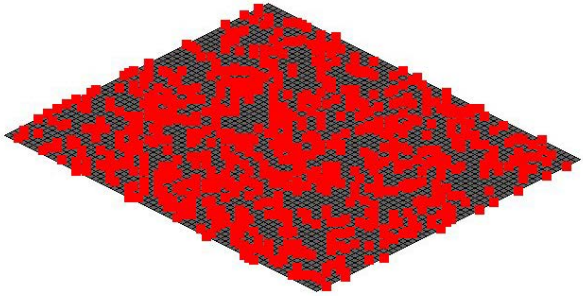

Figure 6. Finite element model, 737 output points

The phase ignored RMS velocity of the output nodes was compared to the reference, which was the RMS velocity of all the nodes, except the excitation node. Figure 7 summarizes all the results. The reference line is the black curve, the brighter the curve, the less output points are contained in the RMS velocity curve.

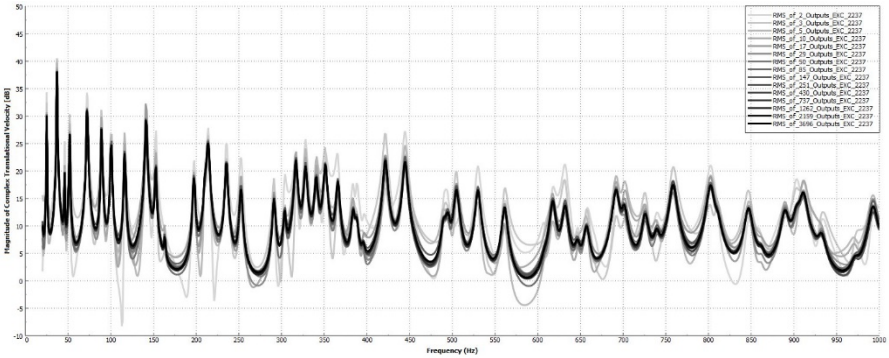

Figure 7. RMS velocities in case of different number of output nodes

It can be observed that although some discrepancies can be detected between the black and some of the brighter curves, the correlation between the darker ones is generally very good. This means that the averaged results converge to the average values of all nodes. Figure 8-10 shows the averaged results for 3, 17 and 737 nodes, respectively.

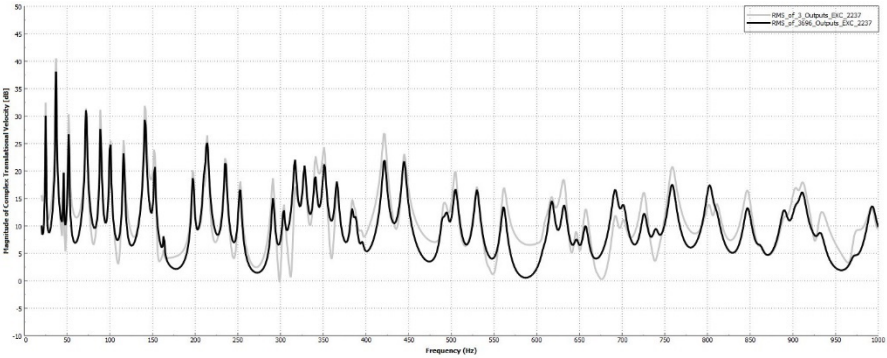

Figure 8. RMS velocity 3 nodes compared to reference

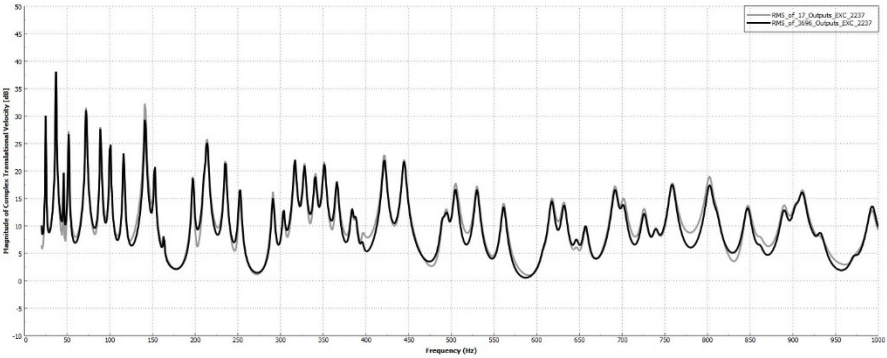

Figure 9. RMS velocity 17 nodes compared to reference

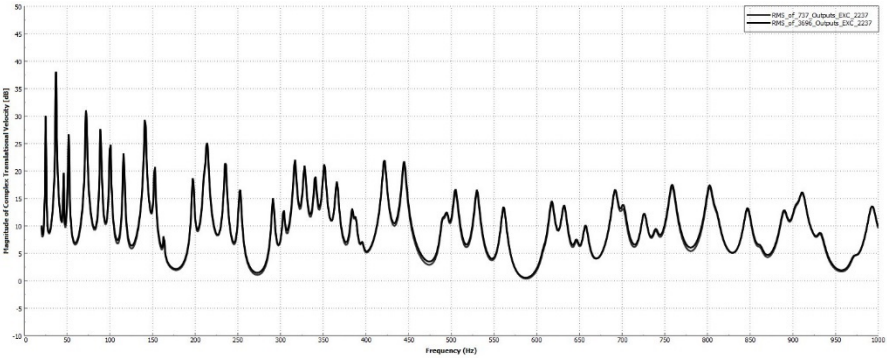

Figure 10. RMS velocity 737 nodes compared to reference

As the results show, the averaged response of 3 randomly chosen output points has quite significant difference relative to the reference curve, but could be adequate, if only a few sensors are available. In SEA, the response of a subsystem is computed in third octave bands, so in some cases a filtered 3-node averaged result could also show acceptable correlation with SEA.

Regarding the averaged result of 737 output points, it gives almost the same curve as the all-node RMS velocity. It can be stated the results will not change beyond this number of outputs. However, 737 measurement points is still too much to realize. On the other hand the 17-nodes averaged result also shows good correlation with the reference curve, and it could be feasible in real measurements as well. It can be concluded that 3 response points are not, but 17 response points are adequate to obtain a well approximated averaged response. Note that applying 17 sensors at the same time on a plate would lead to distorted results, but in a few runs, changing the position of the accelerometers randomly is applicable.

It was also checked that the RMS velocity of 17 output nodes is independent of the position of the nodes. This is shown by Figure 11, where the RMS velocities can be seen in 8 different simulations. In each simulation, 17 different output nodes were selected, while the excitation remained in the same position.

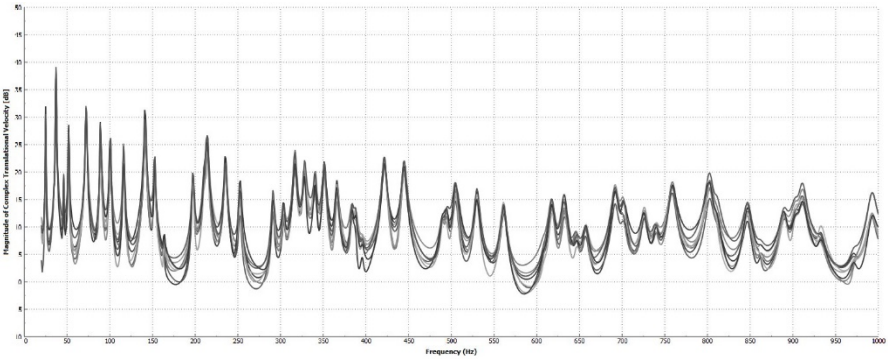

Figure 11. RMS velocities of different 17 nodes in 8 cases

3. Effect of the excitation position

It was proved that 17 randomly selected output points are enough to obtain a well approximated RMS panel velocity, for a given point force loading. But in SEA, the excitation is defined as a rain-on-the-roof excitation, thus it also must be checked that what effect does the position of the excitation on the averaged response of the panel.

In 15 cases, the same 17 output nodes were selected, while the excitation position was changed randomly. The only restriction was that the excitation node must not be near the boundaries of the panel, so the outermost 3 rows of elements (the affected nodes) were excluded from the possible positions. The position of the excitation is selected from the area indicated by blue on Figure 12.

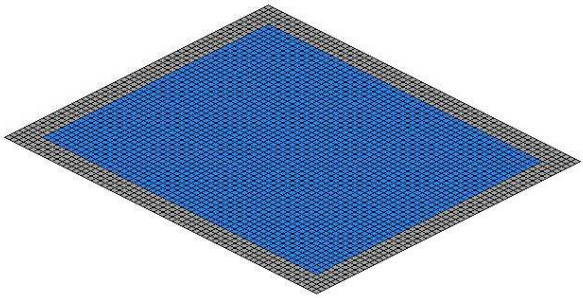

Figure 12. Area of the possible excitation location

The RMS velocities in the 15 cases is shown by Figure 13. It can be observed that between 300 and 400 Hz, and above 600 Hz, there are some discrepancies in the results. Taking the RMS of all the curves results in the red curve on Figure 14.

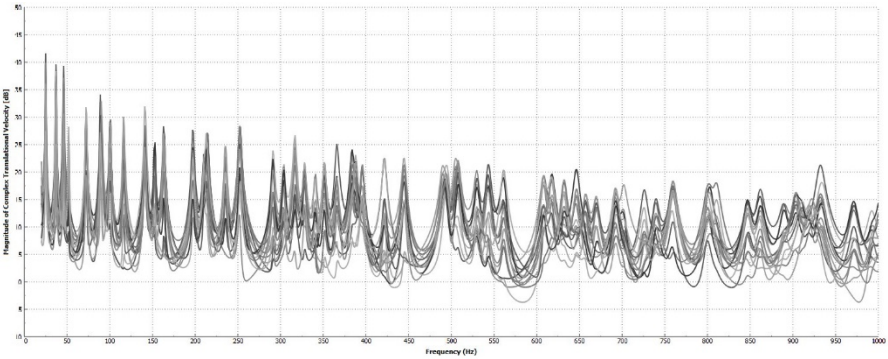

Figure 13. 17-node RMS velocities in 15 load cases

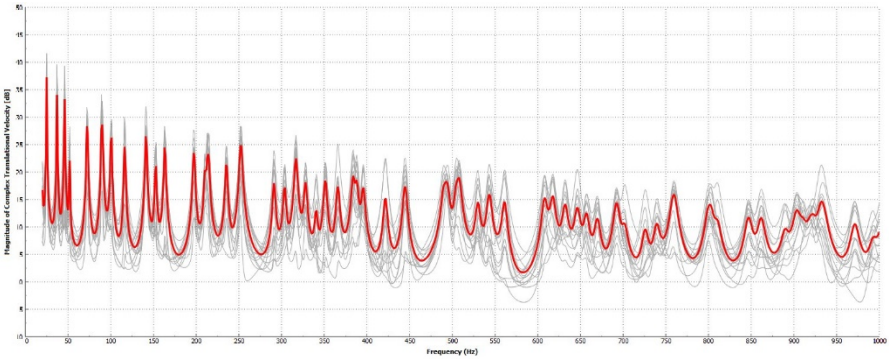

Figure 14. RMS velocity of all nodes in 15 load cases. Red line: RMS of all nodes in all load cases, grey lines: RMS of all nodes in each load cases

The RMS of all nodes in all load cases is the curve, which must be approximated in a fewer number of load cases. Taking the averages of three randomly selected curves gives the curves shown on Figure 15 by yellow, and the red one is the average of all load cases.

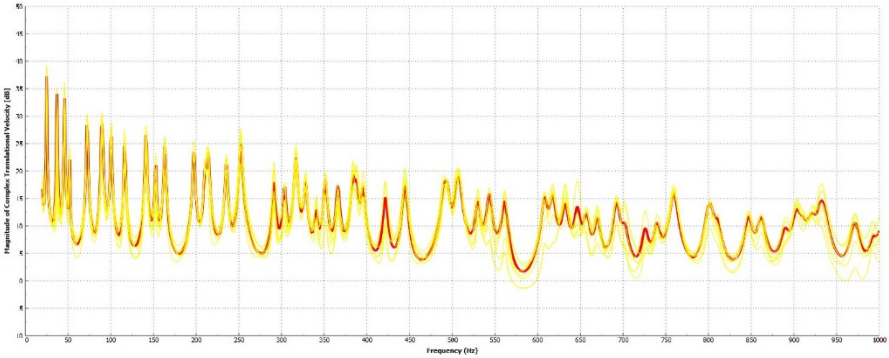

Figure 15. RMS velocity of randomly selected three load case. Red line: RMS of all nodes in all load cases, yellow lines: RMS of all nodes in 3 randomly selected load cases

Any of the yellow curves shows good correlation with the red one. It can be stated that at least 3 different load cases are enough to obtain a well approximated panel velocity, with at least 17 output nodes.

4. Comparison with SEA results

To validate the above-mentioned results, a comparison to SEA was performed. The physical properties of the panel were the same as in the FE simulation. A point force of 1 N magnitude was defined on the plate as the excitation. The averaged panel velocity is shown on Figure 15 (by black colour). The third octave filtered, 17-node, 15-load case averaged RMS velocity is indicated by red and the 17-node, 3 load case averaged result is shown by blue.

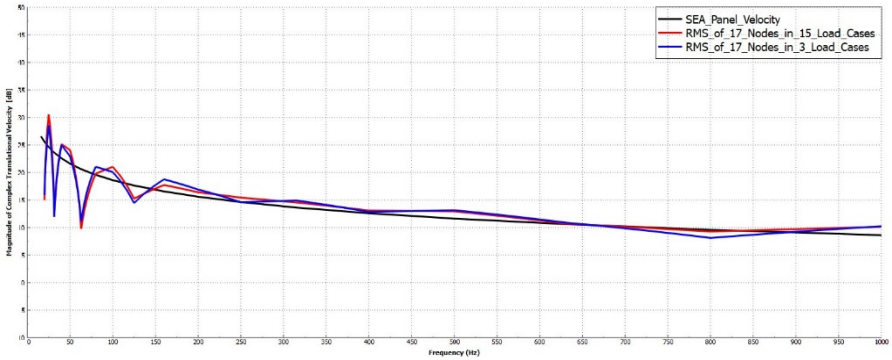

Figure 15. RMS velocity of randomly selected three load cases. Black line: SEA, red line: third-oct. of RMS of all nodes in all load cases, blue line: third-oct. of RMS of all nodes in 3 randomly selected load cases

Good correlation of the results can be observed between the SEA and the Finite Element Method results, regarding both the all-load case averaged and the 3-load case averaged curves. The discrepancies below 150 Hz are due to the presence of global modes and low modal density, that cannot be considered in SEA. The SEA model is valid over 150 Hz, where the main assumptions prevail.

5. Conclusions

An applicable method with high reliability was developed to compare NVH measurements or Finite Element Simulation with minimal output request to SEA simulation results. It was shown in this study, that in the case of a flat plate, it is adequate to measure the panel velocity in 17 points to obtain a well approximated average response. This number of accelerometers cannot be applied at once in a single run, because of the mass effect, but it is not necessary. It was also shown that at least 3 load cases are required to exclude the influence of the excitation position. Based on the proposed method, 3 different measurement runs should be performed, with different accelerometer positions in each.

Acknowledgements

This work was supported by the Hungarian Academy of Sciences and Audi Hungaria Zrt. through the MTA-SZE Lendület Vehicle Acoustics Research Group.

References

[1] T-M. Kim, J-T. Kim, J-S Kim, SEA-FEM hybrid analysis for predicting Inter-floor impact noise, Applied Acoustics, 129 (2018) pp. 397–407 doi:10.1016/j.apacoust.2017.08.025

[2] R. Gao, Y. Zhang, D. Kennedy, A hybrid boundary element-statistical energy analysis for the mid-frequency vibration of vibro-acoustic systems, Computers and Structures, 203 (2018) pp. 34–42 doi:10.1016/j.compstruc.2018.05.007

[3] G. Borello, L. Gagliardini, Virtual SEA: towards and industrial process, SAE Technical Paper, 2007-01-2302 (2007) doi:10.4271/2007-01-2302

[4] A. Culla, W. D′Ambrogio, A. Fregolent, S. Milana, Vibroacoustic optimization using a statistical energy analysis model, Journal of Sound and Vibration, 375 (2016) pp. 102–114 doi:10.1016/j.jsv.2016.04.026

[5] A. Cicirello, R. S. Langley, L. Kovalevsky, J. Wiidhouse, The Hybrid Finite Element/Statistical Energy Analysis method in “MID-FREQUENCY” – CAE Methodologies for Mid-Frequency Analysis in Vibration and Acoustics, KU Leuven, Leuven, Belgium, 2012, pp. 233–259

[6] M. Brandstetter, Virtual SEA – Mid and high frequency solutions based on standard FE models, 2018 FFT Acoustic Simulation Conference, Toulouse, France, 2018

[7] P. Shorter, V. Cotoni, Statistical Energy Analysis in Engineering Vibroacoustic Analysis: Methods and Applications, John Wiley & Sons, Ltd., Chichester, West Sussex, United Kingdom, 2016, pp. 339–383

[8] B. J. Schwarz, M. H. Richardson, Experimental modal analysis, CSI Reliability week, Orlando, FL, 35.1 (1999) pp. 1-12.

[9] The Fundamentals of Modal Testing, (2000) Application Note 243-3 Agilent Technologies

[10] N. H. Baharin, R. A. Rahman, Effect of accelerometer mass on thin plate vibration, Jurnal Mekanikal, 29 (2009) pp. 100–111.

Acta
Technica
Jaurinensis

Vol. 12, No. 4, pp. 347-370, 2019
DOI: 10.14513/actatechjaur.v12.n4.513
Available online at acta.sze.hu

Review of Hybrid Finite Element – Statistical Energy Analysis Methods in Vehicle NVH Predictions

M. F. Treszkai[1], D. Feszty[2]

Department of Whole Vehicle Development, Audi Hungaria Faculty of Automotive Engineering, Széchenyi István University, Egyetem tér 1., 9026 Győr, Hungary
e-mail[1]: treszkai.marcell.ferenc@ga.sze.hu
e-mail[2]: feszty.daniel@sze.hu

Abstract: In the vehicle industry, the noise, vibration and harshness (NVH) characteristics of a car are becoming more and more important. In order to control these, it is necessary to know the sources and contributors to the interior noise level. This paper provide an overview of the state-of-the-art on predicting the NVH characteristics of fully trimmed vehicles in the mid-frequency gap between 400 Hz to 1 kHz. It is shown that for this frequency range, typically a hybrid FE-SEA method is used. This method provides a mixture of the advantages of the deterministic and statistical approaches. The first part of the paper introduces the method, followed by an overview of the different fields of usage in the vehicle industry. At the end of the paper, gaps in the knowledge are identified.

Keywords: statistical energy analysis, hybrid finite element-statistical energy analysis, fully trimmed vehicle simulation

1. Introduction

Noise, Vibration and Harshness (NVH) research and development has become increasingly important in the vehicle industry recently. NVH is about predicting and controlling vibroacoustics phenomenon, which constitute a set of complex problems, such as structure-borne noise or airborne noise. Structure-borne noise can cause fatigue of car components as well as interior noise that is audible to the driver. The

sources of noise or vibration occur at various frequency ranges, for example road noise occurs at lower frequency than wind induced noise.

There are also various trends in controlling the undesired vibroacoustics phenomenon. For example, the easiest way to reduce vibration or Sound Pressure Level (SPL) in a vehicle would be to add extra mass to a part participating in the vibration or noise transfer. However, this is problematic nowadays, when one of the main trends in the vehicle industry is to reduce the weight of the car due to the tightening emission standards, such as Euro 7. Also, electric vehicles have special importance from NVH point of view, since the excitation differs both in frequency and location in comparison to the classical internal combustion engine driven vehicles. The electric motor excitation occurs at a much higher frequency, than for combustion engines as well as noise sources, which have been "masked" before, might now become important. Such noise sources include road noise and wind induced noise. For the latter one, the turbulent boundary layer excitation will occur at higher frequencies and will be random. The heavy battery packages will increase the weight of an electric car, calling for the usage of new lightweight materials such as carbon fibre or alloys. At such complex or lightweight structures, one has to analyse the effect of high frequency excitation from structural, fatigue, failure as well as noise point of view. For this reason, electric vehicles require full car simulations, what represent a quite significant computational challenge [1].

From the frequency point of view, it is common to distinguish in vehicle NVH between low-frequency (up to 400 Hz), mid-frequency (400-1000 Hz) and high-frequency (above 1000 Hz) noise. There are quite matured methods established for predicting the low-frequency or high-frequency noise, however, there is no common approach to predict the mid-frequency problem. In this paper, the goal was to provide a comprehensive overview of the simulation methods for mid-frequency NVH problems, with a special focus on one of the most promising methods, the Hybrid Finite Element – Statistical Energy Analysis (Hybrid FE-SEA) method [2].

2. Theoretical background of Hybrid FE-SEA

In NVH, the mid frequency range of excitations is defined as ~400 Hz to 1 kHz and in this region, the dynamic behaviour of a component becomes very important. At low frequencies, the modal density is low, the resonances are individual peaks, thus, it is quite easy to define the eigenmodes. However, when the frequency is higher, the modal density is also getting denser. Therefore, the modal behaviour of a component becomes more relevant, while the material inaccuracies and non-constant thickness of a plate gets a higher importance [2]. However, FEM simulations are deterministic methods, and as such, they consider a perfect geometry. During comparison with measurements, one can observe that nominally

identical geometries will yield a different result, raising the question: which one is the best?

In contrast, the Statistical Energy Analysis (SEA) method calculates with statistical background for the various material parameters, such as the density or the thickness. For this reason, SEA can represent more realistically the results of a set of measurements However, in the interest of high quality results, the method requires at least 3 modes per third octave band. This might be difficult to achieve for stiffer (such as beams) or smaller parts. Therefore, the philosophy of the Hybrid FE-SEA method is to combine the strengths of both methods, i.e. to use FEM for stiffer parts and SEA for plate-like structures [2].

2.1. Finite Element Method

The most common simulation method in vibroacoustics is the Finite Element Method (FEM), which provides good results up to 200 - 400 Hz, depending on the complexity of the geometry. The problem is, however, that due to the deterministic nature of the method it is not applicable for mid- and high-frequencies, because small deviation in the material or manufacturing inaccuracies causes big differences in the results. In addition, the models require highly detailed geometries, as well as a quite fine mesh if the target frequency is high, since a finer mesh is required to capture a smaller wavelength of vibration. This leads to high total element number as well as computational costs. Since the lowest eigenmodes are the most important ones due to their high amplitude response, which can cause fatigue, these play great role in vibroacoustic analysis. However, Finite Element Method is still the best way to identify the eigenfrequencies and modeshapes, despite the fact that they neglect the uncertainty of manufacturing [2].

2.2. Statistical Energy Analysis

A common method for solving the high frequency domain is Statistical Energy Analyis (SEA). SEA is a statistical method, in which results are averaged spatially as well as throughout frequency. As a consequence, the method neglects most of the details of the model. The lower limit of the applicability of SEA method for vehicles is about 200-400 Hz, because the SEA method needs a modal density of at least 3 modes per frequency band, which means a limitation at smaller subsystems or stiffer parts. In general, the frequency band is a third octave frequency band. Another issue in SEA is the identification of the Coupling Loss Factors (CLF). This value defines the energy loss at a junction, which of course would have an influence on the results. The Damping Loss Factor (DLF) - that is proportional with the subsystem structural damping - can be obtained in a different way, that also impact the results. The pure

SEA is ideal for panel-like structures that have a large number of modal density [2-5].

The application of the SEA is widespread in the industry. Applications range from dishwashers and washing machines [2], to launch vehicles and spacecraft [3]. It has been well demonstrated to be used for predicting interior noise or for noise control treatment design in trains [6], ships [7], aircraft [8], buildings [9] and automotive applications [10], as well as for predicting the exterior noise for electric cars [1].

2.2.1. Theoretical background

The Statistical Energy Analysis was developed in the early 1960's when the vibrational response of a spacecraft launcher was to be predicted. The problem and the geometry were too complex to be solved via FEM. The number of modes of the Saturn launch vehicle was around 500 000 in the frequency range from 0 to 2 kHz [6]. Lyon [11] proposed that the energy flow between two coupled oscillators is proportional to the difference of the vibrational energies. The analogy of the two oscillators is similar to a heat transfer problem. Fig. 1 illustrates the latter one by considering two identical thermally conducting parts [5] [6].

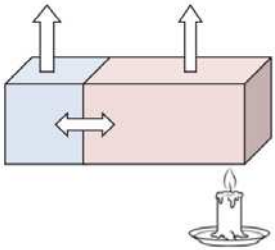

Figure 1. Heat flux analogy to the SEA [10]

According to Fig. 1, thermal energy is injected into the right subsystem, which one part dissipates to the environment, while the other part transfers heat energy into the left subsystem via the coupling. The modal density corresponds to the thermal capacity, the damping to radiation loss, the conductivity to the coupling loss factor and the flow of vibration energy as flow of heat [10].

The word "statistical" in the name of the method refers to the fact that the response is averaged over the subsystem as well as over a certain frequency band (generally 1/3 octave). The energy, which is stored in the subsystem, dissipated or exchanged with other subsystems, is the main variable in the method. There are three approaches to calculate the transmission coefficient: a) modal, b) wave and c) mobility approach [4] [11].

2.2.2. SEA assumptions

Every numerical method has limitations, or is based on assumptions, which have to be taken into account in order to get reliable results in the simulations. The theory of SEA was derived by applying the following four assumptions [5] [12]:

- Rain-on-the-roof excitation
- Large number of modes
- Weak coupling
- Light damping

There are several publications, where the effect of these assumptions on the simulation results were investigated. Le Bot et al. [12] investigated in 2017 the effect of these assumptions on the results. The examinations were illustrated via simple examples. The first example consisted of 6 rectangular plates, with one plate excited by rain-on-the-roof random excitation, while the response was observed on one of the plates. Three calculations were performed: a reference calculation based on a closed equation, an SEA calculation and finally a geometrical acoustic prediction. Results showed that if the damping was light (about 1%), then the SEA prediction was always correct. However, when the damping was strong (about 10%), significant errors appeared. The second example consisted of three rectangular plates with random resonators and coupled through a spring of stiffness K. The coupling strength was controlled by varying K. Two calculations were performed: a) one with SEA, b) one by applying a semi-analytical method. The SEA solution always proved to be correct if the coupling was weak. However, after a certain point, the flow of the energy was reversed, giving negative values, what is physically impossible in thermodynamics. The conclusion of the article was that the first three assumptions can be reduced to a single condition of the diffuse field in all subsystems. The last assumption – weak coupling – is an imperative requirement that cannot be maintained in general.

2.2.3. Statistical Energy Analysis equations

The fundamental idea of the SEA method is to divide the geometry into subsystems, where the equations are solved. At first, consider a single subsystem – eg. a flat plate – into which power is injected via excitation. This subsystem will store some of the vibrational energy, while the rest will be dissipated (see Fig. 2). [4].

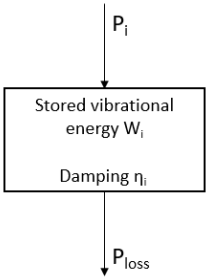

Figure 2. Power equilibirum of one subsystem [4]

The following equation describes this phenomenon [4] [13]:

$$P_{ii} = \omega * \eta_i * W_i \tag{1}$$

Where, P_{ii} is the injected power, ω is circular frequency, η_i is the damping loss factor and W_i is the stored energy in the subsystem. In this case, the injected power equals the power loss, i.e. $P_{ii} = P_{loss}$.

In the case, where two subsystems are coupled to each other (see Fig. 3), the power balance equations will be [4] [13]:

$$\begin{pmatrix} P_i \\ P_j \end{pmatrix} = \omega \begin{pmatrix} \eta_i + \eta_{ij} & -\eta_{ji} \\ -\eta_{ij} & \eta_j + \eta_{ji} \end{pmatrix} \begin{pmatrix} E_i \\ E_j \end{pmatrix} \tag{2}$$

Note that the left side of the equation is the vector of input power, while the right side contains the frequency, the loss matrix, and the energy vector, respectively.

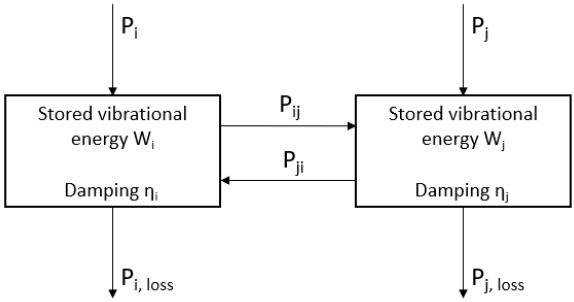

Figure 3. Power equilibrium of two coupled subsystems [4]

2.2.4. Energy of vibration

In SEA, the main variable is the vibrational energy of a subsystem. There are two different subsystem types: structural and acoustic. The structural subsystem energy is given by the kinetic energy [4] [13]:

$$E_i = m_i \cdot v_i^2 \tag{3}$$

Where m_i is the weight of the subsystem, v_i is the root-mean-square velocity, averaged over the subsystem.

The acoustic subsystem energy is [4] [13]:

$$E_i = \frac{p_i^2 V_i}{\rho_i c_i^2} \tag{4}$$

Where, p_i is the root-mean-square sound pressure level (SPL) in the acoustic cavity, marked as V_i. The continuum density is ρ_i and the c_i is the wave speed in the continuum.

2.3. Hybrid FE-SEA

The concept of the hybrid FE-SEA method is to combine the strengths of the two methods. Thus, some part of a subsystem is modelled in FE while the rest in SEA. The part modelled in FE has well defined physical properties, which values are equal over a part. On the other hand, the SEA subsystem has random physical parameters, such as density or geometry, etc. For this reason, the hybrid model contains enough random, or so-called statistical parameters, which makes the system response more realistic [2]. The general guideline for dividing the system is the following: stiffer parts are modelled in FE, since they have small modal density at higher frequencies (for example, the A-pillar of a vehicle). Larger panels, or plates with high modal density are, on the other hand, considered as SEA subsystems (for example, the roof or windows). The SEA subsystems are then coupled to the FEM systems [2][14]. The hybrid FE-SEA subsystem energy balance equations the following [2]:

$$\omega\left(\eta_j + \eta_{d,j}\right)E_j + \sum_k \omega \eta_{jk} n_j \left(\frac{E_j}{n_j} - \frac{E_k}{n_k}\right) = P_{in,j}^{ext} + P_{in,j} \tag{5}$$

The equation based on the original SEA equation supplemented with the FEM equation. The η_j is the damping loss factor of subsystem j, n_j the modal density of subsystem j, $P_{in,j}^{ext}$ the power input.

Different hybrid solutions are being, since both acoustic and structural components can be included in the model [15]. This is a quite new method that alloys the advantages of the two methods. The hybrid method main advantages the model

size is smaller compare to the FEM model, and more suitable for the mid-frequency range. In addition, the hybrid model much faster for a fully trimmed vehicle then the pure FEM, and it give an opportunity to monitories the noise transmission paths in the model [16].

3. Overview of relevant literatures

In the vehicle industry, there are lot of examples on employing SEA as well as the hybrid FE-SEA methods to vehicles. Typically, the investigation of a fully trimmed configuration requires lot of parameters about the structure itself and the poroelastic trim materials, which are defined in the form of Biot-parameters. Therefore, some authors investigated individual parts of vehicle only. The simulation of a passenger vehicle is usually made via hybrid FE-SEA method, while for some larger vehicles, such as a truck, classical SEA is typically sufficient. The following papers review the usage of hybrid FE-SEA methods for Trimmed Body as well as Body-In-White type vehicles.

3.1. Literatures of Statistical Energy Analysis method

Some of the papers in the literature deal with the development of the method itself [20], [25], mainly with improvements of the SEA as a numerical method. The most important parameters in experimental Statistical Energy Analysis are a) the determination of the CLFs and DLFs, b) the proper modelling techniques, i.e. which representation gives the best results for a panel?

Delaere et al. [17] investigated the air gap of an electric motor in 1999 via SEA. The focus was on the stator, so the rotor and the end caps were removed. Two different cases were considered: a) stator without coils, b) stator with standard coil system. The SEA used the experimental data in order to quantify the internal losses in the stator and the coils. This paper is interesting because electric machines rotate at high frequency, and this frequency is too high to fulfil the assumptions of the classical modal analysis techniques. Deleare et al. used inverse SEA to determine the internal energy flow as well as the system properties. The article described the operating condition of the machine, in which the stator teeth were excited by radial reluctant forces caused by the magnetic field in the air gap (Maxwell stress). The teeth transmitted these forces to the yoke without losses. The authors used Power Injection Method (PIM), in which every subsystem is excited, and the response is analysed in every case. Then, the Loss Matrices were calculated from the equations and the subsystems were covered randomly with N accelerometers. The excitation was introduced at a random number of locations, using a shaker or hammer. The analysis concentrated on characterizing the internal loss factors and CLFs.

Fischer's paper on SEA theory from 2006 [6] shown in the mathematic derivation of the kinetic energy, that this is proportional to the mean square velocity. Three averaging methods were introduced. The first one was over the points of the observation, while the second one over the points of excitation, where the information about the shape of the individual eigenmodes was eliminated. Note that as a consequence, the mode shape needs to be no longer considered in SEA. The third averaging was over the frequency of excitation. The author presented a really good analogy of the power balance equations through hydrodynamics. This article is a standard work on SEA, which helps to understand the theory and key aspects of the method.

Sarradj in 2004 [18] listed the most notable advantages of energy-based methods. According to him, energy-based methods are not sensitive to small parameter changes, since energy quantities can be averaged more easily. The goal of the energy-based computations is to determine the energy quantities (SPL). Sarradj described the SEA background and its basics, followed by an example, where the 1st and 4th subsystems were not coupled to each other, so their CLFs were zero. However, in the loss matrix all CLFs associated with power losses were summed. The author introduced two types of SEA, experimental and predictive, which can predict the behaviour of the structure in the early stages of design, when no object is available for measurements. The article highlights the main advantage of the SEA, that is that it can quantify the transmission paths in the system.

Hauer et al. [19] wrote an article about the hybrid approach for a trimmed passenger vehicle in 2004. The hybrid method was used to identify the loss factors within and between the subsystems, by using a Power Injection Method. According the authors, the hybrid method could calculate the tunnelling effect accurately, which means the physically not connected subsystems appeared as though coupled to each other. They investigated how many response data were necessary in order to obtain reliable results. For internal loss factors, 5 response points were enough, while for CLFs 10 points were required. As a conclusion, the authors stated that the hybrid method was a powerful method, especially in the early stages of development, since it allowed to determine accurately the SEA model parameters for complex systems and complex junctions. Another advantage of the hybrid method was that the optimization process used only two subsystems for determining the loss factors.

Different junction types can have a high impact on the Coupling Loss Factors. Panuszka, et al. [20] examined this effect in 2005 by investigating the Coupling Loss Factors between two rectangular plates joined either by a welded line, spot-weld, screw-bolted or riveted junctions. For the line junction, the authors investigated the influence of the thickness ratio of plates. For the point junction, the influence of the point distribution at the junctions was investigated. In the article, the equations of

the junctions were derived. The test case was carried out with care, and the Internal Loss Factor of the plates was measured. The measurements were compared to theoretical equations and in some cases to simulation results as well. The results showed that the CLF values decrease when the ratio of the plate thicknesses is increased, as well as that the point-like junction has the tendency to increase with the density of the joining points. The highest CLF values appeared to spot welds, whereas the lowest to riveted joints. (See Fig. 4.)

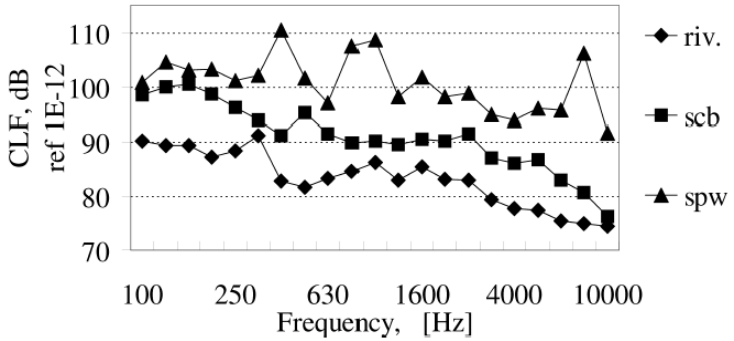

Figure 4. CLF results of different connection types versus the frequency [20]

In 2012, Xin et al. [21] investigated a car interior with SEA, for a vehicle at high speed, where air-borne excitation was the main contributor to interior SPL. They investigated a highly detailed model in SEA, with proper excitations. The acceleration of the engine mounts, and the SPL in the engine compartment were measured at 100 km/h. The air-borne excitation was obtained from CFD simulations, with high attention to the A-pillar and mirror area. The SPL at the driver's headspace was investigated from 200 Hz to 5 kHz. The comparison showed that the average deviation from the measurements was less than 3 dB (Fig. 5).

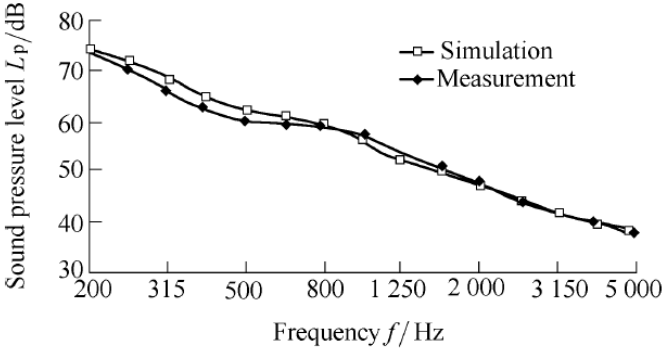

Figure 5. Compariosn of SPL results for an SEA simulation of a fully trimmed vehicle [21] Airborne noise excitation was obtained via CFD

Another objective of the work was to reduce the SPL in the driver headspace. The authors used a material database (AMDV) in order to set up different materials without measurements. There were 9 different load cases, and the results showed that they could reduce the SPL on average by 2,64 dB, except at idling condition where the SPL increased by 2,2 dB [21].

Blanchet and Golota [22] have tried to answer in 2014 the following question: how can one identify the convective and acoustic sources as well as how can the transfer path from the sources to the interior cavity be identified? They used CFD and/or experiment to determine the turbulent flow, so that wind noise sources can be characterized. The investigation focused on the neighbourhood of the A-pillar as well as on the pressure fluctuations around the mirror area. They simulated three independent cavities, which one side was covered by glass and they examined different acoustic models (Corcos model, Diffuse Acoustic Field, Propagation Wavefield). The radiated acoustic power from the side glass was compared to SEA as well as Boundary Element Method (BEM), the results were found to compare quite well. During the wind tunnel test, the average SPL on the front left side glass and also in the interior were measured. When compared to the experiment, good agreement was achieved with SEA in a wide range of frequencies (250 Hz – 8 kHz), by using multiple propagating waves.

Putra et al. [23] worked out an individual method in 2014 to ensure the diffuse field for the SEA in a vehicle interior. They proposed the total energy to be equal to the direct field and reverberant field energies and removed the direct field component from the measurement and modified the DLFs and CLFs values. Fig. 6 shows the background of the analysis.

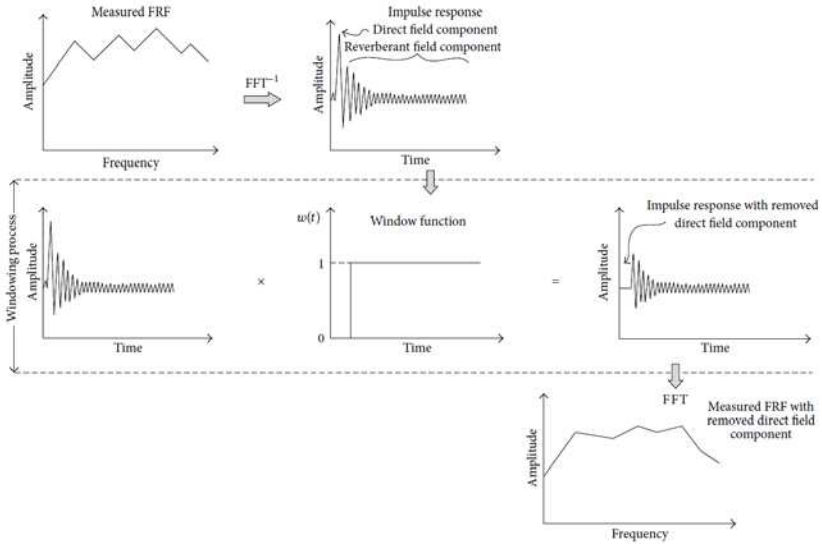

Figure 6. The direct field removing process [23]

They divided the vehicle interior into two subsystems, front and rear cabin. The front seats were the coupling between the cavities. During the measurements, a loudspeaker was used as an excitation, to inject the sound energy into the subsystem. Two cases were investigated: a) excitation from the loudspeaker, b) energy input from the engine at constant RPM. Sound intensity was measured, and the results compared to the classical SEA and to the corrected SEA methods. They tested a midsize vehicle in a semi-anechoic room. The corrected SEA simulations showed good correlation with the measurements, while the classical SEA overestimated the results at 1000, 2000 and 3000 RPM, as illustrated in Fig. 7. [23].

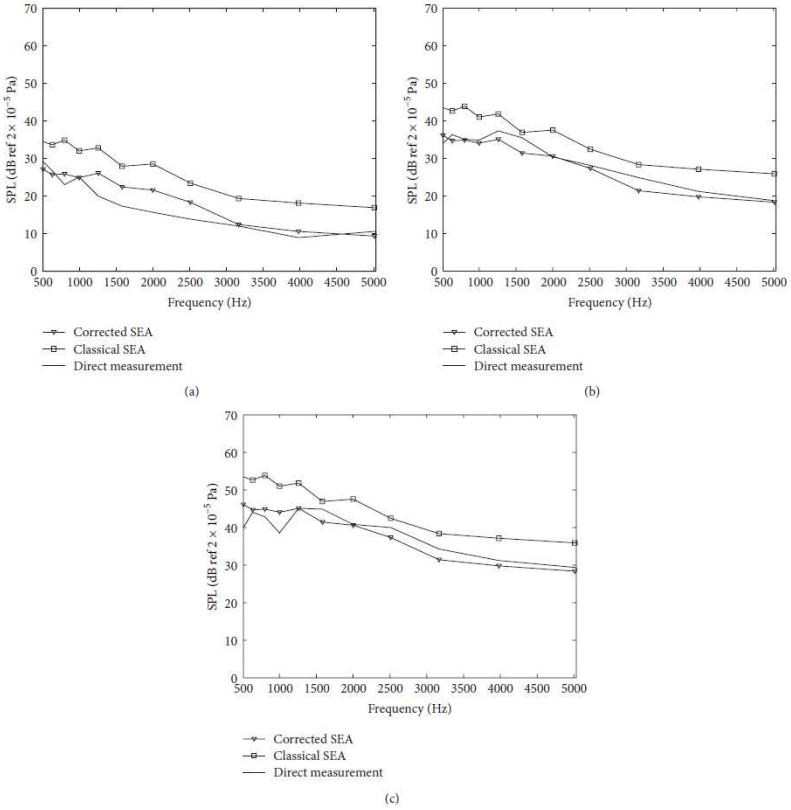

Figure 7. Results of classical and corrected SEA simualtions at the three engine RPMs [23]

With the advent of electric drive systems, the development of electric motors become important from fatigue and vibration point of view. Some papers investigated the problem with SEA only.

A. Bötke et al. [24] investigated in 2015 a fully trimmed electric car in SEA. They focused on the mid- and high-frequency range because of the high-frequency excitation. The road and the wind noise were the most dominant excitation sources, which were modelled as random signals. The authors described the limitations of FEM and explained why SEA is so powerful for these high-frequency analyses. According to Bötke et al., in case of electric cars, the location of the excitations is random, so it is required to analyse the whole vehicle and the whole sound insulation package, which increases the model size and computational costs in FEM. For the

simulation model, various materials were experimentally characterized in terms of the poro-elastic properties (porosity, damping loss factor, etc.) Two different test cases were performed: a) a controlled environment in a semi-anechoic chamber, with a constant spherical sound source between 100 Hz – 10 kHz in the front and rear tire regions, using two different output nozzles; b) closed track tests at three constant speeds (10, 20, 40 km/h). The measurements were performed at the driver head and the rear seat head positions with microphones. The results showed that differences of up to 10 dB could occur between the measurements and simulations. They listed the possible causes of errors, divided them into dependent and independent from the computation.

Gu and Sheng [25] developed a method in 2015 to estimate the CLFs from a structure coupled in series. They used the so-called Energy Ratio Method (ERM). In some cases, however, the original method had numerical problems, so they improved it by identifying a complex coupled system as two coupled systems. The improved method simplified the large matrix into a two-dimensional matrix. The classical ERM can cause negative CLF values, which is inconsistent. The objective of the paper was to substitute a structure consisting of *n*-coupled series by a two-coupled structure, as well as to substitute the loss factors and equivalent vibration energy of the new subsystems 1 and 2. In the experiment, they investigated the loss factors for each subsystem, when only one subsystem was excited. The results showed that there is no negative value in the improved method, compared to the classical ERM, which gave negative results in some frequency bands. Validation with experiments was performed by comparing the vibrational energies with simulations as well as tests of subsystems 1 and 2. The prediction results appeared to be accurate and reliable.

Jang et al. [26] investigated in 2015 a mid-size truck in VA One and compared the results to measurements. They divided the truck into structural panel subsystems and acoustic subsystems, keeping in mind that the SEA subsystems must have at least 3 modes/bands in order to be valid. They considered the ribbing on the plate and the air duct in the pillars. For Noise Control Treatment definition, Biot parameters were applied. The TL for the grommets were specified analytically. If a panel was not an idealized SEA panel, they calculated it by a local FE model. Measurements were made on the road and on a 4-wheel dynamometer. The interior noise level was measured, and the structural and airborne transfer paths were investigated. According to the authors, in this case the air-borne sources could be neglected below 200 Hz, while the structure-borne noise over 2 kHz. During the measurements, sound sources were placed around the vehicle and the SPL was measured at the driver and passenger headspaces. Tests were performed at multiple conditions: idle, wide open throttle for multiple gears, at constant 60, 80 km/h, as well as at steady-state

conditions. The conclusion was that the results correlated well, especially from 300 Hz.

Jang et al. [27] analysed in 2015 the air-borne noise transfer path with SEA of a truck. They optimized the sound package of the vehicle, using multi-layer poro-elastic materials. They identified the Biot-parameters of these by using an impedance tube and FOAM-X. The authors had two objectives: a) to improve the SPL at the driver head space at constant cost, b) to reduce the sound package cost at constant SPL. VA One has a Design Optimization Tool part, which was used to optimize the performance and the cost of the sound package. They measured the truck noise performance before and after the improved sound package implementation. For the beaded panels they used modal correction factors to amend the modal densities. The truck was tested in a semi-anechoic room. In this analysis, the structure-borne sources were not considered, only the air-borne sources. The measurement was performed at 80 km/h at steady-state condition. Results showed that the sound package was enhanced by 3 dB at no additional cost, and that the price of the sound package was reduced by 30% at same SPL.

Jálics [28] wrote a short paper in 2017 about poroelastic materials and their possible mathematical descriptions in SEA. The intention was to determine the Transmission Loss of a plate in SEA through different models and to the compare them to a measurement. The plate was constrained between two cavities and the transmission loss was measured. There was a spherical speaker in the transmitter room, which provided the diffuse field, as well as some microphones. During the measurement, the reverberant time (T_{60}) was measured in the receiver room. The SEA plate was modeled in three different ways, a) sandwich plate, b) composite plate, c) general multilayered plate. The results showed that the composite and multilayered plates had good arrangement in the frequency range of 200 Hz – 2 kHz. Over 2 kHz, the sandwich plate had the best agreement with the measurements. The conclusion was that the difference was due to the damping value. Since this is unknown for such a wide frequency range, the author assumed a constant value.

In 2017, Siemens AG has issued a white paper on the challenges of vibroacoustic analysis of electric vehicles [1]. Electric motors have higher excitation frequencies than internal combustion engines and the accessories have higher impact to the interior noise, especially at idle and low speed. Road noise and wind noise is more prominent and thus they have greater impact on interior SPL. The problem with these excitation sources is that they are random and occur all around the car (Fig. 8). This implies the need for a full vehicle model with all noise control treatment. The size of such model is excessive for a classical FE model. Thus, SEA simulations offer a big advantage over FEM models in a sense that they are better suited for high frequency excitations and large models. The other issue with electric vehicles is that

due to the large battery weight, weight reductions become more important. In order to design a lighter vehicle, lot of new materials were developed, which modelling is another new challenge in vibro-acoustics.

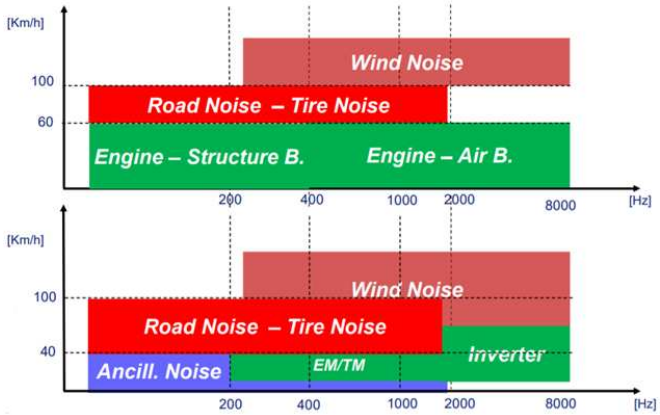

Figure 8. Contribution to interior noise for IC Engine driven vehicles (top), and Battery Electric Vehicles (bottom) [1]

An additional advantage of SEA for electric vehicles is that the modelling of exterior, infinite cavities is easier in SEA, so is the transfer path analysis as well (Fig. 9) [1].

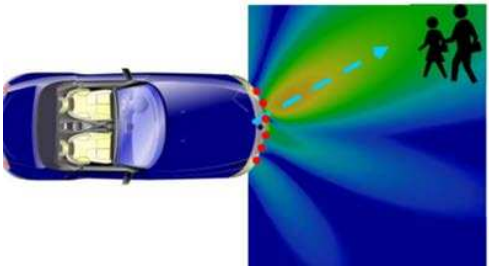

Figure 9. Exterior cavities have higher importance for electric vehicle [1]

3.2. Literatures of Hybrid FE-SEA method

Siano, et al. [29] have made an investigation of an engine cover. The authors used the hybrid FE-SEA method in different aspects. The geometry was modelled in FEM, while the cavity in SEA. The engine cover modelled as an FE model with very fine mesh, according to the authors it was able to perform the modal analysis with

100 % accuracy up to 5 kHz. They also calculated transmission loss values of the cover, but the results were not compared to measurement results.

Charpentier et al. in 2007 [30] used hybrid FE-SEA to predict the structure-borne noise transmission in a trimmed automotive vehicle in the mid frequency range. The goal was to improve the SEA definition of the panels as well as the couplings used by the local FE models. They identified that simple structural junctions (welds, bolts) can be accurately estimated using the standard algorithms. The CLFs were described via the FE model. During the experiments, they applied huge number of accelerometers, typically 10 per/subsystem. Overall, 135 accelerometers were used for 15 load cases. Simulation and experimental results were found to be within 3 dB in most of the frequency bands.

Charpentier and Fukui [16] made a really detailed and advanced fully trimmed vehicle simulation by Hybrid FE-SEA in 2008. They investigated the mid-frequency domain between 200 Hz - 1 kHz. They divided the experiment to different levels: first, a subsystem analysis, next a transmission path analysis (TPA) on the rails of the chassis. In order to reduce the computational costs, they compared the different FE models with the Hybrid FE-SEA model. The authors used different excitation points and different receiver points during the investigation, and they took into account the seals, passthroughs and leakage of the vehicle. The model was able to calculate the acceleration correctly far from the excitation point during the TPA. These time-consuming tests were successful according to the authors and the results were within 2 dB. The instrument panel simulation times reduced from 20 hours to 7 hours. The difference between the models in terms of the interior noise was about 3-5 dB.

The usage of FE-SEA method in the mid-frequency range was the focus of Chen in 2011 [31] (Fig. 10). The author made an intensive full vehicle investigation. The stiff parts of the car were modelled in FE while the flexible parts as SEA panels. The effect of the trim parts was considered as an absorption coefficient. Comparison was made at 120 km/h, the maximum absolute error was less than 3 dB(A).

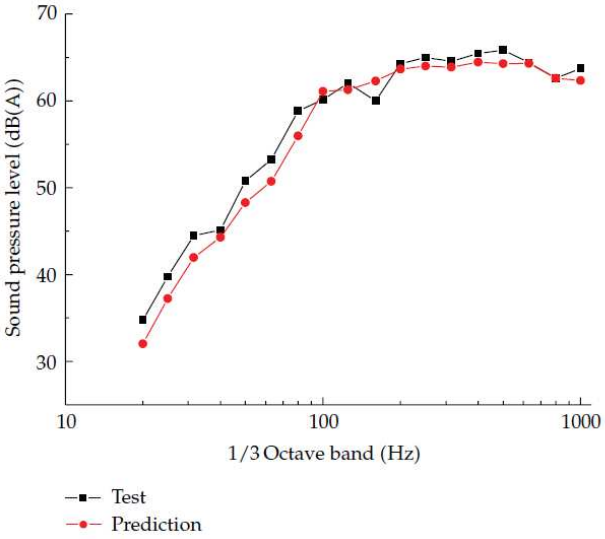

Figure 10. Simulation and measurement results [31] for a hybrid FE-SEA method applied to a fully-trimmed vehicle No information from the trim material properties was used during the prediction

Beigmoradi et al. [32] has performed an FE-SEA analysis of a car door in 2013. They made a clearance analysis of a B segment car door structure in order to improve the noise level in the driver's ear position. The trimmed door involved two parts: a trim panel and a pocket section. The clearance ranged between 0.1 and 6 mm, and they investigated only the worst-case scenario nodes. As a result, they improved the rattle by adding ribs or by increasing the number of connection points. Adding some ribs on the pocket increased the stiffness of the region and reduced the rattle.

Prasanth et al. [15] made a really detailed hybrid FE-SEA investigation for a trimmed full car in 2011 with the aim to reduce structure borne noise. The authors focused on the mid-frequency range, between 200-1000 Hz and used Noise Transfer Path Analysis (NTPA) to identify the main contributors of the interior noise. The receiver cavities were at the driver's headspace and the right-rear seat headspace. Thanks to NTPA and the detailed car model, they could redesign the parts and observe the changes. For example, a modified windshield seal reduced the vibration on the windshield which was one of the main contributors to noise. Furthermore, the headliner modification reduced the SPL too, mainly in the rear seat region. The floor and the firewall were not critical parts in this analysis. The prediction was compared

to measurement and according to the article, the biggest challenge was the repeatability of the cabin noise measurement. The SPL accuracy was ±1 dB. The model was able to predict the input power within 5 dB in most of the frequency bands.

Prasanth et al. [33] used hybrid FE-SEA method in 2013 to solve the mid-frequency problem for a fully trimmed vehicle. The stiff parts were set up as an FE model, the panel-like structures as SEA model. They used multiple sources at different locations. The sound package was modelled using a classical SEA Transfer Matrix Method and local FE models were used for each subsystem to calculate the SEA parameters. For the SEA validation, accelerometers at 40 subsystems were used, while the number of total measurement locations was 300. For the acoustic response, 40 microphones in 10 sub-cavities were applied to measure the SPL. The average difference was 3-5 dB between the measurement and the prediction. The simulation time was optimized and analysed in order to get the most accurate and reliable results as fast as possible. The fully trimmed model simulation took around 80 minutes on a regular PC.

A critical point, i.e. the definition of the correct Transmission Loss value between two cavities was addressed by Wu et al. in 2014 [34]. They developed a new approach to improve the Transmission Loss (TL) definition called Edge-based Smoothing FE-SEA (ES-FE-SEA). The goal was to make the stiff part of the deterministic model softer as well as to eliminate the numerical error in standard FEM. They compared the ES-FE-SEA results to a very smooth meshed FE model and a rough FE model. The second case was a dash panel and the results showed good agreement with the reference results. Also, computational efficiency was better than the reference one. The ES-FE-SEA method provided more accurate results than the traditional FE-SEA using the same mesh.

Tanner et al. [35] investigated in 2016 a vehicle floor that was excited between 0 - 3 kHz frequency. A hybrid FE-SEA method was used to solve the mid-frequency gap. The stiff beams were modelled by FE, while the panels as SEA models. A new alternative model for the SEA subsystems called Discrete Flow Mapping (DFM) was also developed. The DFM result was compared to Monte Carlo FEM results, and it showed good agreement with the FEM results.

Kurosawa [36] used hybrid SEA in 2016 to predict the SPL in a vehicle interior. His model consisted of 106 structural subsystems, of which 10 served as input subsystems. The number of acoustic cavity subsystems was 30. This model included the trims, damping materials, soundproof materials, as well as seals and leakages. Kurosawa determined the flow resistivity by Delany-Bazley's formula. The author pointed out that the flow resistivity will change if density changes. The sound absorption and sound insulation also changes. In conventional SEA model, the trim's

thickness distribution is considered, and he improved it further by completing it with the density changes of the material. Measurements were carried out in a semi-anechoic room. The vehicle was measured on a chassis dynamo (CDM) as well as a test course (TC) in steady-state conditions. The difference between the two conditions was the air-borne excitation. The results of the comparison were that the SPL difference was +-2 dB in the 800 Hz – 5 kHz frequency range. This paper is one of the most comprehensive ones, including a very detailed vehicle model, as well as detailed description.

4. Conclusions

This paper emphasized the importance of SEA methods as well as of Hybrid FE-SEA methods for the mid-frequency range vibroacoustic analyses. The literature review focused on the vehicle application and the cornerstones of the two methods. For example, the SEA method requires proper Coupling Loss Factors as well as Damping Loss Factors, etc. Some papers represent good and quite accurate simulation results in the mid-frequency range. Other sources present detailed vehicle models, although even in these papers the authors do not detail important model properties, such as DLFs or trim properties. Other important observation is that none of the literature described the method of how simulation from statistical methods and measurements shall be compared and the same is true for the comparison of two different simulation methods, such as the deterministic FEM and the statistically based SEA. This is expected to be a key element for objectively evaluating the accuracy of an SEA-based method, because some software use a closed formula to identify the power input or velocity response. All in all, there appears to be no generally accepted set simulation method that can achieve good correlation to measurements in the frequency range of 400 Hz – 1 kHz.

Acknowledgements

Present work was supported by the MTA-SZE Lendület Vehicle Acoustics program as well as the EFOP 3.6.1-16-2016-00017 project.

References

[1] Siemens, Vibro-Acoustic Engineering Challenges in (Hybrid and) Electric Vehicles, Siemens AG, 2017.

[2] W. Desmet, B. Pluymers, O. Atak, "MID-FREQUENCY" CAE Methodologies for Mid-Frequency Analysis in Vibration and Acoustics, 2012, pp. 233-262.

[3] P.J. Shorter, R.S. Langley, Vibro-acoustic analysis of complex systems, Journal of Sound and Vibration 288 (3) (2005) pp. 669-699. doi:10.1016/j.jsv.2005.07.010

[4] R. H. Lyon, R. G. DeJong, Theory and Application of Statistical Energy Analysis, 2nd Edition, Butterworth-Heinemann, Newton, MA, 1994.

[5] A. Le Bot, Foundation Statistical Energy Analysis in Vibroacoustics, 1st Edition, Oxford University Press, 2015.

[6] M. Fischer, Statistical Energy Analysis, Seminar: Vibrations and Sturcture-Borne Sound in Civil Engineering – Theory and Applications, 01. April, 2006

[7] N.J. Kessissoglou, J. Keir, A Hybrid Approach to Predict the Vibration Transmission in Ship Structures Using a Waveguide Method and Statistical Energy Analysis, Acoustics 2004, 3-5 November 2004, Gold Coast, Australia, pp. 587-592.

[8] B. Campolina, Vibroacoustic modelling of aircraft double-walls with structural links using Statistical Energy Analysis (SEA), Acoustics [physics.class-ph]. Université de Sherbrooke; Université Pierre et Marie Curie - Paris VI, 2012. English. <tel-00736619>

[9] H. S. Malushte, Evaluation of Statistical Energy Analysis for Prediction of Breakout Noise from Air Duct, Architectural Engineering, University of Nebraska, Lincoln, Spring 4-19-2013

[10] I. Dokhani, N.V.H. Analysis of a Vehicle using Statistical Energy Analysis, Dissertation, Blekinge Institute of Technology, Karlskrona, Sweden (2014).

[11] Lyon, R. H., Maidanik, G., Power Flow Between Linearly Coupled Oscillators, Journal of the Acoustical Society of America 34 (623) (1962) pp. 623–639.
doi: https://doi.org/10.1121/1.1918177

[12] A. Le Bot, N. Totaro, T. Lafont, Statistical Energy Analysis, Assumptions and Validity, Medyna 2017: 2nd Euro-Mediterranean Conference on Structural Dynamics and Vibroacoutics, Sevilla, Spain, 25-27 Apr. 2017.

[13] D. Johansson, P. Comnell, Statistical Energy Analysis software; Development and implementation of an open source code in Matlab/Octave, Master's Thesis, Chalmers University of Technology, Göteborg, Sweden (2010).

[14] W. Desmet, Mid-frequency vibro-acoustic modelling: Challenges and potential solutions, Proceeding of ISMA2002 – Volume II, Katholieke Universiteit Leuven Department of Mechanical Engineering, Heverlee, Belgium, 2002, pp. 835-862.

[15] S. Prasanth, A. Charpentier, K. Fukui, Using the Hybrid FE-SEA Model of a Trimmed Full Vehicle to Reduce Structure Borne Noise from 200Hz to 1kHz, SAE Technical Paper 2011-26-0020, 2011.
doi: https://doi.org/10.4271/2011-26-0020

[16] A. Charpentier, P. Shreedhar et al., Modeling process and validation of Hybrid FE-SEA method to structure-borne noise paths in a trimmed automotive vehicle, 2008 SAE Brasil Noise and Vibration Conference, Florianópolis, SC, Brazil, March 30th to April 01st, 2008.
doi: https://doi.org/10.4271/2008-36-0574

[17] K. Delaere, M. Iadevaia et al., Statistical Energy Analysis of Acoustic Noise and Vibration for Electric Motors: Transmission from Air gap Field to Motor Frame, Conference Record of the 1999 IEEE Industry Applications Conference, Thirty-Forth IAS Annual Meeting, Phoenix, AZ, USA, 1999, pp. 1897-1902.
doi: https://doi.org/10.1109/IAS.1999.805997

[18] E. Sarradj, Energy-based vibroacoustics: SEA and beyond, Proceedings of the Joint Congress CFA/DAGA'04, Strasbourg, France, 2004, pp. 1157-1162.

[19] I. Hauer, K. Jalics et al., Prediction of Vehicle Interior Noise in High Frequency Range using Statistical Energy Analysis Hybrid Method, Proceedings of the Joint Congress CFA/DAGA'04, Strasbourg, France, 2004, pp. 11-12.

[20] R. Panuszka, J. Wiciak, M. Iwaniec, Experimental Assessment of Coupling Loss Factors of Thin Rectangular Plates, Archives of Acoustics 30 (4) (2005) pp. 533-551.

[21] C. Xin, D. Wang, Z. Ma, Simulation on a Car Interior Aerodynamic Noise Control Based on Statistical Energy Analysis, Chinese Journal of Mechanical Engineering 25 (5) (2012) pp. 1016-1021.

[22] D. Blanchet, A. Golota, Validation of a wind noise source characterization method for vehicle interior noise prediction, Proceedings of ISMA 2014 International Conference on Noise and Vibration Engineering, USD 2014 International Conference on Uncertainty in Structural Dynamics, Leuven, 2014, pp. 241-256.

[23] A. Putra, A. Munawir, W.M. Farid, Corrected Statistical Energy Analysis Model for Car Interior Noise. Advances in Mechanical Engineering (2015) doi: https://doi.org/10.1155/2014/304283

[24] A. Bötke, E. Erensoy, C. Sevginer, Modeling and Validation Processes of an Electric Vehicle with Statistical Energy Analysis, Euronoise 2015, Maastricht, 2015, pp. 1417-1422.

[25] J. Gu, M. Sheng, Improved Energy Ratio Method to Estimate Coupling Loss Factors for Series Coupled Structure, Journal of Mechanical Engineering 45 (1) (2015) pp. 37-40.
doi: https://doi.org/10.3329/jme.v45i1.24382

[26] Y. S. Jang, J. Y. Kuk et al., SEA Modeling and Validation of a Truck Cab for Sound Package Optimization, Inter.Noise Conference 2015, San Francisco, California, USA, 2015, p. 12.

[27] Y. S. Jang, J. Y. Kuk et al., Optimization of the Sound Package of a Truck using Statistical Energy Analysis, Inter.Noise Conference 2015, San Francisco, California, USA, 2015, p. 12.

[28] J. Károly, Investigation of Acoustic Properties of Poroelactic Materials with Measurement and Simulation, GÉP 68 (4) (2017) pp. 11-14, in Hungarian

[29] D. Siano, M. Viscardi, R. Aiello, An Hybrid FE/SEA Approach for Engine Cover Noise Assessment, Recent Researches in Mechanical and Transportation Systems, pp. 199-205.

[30] A. Charpentier, P. Shreedhar, K. Fukui, Using the Hybrid FE-SEA Method to Predict Structure-Borne Noise Transmission in a Trimmed Automotive Vehicle, SAE Technical Paper 2007-01-2181, 2007. doi: https://doi.org/10.4271/2007-01-2181

[31] S.M. Chen, D.F. Wang, J.M. Zan, Interior Noise Prediction of the Automobile Based on Hybrid FE-SEA Method, Mathematical Problems in Engineering, 2011 (Article ID 327170) p. 20. doi: https://doi.org/10.1155/2011/327170

[32] S. Beigmoradi, K. Jahani, H. Hajabdollahi, Squeak and rattle noise prediction for trimmed door of a car using hybrid statistical energy – Finite element method analysis, The Journal of the Acoustical Society of America 133 (5) (2013) pp. 3462-3462.

[33] S. Prasanth, P. Shreedhar et al., Modeling process and validation of Hybrid FE-SEA method to structure-borne noise paths in a trimmed automotive vehicle, International Journal of Research in Aeronautical and Mechanical Engineering 1 (3) (2013) pp. 17-28.

[34] F. Wu, G.R. Liu et al., Mid-frequency prediction of transmission loss using a novel hybrid deterministic and statistical method, JVE International LTD. Vibroengineering Procedia 4 (2014) pp. 34-39.

[35] G. Tanner, D.J. Chappell, Comparison of Methods for Modelling Mid-to-High Frequency Vibro-Acoustic Energy Distributions in a Vehicle Floor Structure, SAE International 2016, 06/15/2016 doi: https://doi.org/10.4271/2016-01-1853

[36] Y. Kurosawa, Predicting Automotive Interior Noise Including Wind Noise by Statistical Energy Analysis, International Journal of Mechanical and Mechatronics Engineering 10 (3) (2016) pp. 635-641.